MODELING, CHARACTERIZATION, AND MAGNETIC BEHAVIOR OF TRANSITION

METAL NANOSYSTEMS SYNTHESIZED IN SILICON USING

LOW ENERGY ION IMPLANTATION

Satyabrata Singh, B.Sc., M.Sc.

Dissertation Prepared for the Degree of

DOCTOR OF PHILOSOPHY

UNIVERSITY OF NORTH TEXAS

May 2021

APPROVED:

Bibhudutta Rout, Major Professor
Gary A. Glass, Committee Member
Duncan L. Weathers, Committee Member
Oliviero Andreussi, Committee Member
Jingbiao Cui, Chair of the Department of
    Physics
Su Gao, Dean of the College of Science
Victor Prybutok, Dean of the Toulouse
    Graduate School

Singh, Satyabrata. *Modeling, Characterization, and Magnetic Behavior of Transition Metal Nanosystems Synthesized in Silicon Using Low Energy Ion Implantation*. Doctor of Philosophy (Physics), May 2021, 106 pp., 3 tables, 56 figures, 95 numbered references.

Magnetic nano-clusters in silicon involving iron and cobalt were synthesized using low energy (50 keV) ion implantation technique and post-implantation thermal annealing. Before the irradiation, multiple ion-solid interaction simulations were carried out to estimate optimal ion energy and fluence for each experiment. For high-fluence low-energy irradiation of heavy ions in a relatively lighter substrate, modeling the ion irradiation process using dynamic code SDTrimSP showed better agreement with the experimental results compared to the widely used static simulation code TRIM. A saturation in concentration ($\sim$ 48%) profile of the 50 keV Fe or Co implants in Si was seen at a fluence of $\sim 2 \times 10^{17}$ ions/cm^2. Further study showed that for structures with a curved surface, particularly for nanowires, better simulation results could be extracted using a code "Iradina" as the curve geometry of the target surface can be directly defined in the input file. The compositional, structural, and magnetic properties were studied using Rutherford backscattering spectrometry, X-ray photoelectron spectroscopy, X-ray diffraction, atom probe tomography, and vibrating sample magnetometry. Irradiation of high-current ($\sim$ 2 µA/cm^2) 50 keV Fe ions into Si at a fluence of 2×10^{17} ions/cm^2 showed the formation of Fe_5Si_3 nano structures in the near-surface region of the substrate. Post-implantation thermal annealing in vacuum at 500 ^{o}C for one hour showed a significant enhancement in structural and magnetic properties. Similar high-current irradiation of 50 keV Co with a fluence of 3.2×10^{16} ions/cm^2 into Si substrate showed the formation of superparamagnetic structure even at room temperature in the as-implanted samples. The simulation results for irradiation of Co and Fe on the curved surface were validated by ion irradiation on pre-fabricated Si nano tip followed by atom probe tomography analysis.

ACKNOWLEDGEMENTS

TABLE OF CONTENTS

LIST OF TABLES

LIST OF FIGURES

CHAPTER 1

INTRODUCTION

In the last couple of decades, tremendous progress has been made in nanoscale science and technology resulting in the rapid development of devices in semiconductors and biomedical industries. At a nanometer scale, the fundamental properties of materials become dependent on the size of the particle. Several factors are responsible at the nanoscale that causes the fundamental property to be different from the bulk material. One key factor is the surface-to-volume ratio of atoms. This ratio increases with a decrease in the dimension of a particle. The electronic, magnetic, optical, and chemical properties of material get enhanced as one makes a transition to a nanoscale. In this research, we have focused our study on the synthesis and magnetic behavior of transition metal nano-structures formed near the top surface regions (~ 50 nm) of silicon substrates and nanowires.

1.1   Transition Metal Silicide

Most of the transition metal silicides are metals and they are divided into two categories, binary and ternary transition metal silicides. As their name suggests, binary silicides consist of two materials, one of them is silicon (Si) and the other can be any metal. Ternary silicides consist of three materials where one of them is Si and the other two can be any metal. Because of the favorable electrical properties of these metal silicides, it is used as gates and interconnects in very-large-scale integration circuits in microelectromechanical systems (MEMS). One can choose different materials from (Fe, Co, Ni, Cr, Ti, Pt, etc.). Fe and Co embedded materials have shown great interest among researchers over the past decades. Due to the recent advancements in nanoscience, a great number of researchers have been working towards a scalable synthesis process of metallic nanowires. These nanowires can be used as nano connectors and as the active

components of nanoelectromechanical system (NEMS) devices. Metal silicides are an indispensable part of microelectronics. Synthesizing them in nanoscale will be useful in the NEMS devices. Apart from the electronic property, Fe and Co are ferromagnetic. Hence compounds involving Fe-Si or Co-Si exhibit magnetic property which has various applications in spintronics, and biomedical fields.

1.2   Preparation Techniques of Semiconducting Silicide Nano Systems

For the preparation of semiconducting silicide nano systems, a large number of deposition techniques have been applied, including sputtering or evaporation of metal on silicon and subsequent in-situ or ex-situ thermal annealing. Some of the synthesis methods involve co-deposition of the metal components on cold or hot silicon or other substrates from two separate sources, co-sputtering or laser ablation from a composite target of the corresponding composition, and implantation of metal ions into silicon forming buried layers. After each deposition process a thermal treatment between 400 °C to 1000 °C (depending on the silicide studied) is necessary to transform the layer into the semiconducting phase. Considerable efforts have been directed towards epitaxial growth of semiconducting silicides on Si by employing various techniques such as solid-phase epitaxy (SPE), reactive deposition epitaxy (RDE), molecular beam epitaxy (MBE), and chemical vapor deposition (CVD) epitaxy.

Most of the published results on the synthesis of these silicides are chemical-based such as RDE, CVD, SPE, etc. Most of these materials are used in device manufacturing industries which needs a large-scale synthesis process of these materials. Ion beam synthesis is widely used by the microelectronics industries over the years and still an important processing step for device fabrication. Hence there is a need for research on the synthesis and optimization of the process of making these metal silicides using an ion beam implantation technique.

One of the mechanisms responsible for the rearrangement of atoms is localized thermal annealing. The metal alloys such as Heuseler of a few atomic mixtures are usually synthesized via the mechanical ball milling with post-thermal annealing, arc melting, chemical mixing, and magnetron sputtered co-deposition at elevated substrate temperatures and using expensive molecular beam epitaxy techniques. Each of these techniques suffers from the presence of contaminations in the targets' surfaces and gas environments during the vaporization as well as time-consuming physical mixing and grinding processes. The synthesis process can get much complicated while trying to understand the diffusion of each element at annealing temperatures while forming alloys with more than one metal component and eutectic temperatures. The fabrication of scalable nanoscale structures can be extremely challenging in terms of time, reproducibility, and cost too. Also, another serious concern is the stability of the newly formed phases when the samples are exposed to the atmospheric environment. In this research we have explored the utilization of low energy (< 50 keV) transition metals (Fe, Co), to create nanostructured systems near the surface of Si substrates or Si nano-posts.

1.3   Some of the Reported Study on Transition Metal Silicides

Transition metal silicides show mostly metallic behaviors at their stable phase configuration. Favorable electrical properties of these metallic silicides have made them attractive components in very-large-scale integrated circuits (VLSI) as gates and interconnect. Further, they can be used as reliable high-barrier Schottky or ohmic contacts of low resistance [1]. The silicon microelectronics industry is interested in Si-rich phases at end phase diagrams of the transition metal-silicon phases due to their high thermal and chemical stability and corrosion resistance against the attack of oxidizing ambient. Apart from the metallic silicides, a few silicides also show semiconducting properties [2]. The study involving various phases of iron and silicon has been

reported since 1943 [3]. The Fe-Si binary system provides several iron-silicides that have varied and exceptional material properties with applications in the electronics industry. The well-known Fe-Si binary silicides are Fe_3Si, Fe_5Si_3, $FeSi$, α-$FeSi_2$, and β-$FeSi_2$. A Si-rich phase of the Fe-Si system, such as β-$FeSi_2$, is an excellent candidate for photovoltaic applications. The β-$FeSi_2$ phase shows a highly stable reversible capacity when used as an anode material for rechargeable lithium batteries [4]. Such Si-rich phases are also promising candidates for optoelectronic [5–7] and thermoelectric applications[8]. The iron-rich phase of the Fe-Si system, such as Fe_2Si, behaves as half-metals with 100% spin–polarization at the Fermi level. Such behavior of Fe_2Si is important for spintronic applications [9,10]. The iron-rich silicide Fe_3Si is known to be ferromagnetic at room temperature [11–13]. Over the past decade, several studies have been reported involving the synthesis and properties of these silicides as nanocrystals. Wang et al. have studied the stress distribution around Fe_5Si_3 and its effect on the mechanical properties of Si_3N_4 [14]. Lyashchenkoa et al. have studied the optical and Magneto-optical properties of Fe_5Si_3 and Fe_3Si magnetic silicides using spectral magneto-ellipsometry [15]. Kolel-Veetil et al. have reported the magnetic properties of Fe_5Si_3 nanoparticles which shows that it has a Curie temperature of 375K [16]. Tripathi et al. have reported the ion-beam irradiation synthesis and magnetic properties of Fe_5Si_3 which shows that these nanoparticles are superparamagnetic [17]. Yoon et al. have reported room-temperature ferromagnetic properties in Si substrate implanted with 200 keV Fe and thermal annealing at 800 and 900 ºC [18]. Errandonea et al. have reported the study of structural stability of Fe_5Si_3 by high-pressure x-ray diffraction (XRD) analysis and ab initio calculations [19]. Recent Density functional theory (DFT) calculation by Skomski et al. showed that both bulk and nanostructured Fe_5Si_3 have a Curie temperature higher than room temperature [20]. Among the reported properties of iron-rich silicide, Fe_5Si_3 alloy also shows ferromagnetism at room temperature [16,21].

However superparamagnetic phenomenon has been observed in these ferromagnetic crystals with the reduction of the grain size of the structure below 100 nm [17]. In a superparamagnetic material, the nanoparticles can flip the direction of magnetization under the influence of temperature. Recently, these magnetic nanomaterials have received wide attention due to their applications in the biomedical industry for magnetic resonance imaging [22], gene therapy [23], and cancer therapy [24]. The iron-rich silicide nanoparticles can be inserted into polymer particles and can be made biocompatible. So, there is a great need for the synthesis of these magnetic nanoparticles at a larger scale.

1.4   Reported Studies Involving Ion Beam Synthesis

Various methods have been adopted over the past several years to synthesize these silicides including the ion beam synthesis method. Senthilarasu et al. have studied the β-FeSi$_2$ for photovoltaic application synthesized using electron beam evaporation and post thermal annealing at 650 °C [25]. Tatar et al. have reported the study of β-FeSi$_2$ synthesized via magnetron sputtering [26]. Shimura et al. have studied the photoluminescence of β-FeSi$_2$ synthesized by the ion beam sputter deposition method [27]. Santamaría-Pérez et al. have reported the synthesis of Fe$_5$Si$_3$ by a solid-state reaction in high temperature and pressure conditions (up to 30 GPa) [28]. These silicides have also been synthesized via ion beam synthesis by various researchers utilizing ion implantation and ion beam mixing of the thin-film [29–33]. Tripathi et al. have reported the formation of granular metallic Fe$_5$Si$_3$ silicide phase due to strong interfacial intermixing in Fe/Si bilayer samples with irradiation of swift (100 MeV) Fe ions. Chong et al. have reported the study of FeSi$_2$ synthesized via low energy ion implantation and post thermal annealing at 850 °C for 10 hours [34]. Lakshantha et al. have studied the depth profile of Fe in Si and formation of β-FeSi$_2$ phase in the case of 50 keV Fe implantation in Si and post-thermal annealing at 800 °C for 1 hour [35].

Gumarov et al. have studied the ion irradiation fluence dependence on the local magnetic properties of ion beam synthesized silicide films [36]. Omae et al. have reported the formation of a continuous β-FeSi$_2$ top-layer in elevated temperature (350 ºC) irradiation of 120 keV Fe in Si with a fluence of 4×10^{17} atoms/cm^2 and post-thermal annealing in a vacuum furnace at temperatures ranging from 500 ºC to 800 ºC [37]. Naito et al. have studied the ion beam synthesized Fe-Si layers using transmission electron microscopy (TEM) and have reported the effect of post-thermal annealing at various temperatures (200 ºC to 700 ºC) [38]. Yang et al. have reported the formation of various Fe-Si phases in the case of low energy Fe$^+$ ion implantation and post-thermal annealing at different temperatures ranging from 400 - 800 ºC [39]. These studies have shown that if a sufficient amount of Fe is present in ion implantation depths, it is possible to synthesize predominantly iron-rich phases by annealing at a lower temperature up to 500 ºC.

1.5   Origin of Magnetism in Solids

The magnetism in the case of solid is originated from the electronic configuration of atoms. The electrons in an atom have two types of angular momentum; orbital angular momentum and spin angular momentum. As electrons are charged particles, the motion of electrons creates a magnetic field. Hence the magnetic moment contribution comes from both orbital and spin angular momentum. In a solid, generally many electrons are moving around the nucleus but only two electrons with different spin orientations (up or down) can occupy the same orbit. Hence, the magnetic moments originated from spins cancel each other and do not contribute to the magnetic moment of a solid. In the case of a transition metal such as Fe, Co, and Ni the 3d-subshell is not fully occupied, and they have unpaired electrons. These unpaired electrons contribute to the magnetic moment of the atom. The best way to classify various types of magnetism is by studying their response to external magnetic fields. Here we have discussed in brief some of these magnetic

behaviors observed in various materials.

1.5.1 Diamagnetism

Diamagnetism exists in most of the materials but is usually very weak. For a diamagnetic material, the atoms have no net magnetic moment because of the unavailability of unpaired electrons in the atom. When an external magnetic field is applied, an induced magnetic field is created in the material in a direction opposite to the applied magnetic field producing a negative magnetization. Thus, susceptibility is negative and very small in the case of diamagnetic material. Once the external magnetic field is removed, the net magnetic moment of the material becomes zero. Figure 1.1 (a) shows the relation between M (magnetization) and H (applied magnetic field) in the case of a diamagnetic material. Silicon is one such material that is diamagnetic.
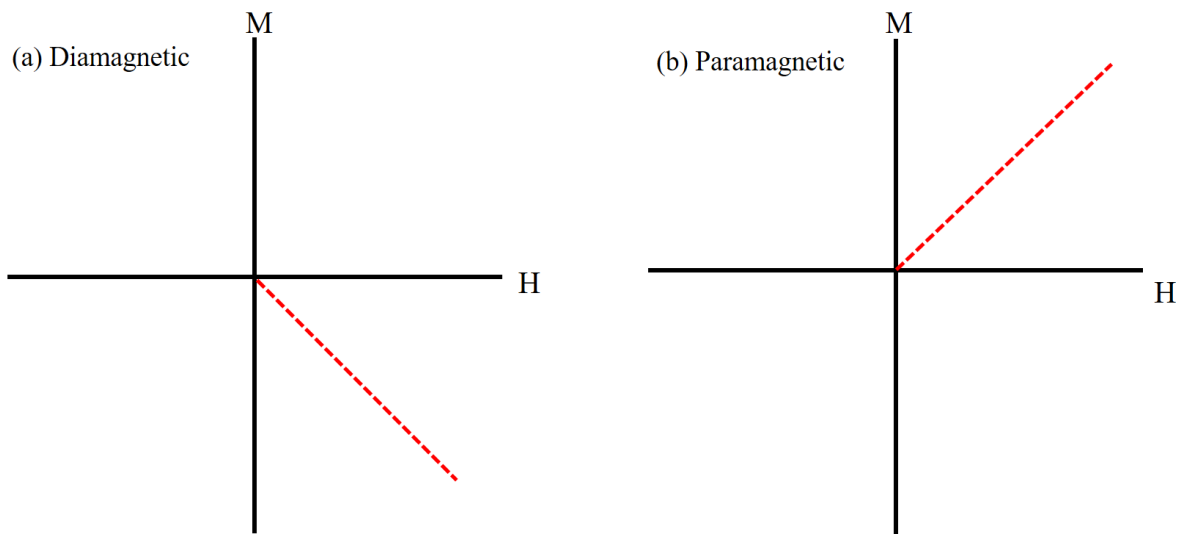
Figure 1.1: M vs H for (a) diamagnetic and (b) paramagnetic substance.

1.5.2 Paramagnetism

Paramagnetic materials are attracted to an external magnetic field. In these materials, the atoms have a net magnetic moment due to unpaired electrons in partially filled orbitals. In this case, the individual magnetic moments are randomly oriented inside the material. When an

external magnetic field is applied, they are oriented in the same direction as the applied magnetic field giving a positive magnetic moment and susceptibility, but the value of the susceptibility is very low. Once the external field is removed, the net magnetization becomes zero. The number of unpaired electrons in this type of material is usually smaller. The higher number of unpaired electrons gives rise to ferromagnetism. Figure 1.1 (b) shows the relation between M and H in the case of a paramagnetic material.

1.5.3   Ferromagnetism

In this type of material, the atomic moments exhibit very strong interactions between them. The exchange interaction in the case of these materials is significantly higher than the magnetic dipolar interactions. There are magnetic domains inside the material and inside a domain, all the magnetic moments are aligned in one direction. A schematic representation of the magnetic domain in the case of ferromagnetic material is illustrated in Figure 1.2.
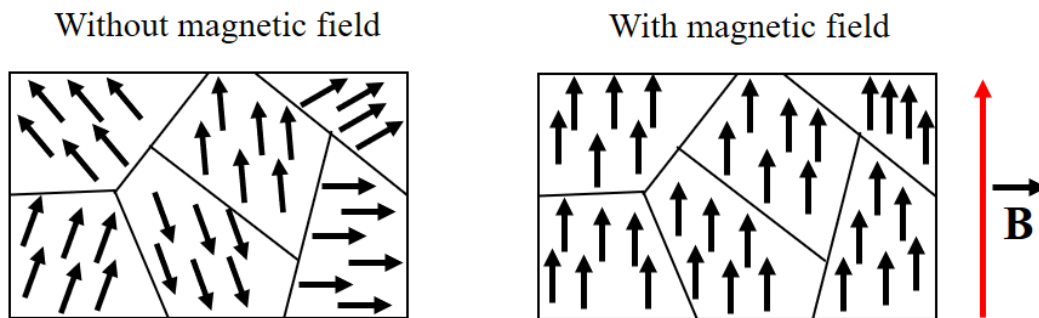
Figure 1.2: Magnetic domain inside a magnetic material.

Within a domain, the magnetic dipoles are aligned along the local easy axis. However, when an external magnetic field is applied, individual magnetic moments inside the magnetic domain align themselves in the direction of the applied magnetic field. Once the magnetic field is removed, these domains can retain the memory of the applied magnetic field and remain aligned in the same direction until forces are applied to the material which causes the domains to change the direction.
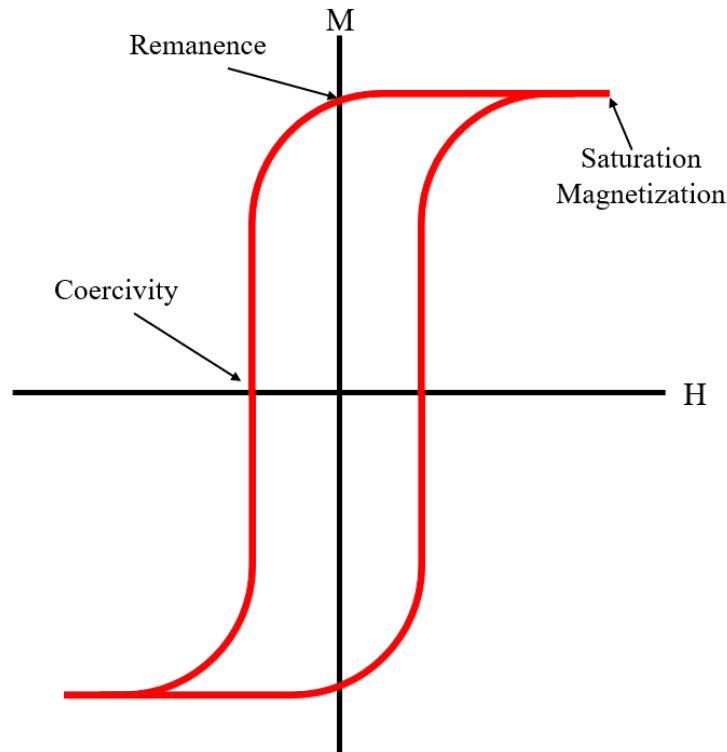
Figure 1.3: M vs H curves for ferromagnetic material showing the coercive field, remanence, and saturation magnetization.

In the case of ferromagnetic materials, for a certain value of the applied magnetic field, the induced magnetization becomes maximum. Further increase in the applied magnetic field does not increase the net induced magnetic moment. This is known as saturation magnetization. The saturation magnetization in the case of a ferromagnetic compound is different for different types of materials and strongly depends on the substrate temperature. The ferromagnetic substance can retain the memory of the applied magnetic field and the net induced magnetization is nonzero even at zero applied magnetic field. This is called remanent magnetization. This behavior is called hysteresis and a plot of the variation of magnetization with the magnetic field is called a hysteresis loop. A schematic representation of the M vs H curve for ferromagnetic materials is shown in Figure 1.3. Another term often used is called coercivity. It is the value of the applied magnetic field that is needed to make the remanent magnetization zero. The various hysteresis parameters

in the case of a ferromagnetic material strongly depend on both crystal structure and substrate temperature. There is also a temperature limit in the case of ferromagnetic material known as Curie temperature. Beyond the Curie temperature, the materials lose their magnetic property. Curie temperature is different for different types of materials.

1.5.4 Superparamagnetisim

The concept of superparamagnetism was first proposed by Frenkel and Doefman in 1930 [40]. In several reported research, it was seen that this type of magnetic behavior occurs only on a nanoscale when the particle size is below 100 nm [41]. The average size of a magnetic domain mainly depends on the exchange energy, anisotropy, and magnetic dipolar energy. With the decrease in dimension, the number of magnetic domains also decreases inside the material. Below a critical dimension, a material changes from a multi-domain system to a single domain system and becomes superparamagnetic. At this stage, the material stays fully magnetized.

In the case of superparamagnetic substance, temperature plays an important role in retaining its magnetic status. There is a critical temperature below in which the material remains in a ferromagnetic state at the nanoscale. Beyond this temperature, the material becomes superparamagnetic. This temperature is known as the blocking temperature. Superparamagnetic materials have a high saturation magnetization and zero coercivity and remanence, making it to be distinguished from the ferromagnetism state. The dissertation has been arranged in the following way after this brief introduction chapter explaining the various states of magnetism. Chapter 2 describes the various experimental techniques used in this research work. A brief introduction to the basic physical principles involving various Monte-Carlo simulation codes used for the ion-solid interaction in 1D and 3D models is described in Chapter 3. Chapter 4 discusses the results of the simulation study of surface sputtering and distribution of ions in silicon due to the low energy

high-fluence cobalt irradiation. Chapter 5 discusses the observation of room temperature superparamagnetic behavior of Fe_5Si_3 nanocrystals synthesized via 50 keV Fe ion implantation in silicon substrate. Chapter 6, reports the formation of superparamagnetic Co-Si nanostructure embedded inside Si substrate, synthesized via 50 keV Co ion implantation. In chapter 7, the simulation of interaction of the 50 keV Co and Fe irradiated on 3D curved surfaced nanostructures (pre-fabricated silicon nano-post) and characterization of the irradiated samples using atom-probe tomography is reported. Chapter 8 gives a summary of the work reported in this dissertation.

CHAPTER 2

EXPERIMENTAL METHODS

For this research, all the samples were synthesized using a low energy ion implantation system associated with a 3 MV tandem Pelletron accelerator available at Ion Beam Modification and Analysis Laboratory (IBMAL) of the University of North Texas (UNT) [42]. A National Electrostatics Corporation (NEC) Source of negative ions by cesium sputtering (SNICS-II) was used to produce and accelerate the Fe and Co ions from a solid cathode. The analytical measurements were performed at the UNT's Material Research Facility (MRF), while the VSM measurements were performed at the UNT's Advanced Materials and Manufacturing Processes Institute (AMMPI). A brief description of some of the synthesis and characterization instruments and their working principles is discussed in this chapter.

2.1   Low Energy Ion Implantation

Ion implantation is generally used to introduce impurities into various substrates in a very controlled way. The concentration of the impurity can be controlled by changing the ion fluence during the implantation. The profile of the ions in the substrate mainly depends on the mass, energy, and angle of incidence of the implanted ions. The energy of the implanted ions can be varied depending on the required range of the implanted ions. One of the main advantages of the ion-implantation process is that the doping area, concentration, and penetration depth of the implanted ions can be controlled. This allows modification of the substrate near the surface region with a high concentration of the dopant ions in case of low energy implantation (50 keV in this study). The recrystallization of the implanted ions is usually carried out by annealing the substrate via different methods. The annealing process causes a redistribution of the implanted ions in the substrate. Thus, the ion beam synthesis technique is one of the important tools for nanomaterial

synthesis used in these manufacturing industries, particularly near-surface buried nanostructures,

which can be protected from surface contaminants.
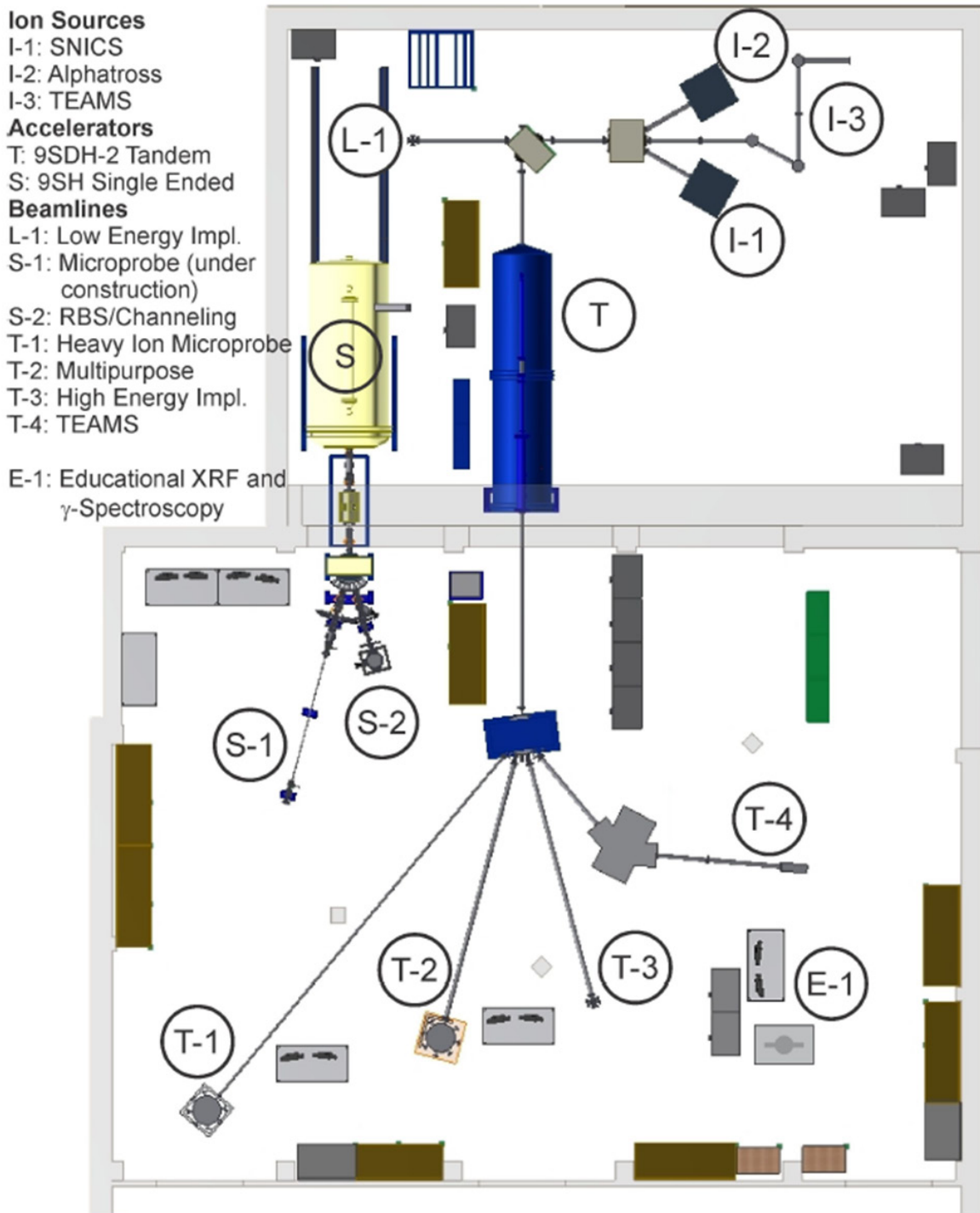
Figure 2.1: Schematics of the ion beam facility at UNT.

A schematic of the ion beam facilitates at IBMAL is given in Figure 2.1. The main laboratory houses two ion accelerators. A 3 MV tandem Pelletron accelerator (NEC 9SDH-2) mainly used for low-energy (15 - 85 keV) and high-energy (up to (q+1) ×3 MV, where q=charge state)) implantation of various elements. A 3 MV (NEC 9SH) single-ended Pelletron accelerator is used for ion beam analysis using broad as well as microbeam of mostly proton or helium ions.

The source of the 9SH-2 tandem accelerator contains a solid cathode source called the Source of Negative Ions using Cesium Sputtering (SNICS). The SNICS ion source can produce ion beams for all elements that form a stable negative ion by the sputtering mechanism using cesium vapor. The cesium oven is heated to a temperature up to ~170 ºC which allows the cesium vapor to flow from the cesium oven into the ionizing chamber. Most of the cesium is ionized by the hot surface, while some of the cesium condenses on the front of the cathode.
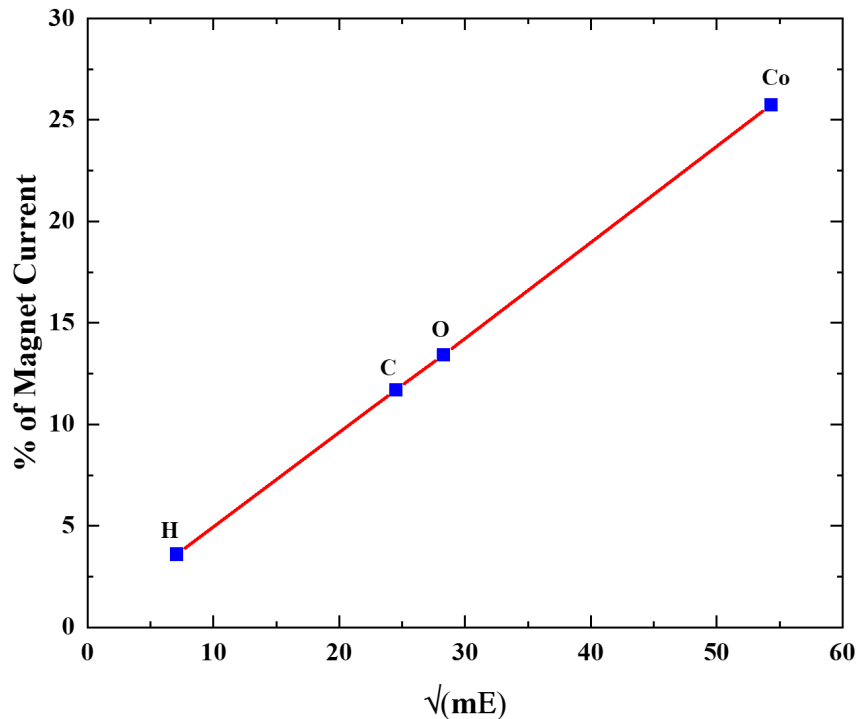
Figure 2.2: Calibration of mass selector magnet used for extraction of 50 keV cobalt ions. The mass is in the unit of amu and energy in the unit of keV.

The ionized cesium sputters atoms from the cathode through a condensed cesium layer on the cathode face. The ions are then accelerated into the beamline. The beam is focused using an einzel lens and is steered using a set of parallel plates to ensure that the beam is at the center of the beamline. Keeping the beam at the center of the beamline is essential for better transmission of the ions from the source to the target area. The beam then goes through a momentum per charge selector magnet that has a resolution of 1 amu. The magnet is usually calibrated by identifying several known elements in the beam. One example of calibration is showed in Figure 2.2 that was used to identify and filter pure cobalt beam. Once the beam is filtered through the magnet, a second magnet is used to bend the beam to the low energy beamline. The schematic for the low energy beamline is given in Figure 2.3.
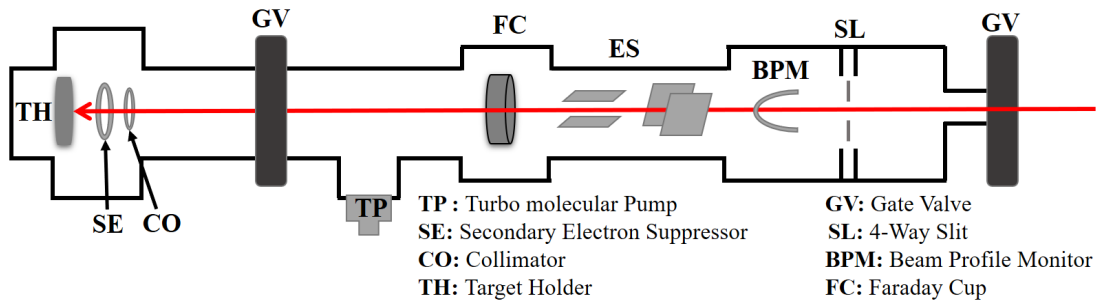
Figure 2.3: Schematics of the low energy beamline at IBMAL.

Apart from the vacuum pumps, the low energy line mainly consists of a set of slits, a faraday cup, a collimator, and a secondary electron suppressor. The suppressor voltage is usually set to 300 V for such experiments. The beam is finally raster scanned (400 V × 400 V) over a circular target area of 3.14 cm^2 to ensure a uniform implantation profile. The target is usually given a positive bias of 100 V to avoid secondary electron emission from the sample surface. Figure 2.4 illustrates the uniformity of the implantation elemental depth profile taken from various spots on the target. The elemental concentration depth profile was extracted using Rutherford backscattering spectrometry techniques on a sample of 50 keV cobalt implanted into Si wafer.
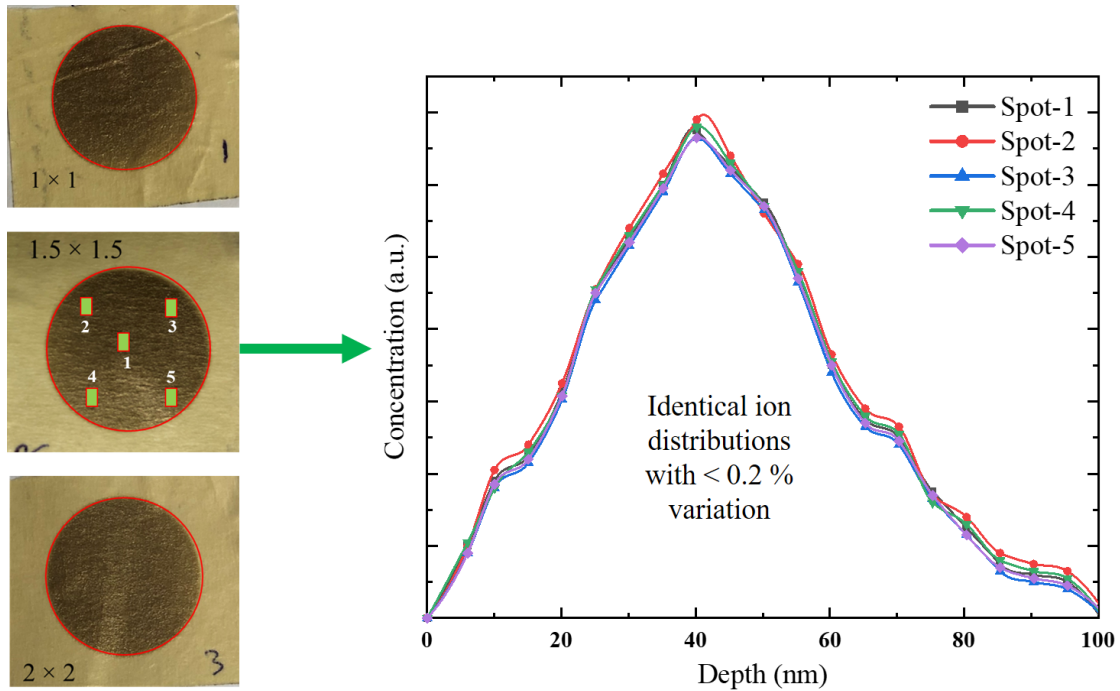
Figure 2.4: Ion distribution from various sections of the target surface showing the uniformity of the implant concentration profile. The elemental (cobalt) concentration profile was extracted using Rutherford backscattering spectrometry (RBS) technique.

2.2   Rutherford Backscattering Spectrometry (RBS)

RBS is a widely used technique in the ion beam community to measure the concentration or compositional depth profile of implanted atoms in a target material. RBS is a relatively non-destructive technique and easy to perform. The sensitivity of RBS measurements is on the order of parts per thousand [43], but is strongly dependent on the element to be analyzed and the substrate.

In this method, a collimated ion beam of known energy (He^+ beam of 1.5 MeV energy in this case) is incident on a solid target. The energy of the elastically backscattered ions, which provide elemental information about the sample, is typically measured using a solid-state, surface barrier detector. The setup of the RBS chamber at the general-purpose beamline associated with the 9SH single-ended accelerator of the IBMAL is illustrated in Figure 2.5.
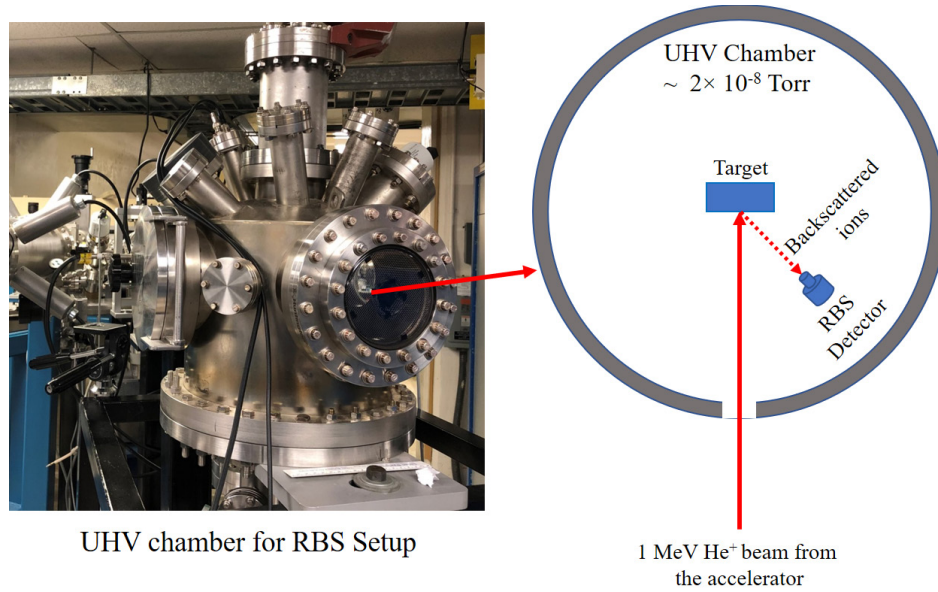
Figure 2.5: Photograph and schematics of the RBS chamber at the general purpose beamline associated with the 9SH single ended accelerator of IBMAL.
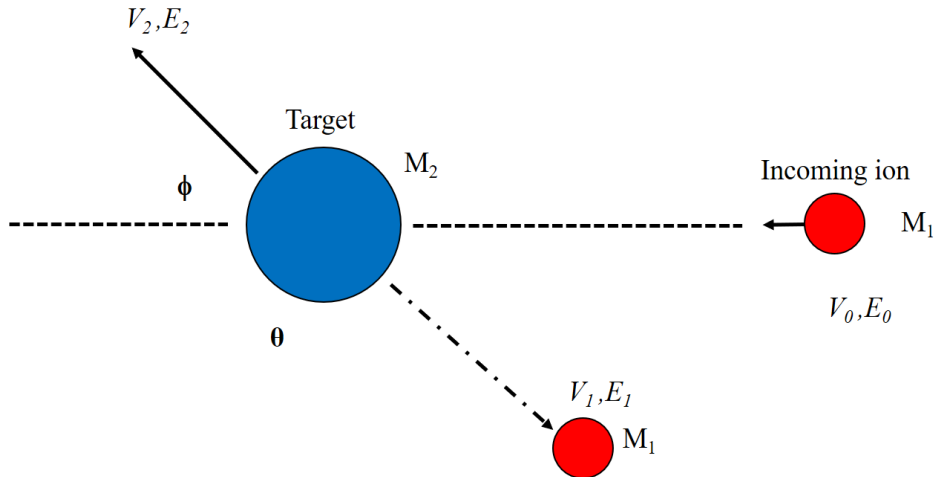
Figure 2.6: Elastic collision between incoming ions of mass M_1, velocity V_0, and energy E_0 and a target atom of mass M_2 which is initially at rest. After the collision, the incoming ion and the target atom have velocities and energies V_1, E_1 and V_2, E_2, respectively. The angles θ and φ are positive as shown. All quantities refer to a laboratory frame of reference.

The elastic scattering processes can be described by a kinematic factor K, where the K is given by the following equation,

$$K = \frac{M_1^2}{(M_1+M_2)^2}\left\{\cos\theta \pm \left[\left(\frac{M_2}{M_1}\right)^2 - \sin^2\theta\right]^{1/2}\right\} \qquad \text{(Eq. 2.1)}$$

where M_1 is the mass of the incident ion and M_2 is the mass of the target atom. Using the energy

and momentum conservation, one can obtain a set of equations and solve for the kinematic scattering factor, K, defined as the ratio of the scattered energy of the projectile to that of its initial energy, $(E_1=E_0)$. Equation 2.1 gives an expression for K and the derivation of K can be found in Rutherford backscattering spectrometry [43].

2.3   X-ray Diffraction (XRD)

X-ray diffraction (XRD) is one of the most common techniques used for semiconductor research to identify the crystallinity of a synthesized structure. In this method, X-rays of a known wavelength are passed through a powder sample to fully investigate its crystal structure. These X-rays are diffracted by the lattice of a crystal to give a unique pattern which is used to identify the type of crystal planes and crystal structures in the sample.

The diffracted beams from atoms in successive planes cancel unless they are in phase, and the condition for this is given by the Bragg law as follows.

$$2\mathrm{dsin}\theta \ = \ n\lambda \qquad\qquad\qquad (\text{Eq. } 2.2)$$

where λ is the wavelength of the x-rays, d is the distance between the different planes of atoms in the crystal lattice and θ is the angle of diffraction.

In this research X-ray diffraction studies on the synthesized samples were carried out using a high-resolution Rigaku Ultima III diffractometer with a Cu K_α monochromatic beam ($\lambda = 0.154$ nm) produced at 40 kV energy and 40 mA current. The Rigaku Ultima III enables a variety of applications including in-plane and normal geometry phase identification, quantitative analysis, lattice parameter refinement, crystallite size, structure refinement, density, roughness, and multilayer thicknesses (from reflectivity geometries), and depth-controlled phase identification. For our case, glancing angle diffraction was used where the X-ray beam was incident at a fixed angle to the sample surface and, the detector was positioned at various angles from 20°-120°. This

18

ensured that the X-rays were diffracted from the top ~100 nm of the sample where the ions were implanted, and various crystal structures were formed. A schematic for the XRD setup is shown in Figure 2.7.
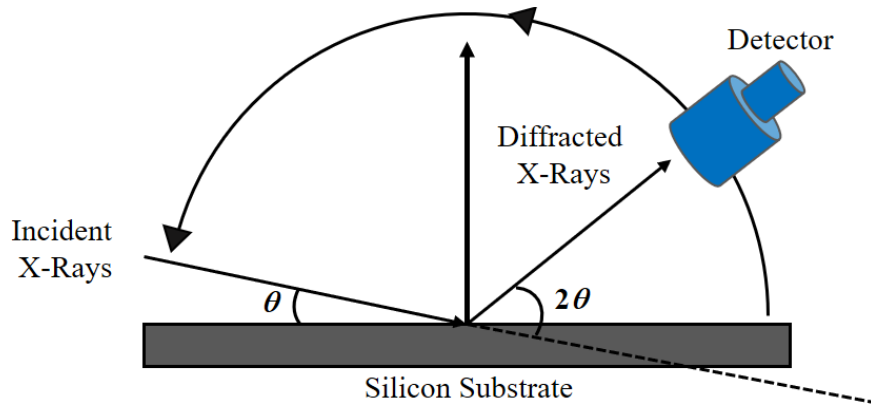
Figure 2.7: Schematic representation of XRD setup.

2.4   Vibrating Sample Magnetometer

Vibrating sample magnetometry (VSM) is the most common technique used in the semiconductor research community to measure the magnetic response of a material to the external magnetic field. VSM is a nondestructive sensitive technique and can detect small magnetization in the sample. In the VSM, the sample is placed on a vibrating stage and an external magnetic field is applied. This external field causes the sample to be magnetized in the direction of the applied magnetic field.   With the increase in the applied magnetic field, the magnetization of the sample increases. This increase (change) in magnetization results in creating a magnetic field around the sample due to its internal magnetic dipole moment. Since the sample is placed on a vibrating stage of fixed frequency, the flux through the pickup coils changes. This results in creating a current in the pickup coils which is proportional to the magnetization of the sample. To avoid any effect of external magnetization contribution towards the magnetization of the sample, the sample was placed inside a quartz tube during measurement. The magnetic properties of the samples were measured using the VSM option in DynaCool-14 Physical Properties Measurement System

19

(PPMS) from Quantum Design Inc. The sample surface was kept parallel to the applied magnetic field. A schematic of VSM is shown in Figure 2.8.
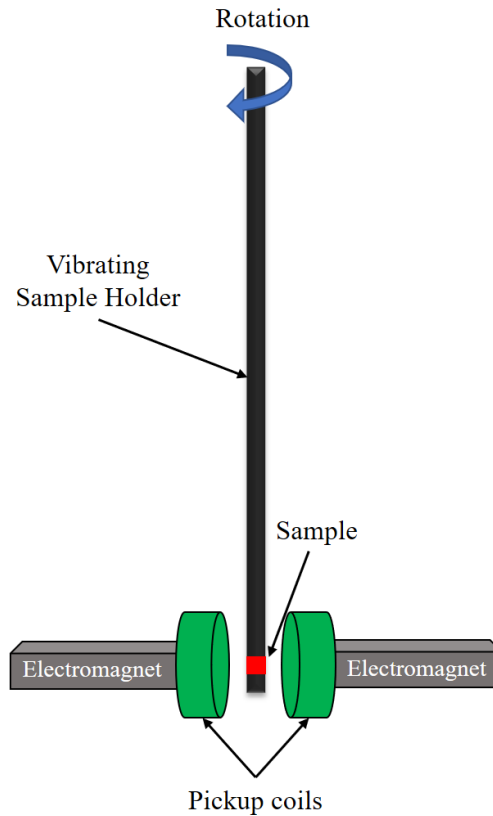
Figure 2.8: Schematics of VSM showing the sample location and other key components.

2.5   Atom Probe Tomography

Atom probe tomography (APT) is based on field evaporation of ions that can evaporate ions one at a time from the sample surface. A needled-shaped sample is prepared for APT measurement where the tip radius can be anywhere from 50-100 nm. The tip is then applied with a high voltage (0.5-15 kV) that creates an induced electric field at the surface. Then a small amount of energy is applied in the form of a pulsed laser that causes the atoms from the tip to evaporate one at a time. The tip is usually kept frozen (~50 K) during this process. The ionized atoms from the tip surface are then detected by a position-sensitive detector that can determine the X and Y

coordinate of the atoms. The Z coordinate of the atom is determined from the order of evaporation as the sample is evaporated as one atom at a time. By measuring the time of flight for each atom, the chemical composition of the sample can be found. Combining all the X, Y, and Z data and chemical composition, a full 3D reconstruction of the sample elemental composition can be made for further analysis. For this research, a Cameca Local Electrode Atom Probe (LEAP 5000 XS) instrument located at the UNT's MRF was used. A schematic representation of the Atom probe is illustrated in Figure 2.9.
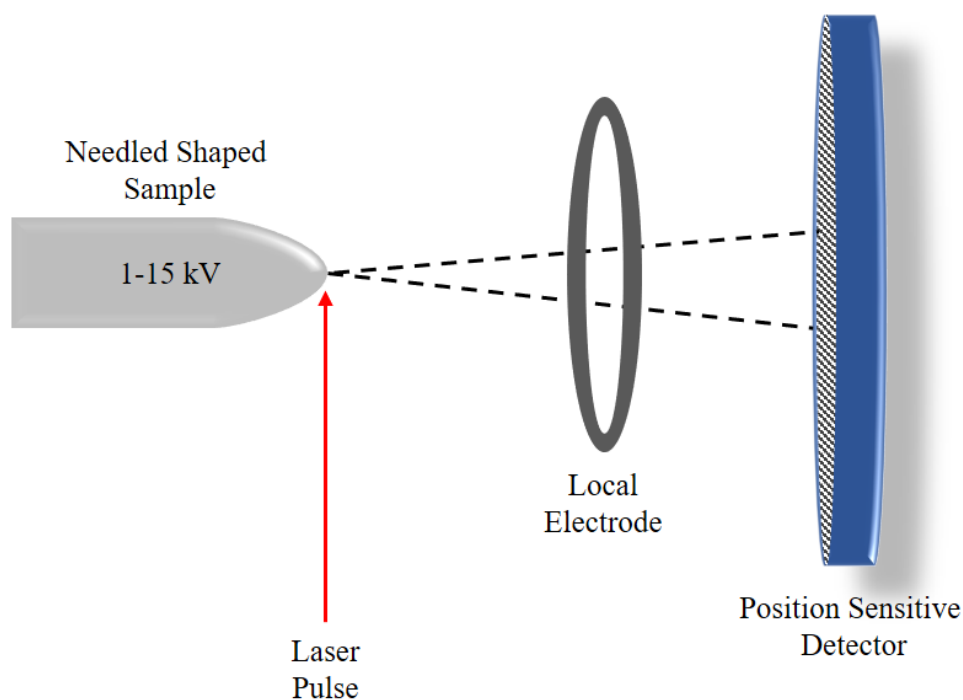
Figure 2.9: Schematic representation of atom probe tomography.

CHAPTER 3

A BRIEF INTRODUCTION TO MONTE-CARLO SIMULATION OF ION-SOLID

INTERACTION*

3.1   Introduction

To determine the distribution of ions implanted into the target, Monte Carlo (MC) based

simulations are frequently used. These MC simulations not only give information about the

distribution of implanted ions but also give the idea about the distribution of ion beam-induced

defects such as vacancies and interstitials created in the target. These MC simulation codes

calculate collision cascades by simulating binary collisions with a random distribution of impact

parameters. One of the most used MC codes is TRIM [44] (Transport and Range of Ions in Matter).

There are several variants of TRIM available for special applications. One example is TRIM.SP,

which is used for sputtering calculations due to ion irradiation. SDTrimSP [45] is mainly used for

dynamic variation in target composition with sputtering. In these MC simulation codes; one could

define the structure and morphology of the target. In "conventional" MC codes based on TRIM,

the target is defined by a stack of layers which is an infinite lateral extension. The use of these MC

codes is valid if one defines the target as a flat surface with a sharp interface. However, it is

impossible to represent nanostructures in these simulation codes. So, if one uses these codes to

simulate the results for nanostructures to obtain accurate distributions of implanted ions and

damage, then the code needs to be modified at the root level. In other words, the correct three-

dimensional (3D) structure and the surface of the target must be represented in the program already

during the simulation. This is especially true when the size of the nanostructure is in the same

---

*The content of this chapter is partially reproduced from S. Singh, B. Rout, Simulation Study of Surface Sputtering
and Distribution of Ions in Silicon due to Low Energy High-Fluence Cobalt Irradiation, **Surfaces and Interfaces, 24**
(2021) 101035, with permission from Elsevier.

range as the size of the collision cascade. Over the past years, many approaches have been used to simulate the ion irradiation of nanostructures depending on the application and the desired accuracy. For very small nanostructures, full molecular dynamic (MD) simulations can be performed. These MD simulations can inherently be much more accurate than the traditional MC simulations because they avoid approximations like binary collisions, and they can correctly simulate target temperatures above 0 K. But in the case of the MD simulations, it requires many orders more of computation time than MC simulations. Over the past few decades, many ion beam simulation codes have been developed that calculated the implantation profile and damage of the target. Here we have explained some of the ion beam codes used in this research and their background.

3.2   The Basic Theory of Ion Irradiation in the Low Energy Regime

The interaction of energetic ions with the target changes the physical and chemical properties of the materials. Two independent approaches have been adopted in the past to simulate ion-solid interactions. The first approach is the simulation based on molecular dynamics which can include the crystalline structure of the target. This method is less studied as the simulation process is time-consuming for high fluence irradiations [46–48]. The second approach is by using Monte Carlo simulation based on binary collision approximation (BCA). The second method is well studied by several researchers in the past as it allows faster calculation methods for irradiation. In the case of BCA, the ions travel through the target material by experiencing many independent collisions with the atoms in the target and it is assumed that the ions travel in a straight path in between the collision. In this study, we have used simulation codes based on binary collision approximation where the target is considered fully amorphous during the simulation. For our study, the ion range, and the distribution of ions in the target matrix plays the most important role. A brief

description of various ion-solid interaction terminology is discussed below along with a schematic represented in Figure 3.1.
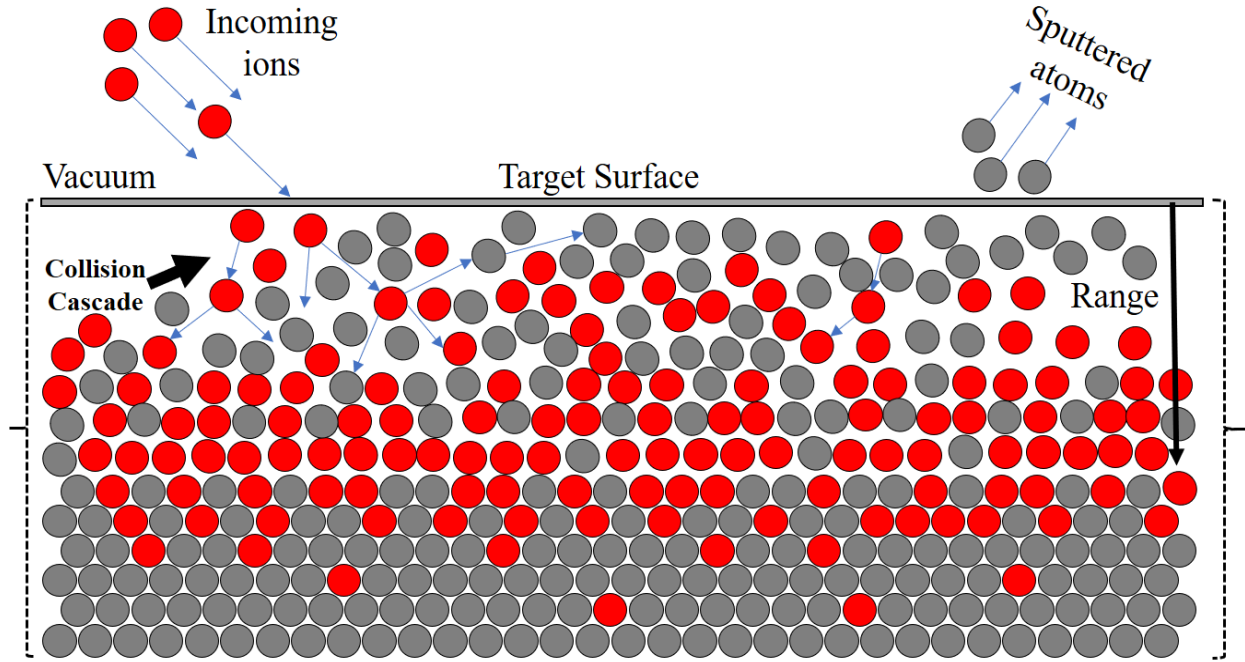
Figure 3.1: Schematic illustration of the ion-solid interaction process.

The range of the ion in a solid is defined as the average depth to which the ions can penetrate. It mainly depends on the energy loss of the ions in the solid. The mathematical expression for the ion range is given as,

$$R = \int_{E_0}^{0} \frac{1}{dE/dx} dE \qquad \text{(Eq. 3.1)}$$

The term dE/dx in the denominator corresponds to the total energy loss over the depth interval dx, it is also called stopping force, and E_0 is the incident energy of the ion. Calculating the ion range accurately is one of the most important factors in the case of ion beam modification. This accuracy of range greatly depends on the calculation of total energy loss by the ions in the solid. The energy loss can occur via two separate mechanisms called electronic energy loss and nuclear energy loss. Electronic energy loss refers to the loss of energy of the incoming ion to the electrons of the target

atoms. This is sometimes referred to as inelastic energy loss. This energy is responsible for the ionization of electrons in the target atoms. Nuclear energy loss refers to the loss of energy of the incoming ion to the target nuclei also called elastic energy loss. The nuclear collision can cause target atoms to be displaced from their regular lattice site. A single energetic heavy ion can create a collision or displacement cascade as shown in Figure 3.1. As a result, this effect can cause significant damage to the target structure. In the high energy range of the incoming ions (MeV energies), electronic energy loss is dominant. In this regime, the incoming ion moves almost in a straight path until it loses most of its energy to the target electrons. Once the energy decreases to a lower value (e.g. few tens of keV), the probability of collision of the ion with the target nuclei increases. At this point the nuclear energy loss dominates and the ion comes to a final stop after undergoing multiple collisions with the target atoms. The nuclear collision of ions can sometimes lead to the ejection of surface atoms from the target through the process of sputtering. The ion range in a solid mainly depends on the mass of the incoming ion, the energy of the incoming ion, the mass of the target, and the angle of incidence of the ion to the normal on the target surface. A detailed study of the angular dependence of range for 55 keV Co ion in Si will be discussed in Chapter 4.

The range and concentration of the implanted ions in a solid are also affected by the sputtering yield of the target. The sputtering yield is defined as the ratio of the total number of atoms sputtered from the target and the total number of incident ions. In this case, Sputtering is the removal of surface or near-surface atoms from the target. The angular distribution of sputtered atoms is far less studied than the distribution of energy of the sputtered atoms. Hence, the modeling study discussed in chapter 4 is focused on the angular distribution of sputtered atoms.

The sputtering of a target atom from the surface is affected by the surface binding energy

of the target material. The surface binding energy is defined as the amount of energy necessary to remove the atoms from the top layer of the target surface. Sputtering is not significant in the case of high energy implant but in the case of low energy (~tens of keV), it plays an important role in determining the distribution of implanted ions in the target. In the case of the low-energy heavy ions (Fe and Co) bombarded on a target species consisting of light elements (such as Si), the range of the implanted ion is about a few nanometers below the surface. During the implantation process, the ions collide with Si atoms which produces a primary recoil atom. This primary recoil induces series of cascades of low-energy secondary atoms inside the target. Towards the end of this cascade, some of the ions carry enough energy to remove the target atoms from their position near the surface. Once the near-surface atom in the target receives energy more than the surface binding energy, the atoms escape from the target surface to vacuum and contribute to the sputtering yield. Both the probability for the initial collision to occur near the surface and the average number of low-energy secondary recoils are quantities proportional to the number density of target atoms. In the case of a high-energy implant, this cascade occurs few micrometers (1-2 μm) deeper from the surface but in the case of low energy implant, it happens near the surface region. Some of the ions get backscattered or reflected by the Si atom and move back to the surface region of the Si while carrying a few eV of energy. In the case of heavy ions (such as Fe, Co, Ni, Xe, etc.) this energy is typically more than the surface binding energy of Si (4.7 eV). The surface binding energy is usually predefined in the simulation. When an ion with an energy more than the surface binding energy of Si collides with the atoms near the surface, it sputters that atom from the surface and takes its position as a replacement ion in the Si matrix. This type of sputtering which involves multiple collisions is sometimes referred to as indirect sputtering. The other type of sputtering that can occur is direct sputtering. The indirect sputtering is dominant for normal incidence and low angle

ion beam incidence on the target. The Sputtering of target atoms increases with an increase in ion fluence. The fluence is generally defined in terms of the number of ions per unit area. Choosing the right fluence, ion energy, and ion incidence angle are the key factors in determining the distribution of the implanted ions target. A summary of various ion-solid interaction codes used in this study is discussed in the following sections.

3.3   Transport of Ions in Matter

Transport of Ions in Matter (TRIM) is a well-known simulation code in the ion beam community which uses Binary Collision Approximation (BCA) Monte Carlo transportation which was written by J. P Biersack in the early 1980s [44]. It has a graphical user interface that allows the users to define the input parameter for the simulation and define the target thickness. In the output, it gives information about the depth profile, vacancies, deposited energy, etc. Accurate determination of the distributions of implanted ions in solid has been a topic of interest for decades, such as for dopant implantation in semiconductors, modification of physical properties of metals and insulators as well as understanding irradiation effects in solids. Ever since TRIM code was written, various developments have been built on this model. TRIM.SP was one of the first of these, whose SP designation came as a result that it could estimate sputtering yield. Another code built on TRIM.SP is the Transport of Ion in Dynamic (TRIDYN) material code, developed by Moller and Eckstein, also in the early to mid-1980 [49].

A static approximation of the simulation is only strictly applicable to systems with small particle fluence, where the effect on the material being bombarded is negligible, $\ll 10^{15}$ projectiles/cm^2. However, in most plasma processing applications, there is a very large fluence where the very point of the operation is to alter the surface material properties, or to etch away the surface, or to deposit a new one. To correctly study these with the TRIM type model, one needs a

code that keeps track of depth concentration profiles of the implanted particles as well as the particle migration of target atoms and then allows the target to change as a function of that incident fluence. TRIDYN has been developed to fulfill this need. The TRIDYN code has been around and under development in a variety of groups for over twenty years, and in that time has been applied to the topic as varied as fluence depended on sputtering yield, to fusion plasma-wall interaction to applications involving thin films. In this study, TRIM was used to simulate the energy loss by the heavy ions (Fe and Co) in Si and to simulate the depth profile of the ions implanted into a 100 nm layer of the silicon. Figure 3.2 shows a schematic representation of the geometry of the incident beam, target layer, and sputter atoms.
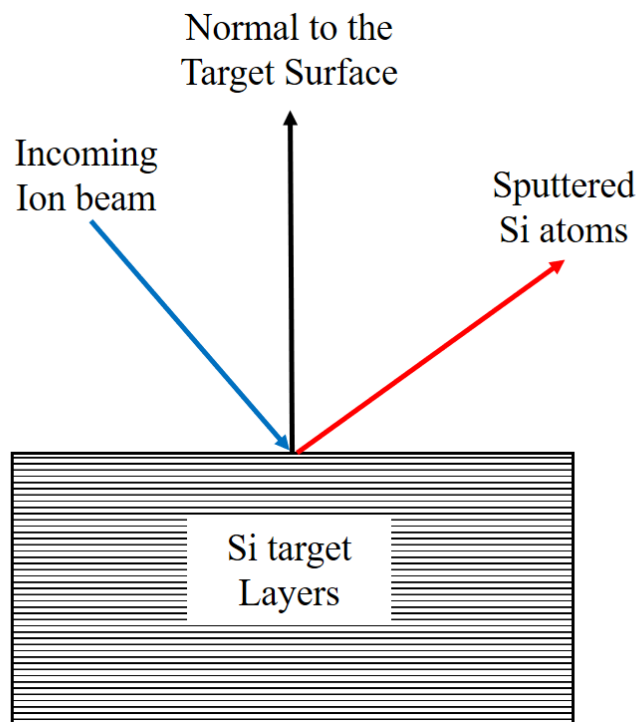
Figure 3.2: Schematics of the ion-solid interaction geometry used in TRIM and SDTrimSP Simulations codes are shown. The target is defined as a stack of layers of Si. The angle of incidence is calculated with respect to the surface normal.

3.4   General Description of TRIDYN Code

TRIDYN code can simulate the dynamic change of thickness and/or composition of a target

consisting of multiple elements during high fluence ion implantation or ion-beam-assisted deposition. It is based on TRIM, using the binary collision approximation (BCA) model for ballistic transport. The main fields of application of TRIDYN include high fluence ion implantation, ion beam synthesis, sputtering and ion mixing of polyatomic solids, ion-beam or plasma-assisted deposition of thin films, and ion-beam or plasma-assisted etching. The effects of ion irradiation such as ion scattering, reflection, sputtering, and ion mixing are computed for a target at 0 K. TRIDYN allows calculating the depth profiles of all atomic species in the target as a function of the incident fluence. Additionally, sputtering yields, total areal densities, surface concentrations, and re-emitted amounts are calculated as a function of fluence, as well as the surface erosion (when sputtering prevails) or the grown layer thickness (in the deposition regime). Due to the binary collision approximation, its lower energy limit is in the order of 10 eV. Nevertheless, experience shows that also collisional processes with slightly lower characteristic energies, such as sputtering, are predicted quite accurately. The upper energy limit is given by feasible times of computation. The TRIDYN is less suitable for energies in the MeV range and above. It does not contain a collision frequency reduction such as in TRIM for higher energies.

A newer version of TRYDN is available called Tri3dyn which allows complex three-dimensional (3D) targets for the simulation[50]. It can simulate the effect of ion irradiation in bulk as well as complex nanostructures.

3.5   SDTrimSP Code

Static Dynamic Transport of Ions in Matter Sequential and Parallel (SDTrimSP) [51] is an ion solid interaction code that is based on TRIM.SP and TRIDYN. It includes all possible output facilities like sputtering, backscattering, transmission, etc. This offers the opportunity to introduce at the same time a modular structure, to have a more flexible output, and to provide higher

portability. The program is suited equally well for all sequential architectures and for all parallel architectures, for which a Fortran 90 (F90) compiler and the MPI (Message Passing Interface) communication library are available. The new program also includes features that were used in the past but were not incorporated in most versions of TRIM.SP and TRIDYN. In SDTrimSP the target layer is constantly updated at a certain interval which can be set in the input file as sputtering modifies the target surface. It can simulate the atomic collisions in amorphous targets to calculate the ion range, sputtering yield, depth profile of implanted ions, energy distribution, etc. The target in the SDTrimSP code used in this research is one-dimensional like TRIM (Figure 3.2) where it is divided into several layers. In the static mode, the target is fixed (change in target composition is not considered during the simulation) whereas in the dynamic mode the composition of layers is updated after a fixed number of ions have been simulated. The number of ions after which the target surface is updated is specified in the input file for the simulation. In SDTrimSP code the coordinate system used is as follows. The beam is incident in the X-Y plane where X is the surface normal. The polar angle (β) is also in the same plane but calculated relative to the Y-axis. For this study SDTrimSP, 5.07 version was used.

3.6   Physical Description of Simulation

In TRIM, Tridyn, or SDTrimSP, the target is always defined as a one-dimensional stack of layers as shown in Figure 3.2. In the dynamical model (SDTrimSP and Tridyn) the thickness of target layers is changed after a certain number of ions are simulated as predefined in the input file.

The binary collision approximation is used to handle the atomic collision which means that the change in flight direction due to the collision is given by the asymptotes of the real trajectory. For this evaluation, an interaction potential must be chosen (usually purely repulsive and only dependent on the distance between the colliding atoms) to determine the scattering angle of the

30

moving atom and the recoil angle of the atom, which is set into motion. Then the energy loss of the moving atom and the energy gain of the recoil can be calculated. Also, a moving atom loses energy to target electrons (electronic or inelastic energy loss). The program also provides the possibility to include simultaneous weak collisions, but strictly in the binary collision approximation. The program follows projectiles (incident atoms) and target recoil atoms three-dimensionally until their energy falls below some preset value (usually in a few eV range) or if they have left the target (backscattering, transmission, sputtering).

In the case of the dynamic model, the simulation code treats the bombardment of incident ions on different target structures. Both incident ions and recoil atoms are treated as series of subsequent collisions. In the simulation, modifications of the target caused by the ion bombardment are considered; i.e the target is updated at regular intervals. The atoms are distinguished in projectiles (incident atoms) and recoils (target atoms). For each traced atom the important physical quantities, as energy, spatial coordinates, the direction of motion, are recorded along its path using general data structures. All these parameters can be extracted from the output file of the simulation.

3.7   Three-Dimensional (3D) Simulation to Incorporate the Curved Surface Geometry

In the previous sections we explained that for the "conventional" MC codes based on TRIM, the target is always defined by a stack of flat layers, which usually have infinite/periodic lateral extension. This way of defining the target limits the applicability of these MC codes to the ion irradiation of bulk targets or layered targets with a flat surface and flat interfaces. Nanostructures cannot be represented in these simulation codes, as they have a relatively curved surface, which is especially a problem for free-standing nanostructures. Nevertheless, these bulk simulations are sometimes used when irradiating a nanostructure with an ion beam. The simplest

way of adapting bulk simulations to nanostructured targets would be to take the distribution of implanted ions or the distribution of damage from bulk simulations and extract the desired shape of the nanostructures; however, this method does certainly not yield the most accurate results [52]. A more advanced method would be to take collision cascades simulated in bulk material and apply these cascades to the nanostructure while adjusting the correct point of entry where the ions hit the nanostructure surface. This method will also yield inaccurate distributions of implanted ions and damage. The surface of the nanoparticles cuts right through the collision cascade, but the influence of the surface on the collision cascade is neglected because the cascade was simulated for bulk. Errors are caused by ions or recoils, which move out of the defined structure and re-enter it, as well as the neglected influence of the surface binding energy at the nanostructure surface. Consequently, the correct curved surface of the target must be represented in the program, as an input file. This is especially true when the size of the nanostructure is in the same range as the size of the collision cascade. We will discuss the basic working principle of one simulation code (Iradina) in the next section that allows 3D target structure for the ion beam simulation. We have used only Iradina in this study though there are other 3D codes available.

3.8   Iradina Code

Ion range and damage in nanostructures (Iradina) is an ion beam simulation code that is specially used for ion beam irradiation of nanostructures. The Iradina code simulates the transport of ions through a target consisting of several cells using MC code. Several very fast routines are adapted from the open-source computer code ''Corteo''[53]. These fast routines account for significant savings in computation time compared to TRIM. First, the target structure and composition are defined in the input file of the program. Several materials, which are present in the target, are also defined in the input file, and each of these materials may contain any number

of different elements in arbitrary concentrations. The lattice binding energy E_b, displacement energy E_d, and surface binding energy E_s need to be defined for each element in each material. It is essential to correctly define these parameters as it affects the ion distribution in the target. In the input file, a rectangular box of desired size (comparable to the size of the nanostructure) is defined to describe the target. The box is again subdivided into equal-sized rectangular cells. Each cell can contain one of the defined materials or vacuum. Furthermore, each cell has several counters, to record how many ions are implanted into this cell and how much damage is produced (for example vacancies and interstitials of each type) which can be used later to the output result of the ion beam simulation. An ion is described at any time by its momentary position in the target, its energy, and its moving direction (the velocity vector normalized to unit length). Each ion is followed through the target until it leaves the target or until it is stopped within the target (meaning it has lost all its energy).
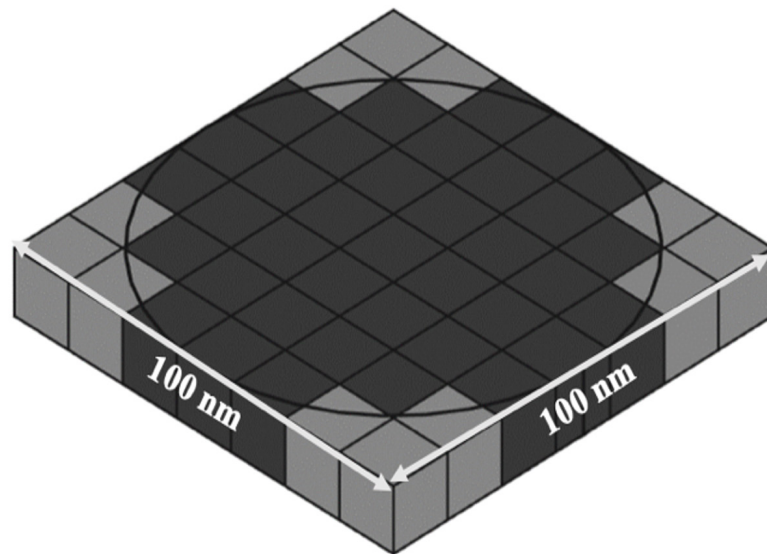
Figure 3.3: Schematics of the target structure for the Iradina simulation where the target was divided into 1 nm × 1 nm × 1 nm cube.

This minimum energy is also defined in the input file which is typically in the order of a few eV. Depending on the ion's momentary position, the material is determined in which the ion

currently moves. A flight length is selected randomly according to a Poisson distribution, such that the mean flight length corresponds to the average atomic distance within this material. The logarithmically scaled stopping tables from the Corteo code are used, because they offer the advantage of extremely fast access, by utilizing a neat indexing mechanism, which avoids the lengthy calculations of logarithms [54]. After a predefined number of ions has been simulated, the code stores the cell counters as 3-dimensional histograms of ion and damage events, from which the distribution of implanted ions and the distributions of the various types of damage can be extracted.

3.9   Conclusion

In summary, for the case of 1D codes, the target was divided into 1nm layers stacked on each other with X and Y periodic boundary conditions. The target layer was kept constant ($\Delta X \sim$ 1 nm) for TRIM and SDTrimSP for a consistent comparison. In the case of 3D codes such as Iradina, the target was divided into 3D grids (cubes) of a dimension of 1 nm with a total cell volume of 1 nm^3. The periodic boundary condition was applied in the Z direction (along the length of the NW) and X, Y was given a specific value. The NW was surrounded by the second material, in our case vacuum, to keep track of the target atoms and/or ions that are leaving simulation volume to accurately calculate the sputtering of Si. The TRIM simulations were carried out on a personal computer with Intel i7 4000 series processor. However, the SDTrimSP simulation was carried out on a supercomputing cluster (Talon 3.0) available at high performance computing center of UNT. A single node of Talon 3.0 with 28 cores was allocated to the process. The supercomputing node used for this simulation was comprised of a Dell PowerEdge C6320 server with two 2.4 GHz Intel Xeon E5-2680 v4 fourteen-core processors. For both the simulation, the input parameters were kept identical to ensure the consistent output of the simulation result. The simulations using Iradina

code were carried out on a personal computer Intel i7 4000 series processor as Iradina is very fast in performing the simulations. Several very fast routines for Iradina code are adapted from the open-source computer code "Corteo", which was originally written by F. Schiettekatte [55]. These fast routines account for significant savings in computation time compared to TRIM.

CHAPTER 4

SIMULATION STUDY OF SURFACE SPUTTERING AND DISTRIBUTION OF IONS IN

SILICON DUE TO LOW ENERGY HIGH-FLUENCE COBALT IRRADIATION*

The study of the range and distribution of low-energy heavy ions implanted into lighter substrates is paramount important in terms of three-dimensional device fabrications. In this study, we report the re-distribution of implanted ions due to the sputtering of target atoms, simulated considering dynamic changes in the target due to the high-fluence irradiation of Co and Fe ions at low energy (55 keV) in silicon substrate. The simulations were compared by using various ion-solid interaction codes that are capable of incorporating the targets with dynamic changes. In the static simulation code, the target is generally defined as a stack of sharp interfaced layers that have an infinite lateral extension where the composition is constant throughout the simulation. Both static code like Stopping and Range of Ions in Matter (SRIM) and dynamic code like Static and Dynamic Trim for Sequential and Parallel computer (SDTrimSP) were utilized to carry out the simulations in silicon substrates. The energy of the ion was kept constant for all the simulations. The fluence of the Co ions was then varied to obtain the optimal distribution of implanted ions in the silicon substrates. The simulated concentration of implanted ions in silicon using static code was higher compared to the dynamic code. In the case of dynamic code, the simulated sputtering and depth distribution was close to the various reported experimental studies. In the case of the Si substrate, the atoms are found preferentially sputtered in the forward direction between 30º - 60º angle with a peak around 45º angle to the target surface normal.

4.1   Introduction

The ion beam synthesis technique is used as one of the important tools for the synthesis and processing of nanostructures in semiconductor devices. Structural modification and doping of the nanostructures (e.g. semiconductor nanowires) using low energy (5 keV – 100 keV) ion beams can significantly enhance their functional properties [56–58]. Because of readily available high-performance computing resources, nowadays it is possible to design and optimize the experimental parameter utilizing ion-solid interaction simulation code before carrying out the actual experimental process. To study the distribution of ions in the target materials, several Monte Carlo technique-based simulation codes had been developed over the years. Some of the widely used codes like Stopping and Range of Ions in Matter (SRIM) [59], Static and Dynamic Trim for Sequential and Parallel computer (SDTrimSP) [51], and TRIDYN [60] generally defines the target materials as a stack of sharp interfaced layers which has an infinite lateral extension or one dimensional (1D) in nature. Recently simulation codes like TRI3DYN [61], Iradina [62], and IM3D [63], etc. have been developed with the capability of including three dimensional (3D) target structure in the input file. These simulation programs have been used by several researchers in the past to successfully modify and analyze the properties of materials due to ion irradiation. SRIM has been widely used by the researcher to study the depth profile, target damage, energy loss, etc. due to the effect of ion irradiation [64,65]. Even though SRIM is the most widely used code in the ion beam community, it does not incorporate the dynamic changes in the target composition during a single simulation. On the other hand, SDTrimSP includes the dynamic changes in the target composition and updates the changes in the target composition periodically during the simulation of ion irradiation. Recently many researchers have reported the study of heavy-ion irradiation in lighter substrates where the results from SDTrimSP simulation show close agreement with the

experimental data. Here we have discussed a few of those cases where SDTrimSP code has been successfully used.

Kalanov et al. have successfully used SDTrimSP to simulate the effect of 1 keV Ar and Ne ion irradiation on Si at a fixed angle of 60° [66]. Their study involves the investigation of energy distributions of both sputtered and scattered ions in the ion beam sputtering process of Si. In this study, they have estimated the distribution of energy of the secondary particles as a function of scattering angle. They have reported the simulated energy distributions of sputtered Si atoms and scattered Ne particles to the target composition for a fixed ion energy (1 keV) and a fixed angle of incidence (60°). The experimental data shows good qualitative agreement with the simulated energy distributions and the presence of direct scattering and sputtering. Additional simulations show that a 10% variation of the contribution of the target composition does not lead to significant differences in the energy distributions of sputtered and scattered particles. Bundesmann et al. have reported the study of the energy distribution of secondary particles (sputtered target and scattered particles) for the ion beam sputtering of TiO_2 in a reactive oxygen atmosphere [67]. For the simulation, they have used 1 keV Ar and Xe ion incident at 0°, 30°, and 60° angle on the target. The simulated results from SDTrimSP show good agreement with the experimental results. The simulated curves of the sputtered primary particles match the principal shape of the experimental data qualitatively. The simulated energy distributions of the scattered primary particles are very similar but much lower in absolute counts. Arredondo et al. have reported the study of angle-dependent sputter yield measurements of 2 keV deuterium (D) ions on W and Fe targets and compared it with the simulation results from SDTrimSP. The sputter yield data from the smooth Fe thin films show quantitative agreement with the SDTrimSP simulations in all cases. The sputter yields from the smooth W thin films agreed quantitatively with the SDTrimSP simulations in all

cases except under normal incidence, where a discrepancy of a factor of two was observed [68].

Stadlmayr et al. have used SDTrimSP-2D to simulate the sputtering of Fe due to the irradiation of 500 eV Ar ions incident at 60˚ angle and for a fluence up to 8×10^{17} ions/cm^2. They have reported the fluence dependence of surface morphology modifications on the sputtering yield of Fe thin films and compared the experimental results with the simulated results [69]. Eswara et al. have simulated the effect of 25 keV He and Ne ion irradiation in Carbon slabs of various thicknesses with a fluence of up to 10^{18} ions/cm^2 where the ions are incident normally ($0˚$ to the surface normal) to the sample. They have investigated the effect of 25 keV He$^+$ and Ne$^+$ ion irradiation of multi-walled carbon nanotube to study the influence of fluence and sample thickness on the irradiation-induced damage. [70]. Backer et al. have used SDTrimSP code to simulate the collision cascades and target damage. They have studied the primary damage in tungsten (W) by using the binary collision approximation, molecular dynamic simulations, and the density functional theory [71]. Lisa et al. have reported the molecular dynamics (MD) simulations of low energy (10 - 100 eV) D irradiation on W, WC, and W$_2$C surfaces. In this study, they have compared MD and SDTrimSP results regarding the C sputtering as a function of the C content of the target. They have used SDTrimSP to simulate the effect of 50 eV and 100 eV deuterium on C and WC, both in the static and dynamic model of the program for various ion fluences [72]. Plank et al. have Studied the temperature-dependent nitrogen retention in tungsten surfaces using X-ray photoelectron spectroscopy. In this study, they have used SDTrimSP to simulate the depth profile of 300 eV N atoms implanted in W at an angle of 45° to the surface normal [73]. Mutzke et al. have studied the Ion fluence dependence of the Si sputtering yield by the bombardment of ions of noble gases (He, Ne, Ar, and Xe). The bombardment of Si with the noble gases was simulated using SDTrimSP at normal incidence for an energy range of 1 to 500 keV. The results show good agreement with the

experimental data [74]. Recently, Hofsäss et al. have reported a comparison of simulation data from SRIM, TRIDYN, and SDTrimSP codes with the experimental data of sputtering of target atoms. The report has shown that SDTrimSP can describe different features of ion beam erosion quantitatively and in good agreement with many experimental data [75].

In this chapter, we have reported a detailed simulation study of the dependence of sputtering yield, ion distribution, and range on the angle of incidence and fluence for 55 keV Co implantation in Si substrate and Si nanowires. The simulated result from the static-code TRIM showed that the concentration of implanted ions is higher with an increase in the angle of incidence to the surface normal but in the case of the simulation carried out with dynamic-code SDTrimSP, the concentration of the implanted ions decreases with an increase in the angle of incidence. For a normal incidence, TRIM simulation shows the peak concentration of Co is 80 % in Si whereas, the simulations utilizing the Iradina and SDTrimSP codes show the peak concentration of Co as 60% and 48% respectively. We have compared the results of various simulation codes for Fe or Co ion-implanted into both Si substrates. The novelty of this study is, for the low-energy heavy ion-implanted into a lighter substrate, the accurate estimation of the sputtering of the target atoms as well as the implanted ions is important for high-fluence implantation. The ion-solid interaction simulation codes (e.g. SDTrimSP) which are capable of incorporating dynamic changes in the target matrix can be efficiently used to determine the saturation in the concentration of the implant atom as the rate of surface sputtering and implantation-induced deposition attain an equilibrium state. The results of these simulations can be utilized for facilitating the synthesis of ternary metal-silicon alloy nanostructures at a targeted depth of the substrate. This study is entirely based on simulation and explains the effect of various input parameters on the distribution of implanted ions and the sputtering of the target material.

4.2   Results and Discussion

4.2.1   Results from SRIM vs SDTrimSP

The distribution of implanted ions in a substrate is mainly dependent on three important factors, ion energy, angle of incidence, and fluence. However, in the case of lower energy implantation (< 100 keV), sputtering plays an important role in determining the distribution of implanted ions in the target matrix. The surface sputtering greatly depends on the energy loss of ions in the solid. The electronic vs nuclear energy loss of cobalt ions in silicon at various energies is shown in Figure 4.1 (a).
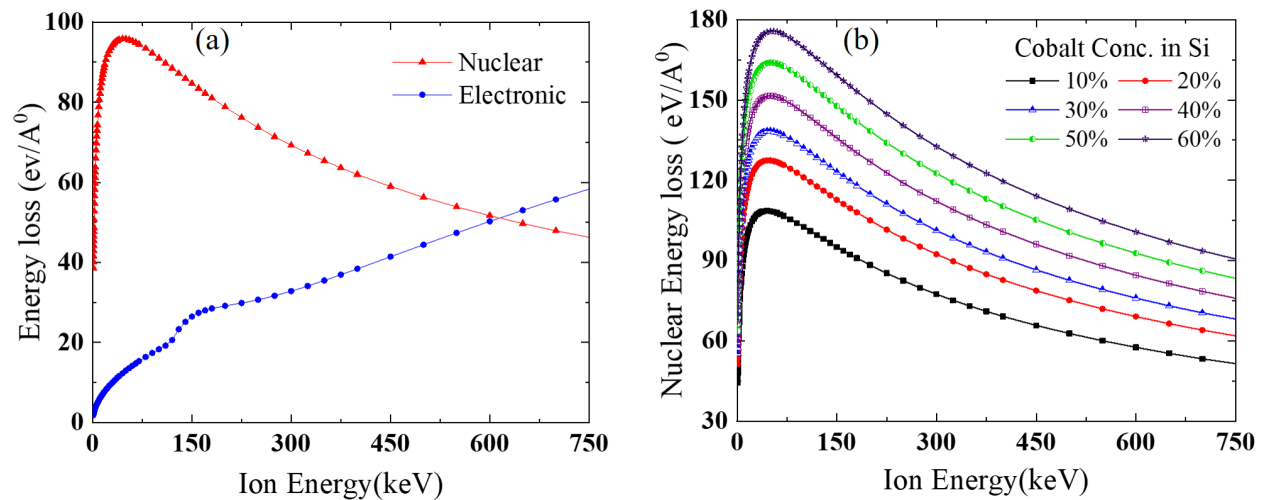
Figure 4.1: Electronic vs nuclear energy loss of Co ions implanted into Si substrate (a) up to an energy of 750 keV showing the regions of dominance. Nuclear energy loss of Co implanted in a target containing various concentration of the Co in Si (b) simulated for various range of ion energy using the SRIM code.

The result shows the dominance of nuclear energy loss in the low energy region. For a 55 keV Co ion in Si, the electronic energy loss is about ~ 17 electron-Volt/Angstrom (eV/A°) whereas the nuclear energy loss is about ~ 95 eV/A°. In this case, the nuclear energy loss is roughly 5.5 times the electronic energy loss. The nuclear energy loss changes as the composition of the target matrix are changed. The simulated nuclear energy loss of Co at various target compositions is shown in Figure 4.1 (b). The result shows a significant increase in nuclear energy loss as the

concentration of Co increased in the Si matrix. The nuclear energy loss increases from $\sim$ 95 eV/A^o to $\sim$ 180 eV/A^o with an increase of Co concentration from 0 % to 60 %. This happens because the probability of collision between Co and Si increases with an increase in Co concentration in Si which contributes to the energy loss. This effect is important as it is responsible for the sputtering of the target surface during the irradiation which is discussed in the following sections.

4.2.2   Angle Dependence of Sputtering and Ion Distribution

To study the effect of angle of incidence on the distribution of ion in the target and sputtering of the target surface, several simulations were carried out. Figure 4.2 (a) represents the simulated depth profile of 55 keV Co implanted in Si for various angles of incidence using TRIM. The results were scaled for a fluence of 2×10^{17} ions/cm^2.
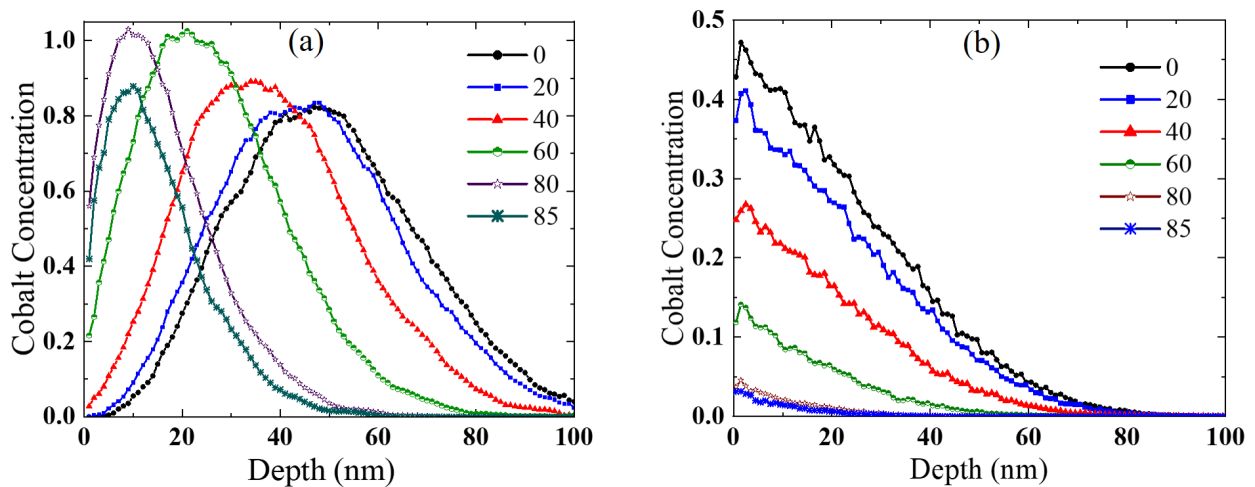
Figure 4.2: Angle dependence of depth profile for 55 keV Co implanted in Si with a fluence of 2 × 10^{17} ions/cm^2, simulated using the (a) static SRIM code, (b) and dynamic-SDTrimSP code.

The results showed that with an increase in the angle of incidence, the range of the peak concentration shifts towards the surface region. The range of the peak concentration decreased from $\sim$55 nm for 0° incidence to $\sim$ 10 nm for 80° incidence of the Co beam. The peak concentration also appears to increase relative to the normal incidence concentration with an increase in the angle of incidence. The depth profile is sharp for a higher angle of incidence whereas it is broad for the

low angle of incidence. The simulated depth profile using SDTrimSP is shown in Figure 4.2 (b). These results show a much different trend than TRIM simulations. The highest atomic percentage of Co to Si occurs for the low angle of incidence (0°- 10°) to the surface normal. The atomic percent of Co decreases with an increase in the angle of incidence. The concentration decreased below 10% for the angle of incidence beyond 60°.
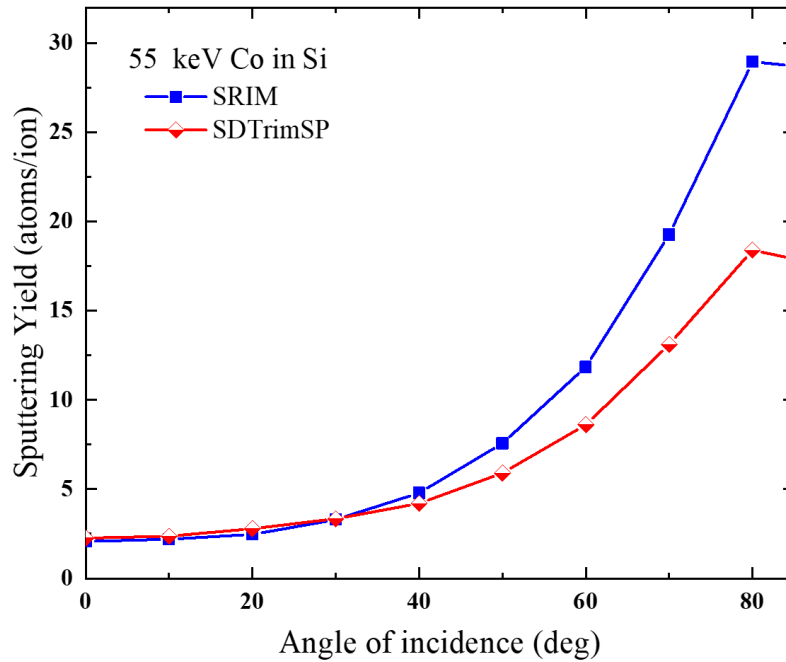
Figure 4.3: Sputtering yield of Si atoms as a function of angle of incidence of the 55 keV Co ion implanted into the Si substrate, simulated using SRIM and SDTrimSP codes.

In the case of TRIM simulation, no dynamic effects such as a change in the target composition due to the surface sputtering are considered for simulating the depth profile. However, for irradiation at higher incident angles, surface sputtering is significant. Due to the sputtering of both implanted ions (self-sputtering) and target atoms (Si), the implanted ion concentration is significantly low in the case of SDTrimSP. At these angles, the target particles get sputtered from the surface rather than getting implanted. Hence, the incoming ion contributes more towards the sputtering and less towards the implantation resulting in less concentration of implanted ions and

puts a limit on the maximum implant concentration that can be achieved. The dependence of the sputtering yield of Si for 55 keV Co irradiation on the angle of incidence is shown in Figure 4.3.

The result showed that both the sputtering yield have similar values for the low angle of incidence up to 30º but deviate at higher angles. The sputtering yield in both cases increases with an increase in ion incidence angle. There is a sharp increase in sputtering yield for the incidence angle between 50º to 80º. Then it starts to decrease with a further increase of the ion incidence angle. For higher angles, the energy deposited by the ions occurs close to the target surface. Hence direct sputtering is dominant. Secondly, with further increase in the ion incident angle (> 80º) the ions get reflected from the surface rather than getting implanted into the substrate. So, the ions are not able to transfer their energy to the target atoms which results in a decrease in the sputtering yield. It is better to explain the sputtering phenomena in terms of partial sputtering yield which refers to the sputtering of each atom or ion species for the irradiation process.

The total sputtering yield of a compound is related to the partial sputtering yield as the sum of the partial sputtering yield of all the constituent atoms (Co and Si in this case). The partial sputtering yield (atoms/ion) is defined as the following in our case,

$$\text{Partial Sputtering Yield } (Y_{Co}) = \frac{\text{Number of Cobalt atoms Sputtered}}{\text{Total Number of Incident Ions}}$$

Figure 4.4 represents the partial sputtering yield of 55 keV cobalt incident on Si for different angles of incidence as simulated using SDTrimSP code. In this case, the partial sputtering yield corresponds to the sputtering of the constituent atoms (Si atoms and Co ion) from a compound target. Even though pure silicon was considered as a target material as the starting point, the target composition was changed dynamically to make a realistic implantation process during the implantation. The results showed that for the low angle of incidence the partial sputtering yield increases with the ion fluence and reaches a concentration saturation around a fluence of 1.8×10^{17}

ions/cm^2. With further increase in the angle of incidence of the beam, saturation occurs at lower fluences. This implies that the concentration of Co in Si will be lower for higher angles of incidence. This can be seen also in Figure 4.2 (b), which shows the decrease in implant concentration with an increase in the angle of incidence. The general trends of the sputtering of elemental targets, such as Si, in this case, depend on the collision between the ion beam and the target atom. In our case, the bombardment of Si by Co at a fluence of 2×10^{17} ions/cm^2 causes the sputtering of Si from the target materials and a maximum of 48 % Co atoms replaces the Si atoms at the target surface when the ion is incident perpendicular to the target surface.
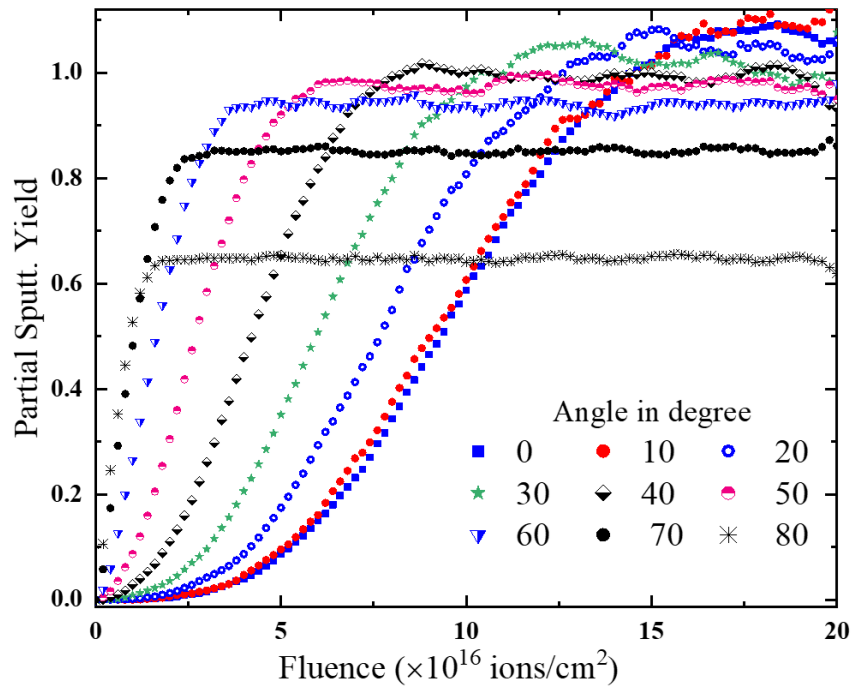
Figure 4.4: Partial sputtering yield of Co for various incident angle represented as a function of incident ion fluence for 55 keV Co implanted in Si simulated using SDTrimSP code.

Figure 4.5 shows the relation between incident ion fluence and the retained concentration of the implants for 55 keV Co into Si for the various angles of incidence. The simulation shows that the retention fluence increases with incident fluence for lower angle implantation before coming to a saturation value. In the case of high-angle implantation, this saturation happens much

faster. For the higher angles, even though the incident fluence is increased, the ions are not retained in the substrate. They are rather sputtered or reflected from the target surface. The simulated saturation fluence for reaching an equilibrium condition can be approximately determined from the fluence dependence of the sputtering yield. At this fluence, the number of particles implanted is the same as the number of particles sputtered from the target. This saturation fluence depends on the ion incidence conditions such as ion energy and angle of incidence. For fixed ion energy, it decreases with an increase in the angle of incidence of the ion which can be seen in both Figures 4.4 and 4.5.
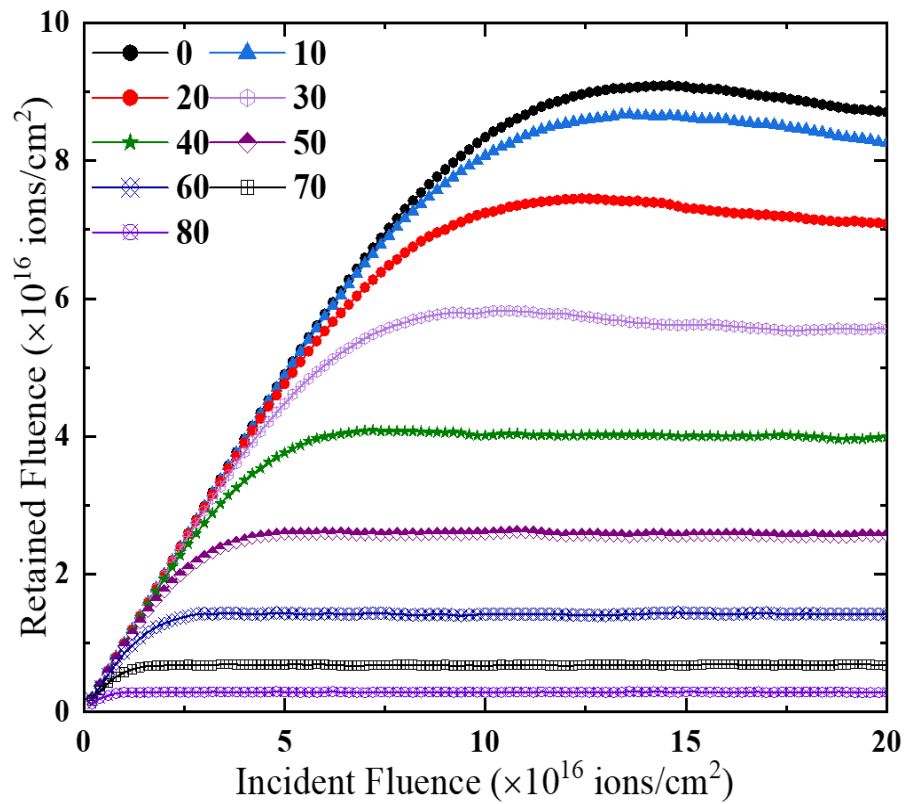
Figure 4.5: Incident fluence vs the retained fluence by the central layer of the target as a function of incidence fluence for 55 keV Co implanted in Si simulated using SDTrimSP code.

The decrease in the saturation fluence is a consequence of the increasing sputtering yield at higher angles. In a previous study of sputtering, Eckstein et al, have introduced a term called equilibrium fluence "f_{eq}". It was assumed that the steady state fluence is reached faster with an

increasing sputter yield and a decreasing range of the incoming projectiles. The f_{eq} can be expressed as,

$f_{eq} = \rho R_{eq}/Y$, where ρ is the target density, R the mean range of the projectiles and Y the total sputter yield" [76].

The saturation fluence has been calculated using the above expression and compared to the SDTrimSP simulation. The results are shown in Table 4.1. The results seem to agree for the lower incident angles but deviate at higher angles.

Table 4.1: Analytically calculated vs simulated saturation fluence for 55 keV Co ion in Si simulated using SDTrimSP code.

Angle of Incidence	Sputtering Yield (Y_{tot})	Range in nm (R)	$f_{eq} = \dfrac{\rho R}{Y_{tot}}$	Simulated f_{eq} SDTrimSP
0	2.26	80	1.77×10^{17}	1.75×10^{17}
10	2.36	80	1.73×10^{17}	1.70×10^{17}
20	2.79	75	1.34×10^{17}	1.45×10^{17}
30	3.34	70	1.05×10^{17}	1.20×10^{17}
40	4.2	65	7.73×10^{16}	7.70×10^{16}
50	5.9	60	5.08×10^{16}	6.20×10^{16}
60	8.61	45	2.61×10^{16}	3.00×10^{16}
70	13.1	40	1.52×10^{16}	1.80×10^{16}
80	18.4	30	8.14×10^{15}	1.90×10^{16}

Another effect in the case of heavy-ion implantation is the oscillation of sputtering yield. In the study reported on oscillation by W Eckstein, the calculations were performed for the bombardment of Be, C, and Si with W, and of C with Au, Ag, and Cu in the energy range of 1–500 keV and for various angles of incidence [77]. This oscillation was not observed in our case. Typical oscillation in the sputtering yield has been reported for a higher mass ratio ($M_2/M_1 > 5$) and a lower angle of incidence [78]. For our case, the mass ratio is smaller compared to the reported studies on the oscillation of sputtering yield. For the Co-Si case, the mass ratio between the target and the incoming ion is ~ 2.1. The SDTrimSP code offers the possibility to simulate the distribution of sputtered atoms as a function of the polar emission angle.
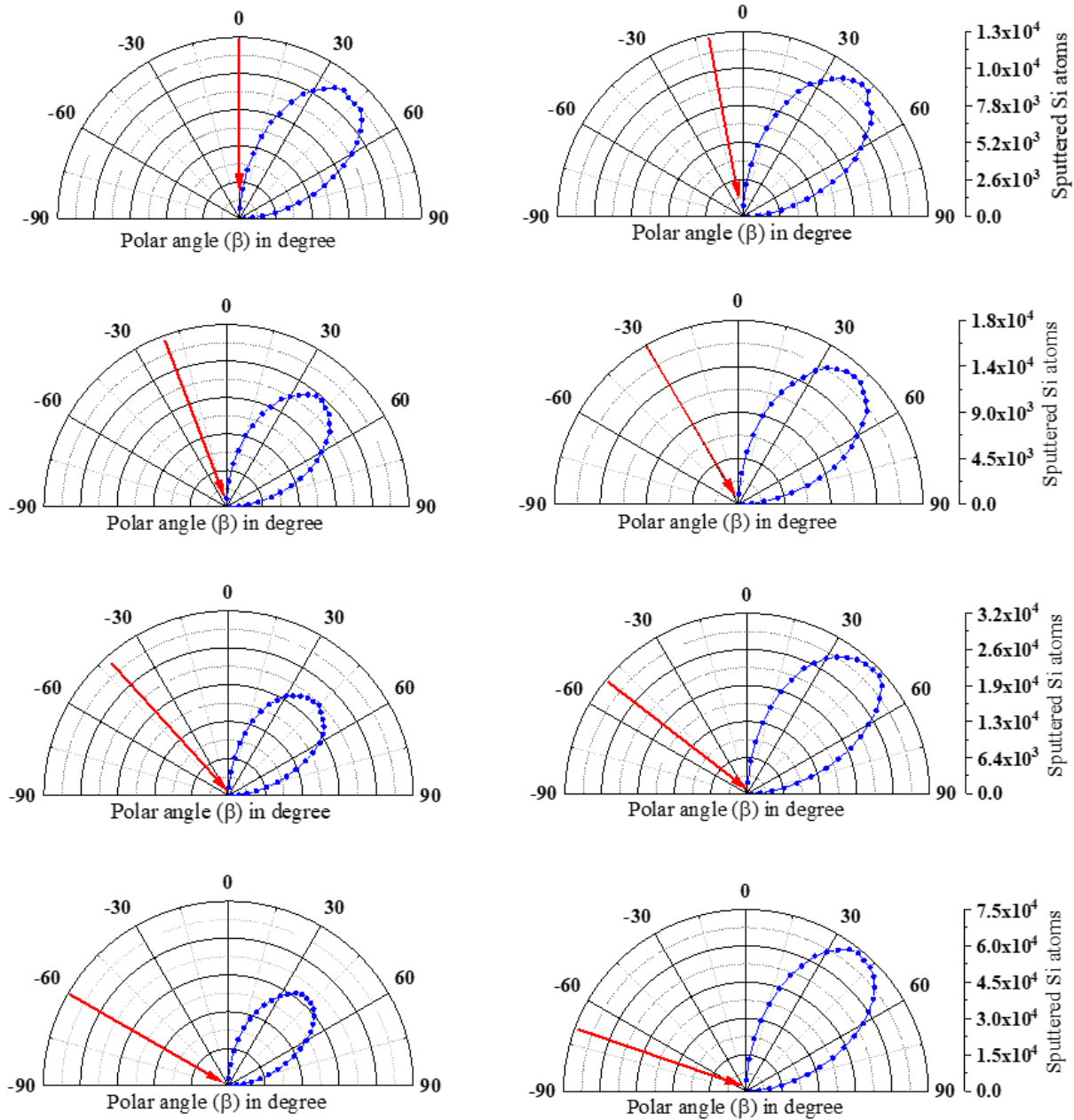
Figure 4.6: The polar plot shows the simulated angular distribution of sputtered Si atoms due to the 55 keV Co ion irradiation. The red arrow indicates the direction of the incoming ion beam. The angle of incidence of the ion beam was increased in each case by 10° up to 70° and corresponding distributions of the sputtered atoms were plotted. The scale (amount of sputtered yield of Si) is different in each row which indicates the increase in number of sputtered atoms with increase in angle of incidence of the beam.

Figure 4.6 represents the distribution of simulated sputtered atoms as a function of the polar

angle. In this case, various simulations were carried out by changing the angle of incidence of the

ion beam whereas keeping the rest of the simulation parameter constant. The results show that the number of sputtered atoms increases with the increase in the angle of incidence. However, the atoms are sputtered in the forward direction between 30°- 60° with a peak around 45°. The sputtering at a lower angle of incidence is due to the indirect sputtering whereas at a higher angle it is caused by direct sputtering due to the incoming ions.

The surface erosion of Si occurs due to the low energy incident Co ion. The simulated surface erosion as a function of the ion incident angle is shown in Figure 4.7. The surface erosion appears to follow the trend of the sputtering yield as shown in Figure 4.3. The erosion increases with an increase in ion incident angle and ion fluence. It starts to decrease when the incident angle is more than 80°. Each simulation was carried out for a particular angle and the surface erosion was noted for each ion incidence angle. For a higher angle, a greater number of particles get reflected from the surface than contributing towards the sputtering of Si
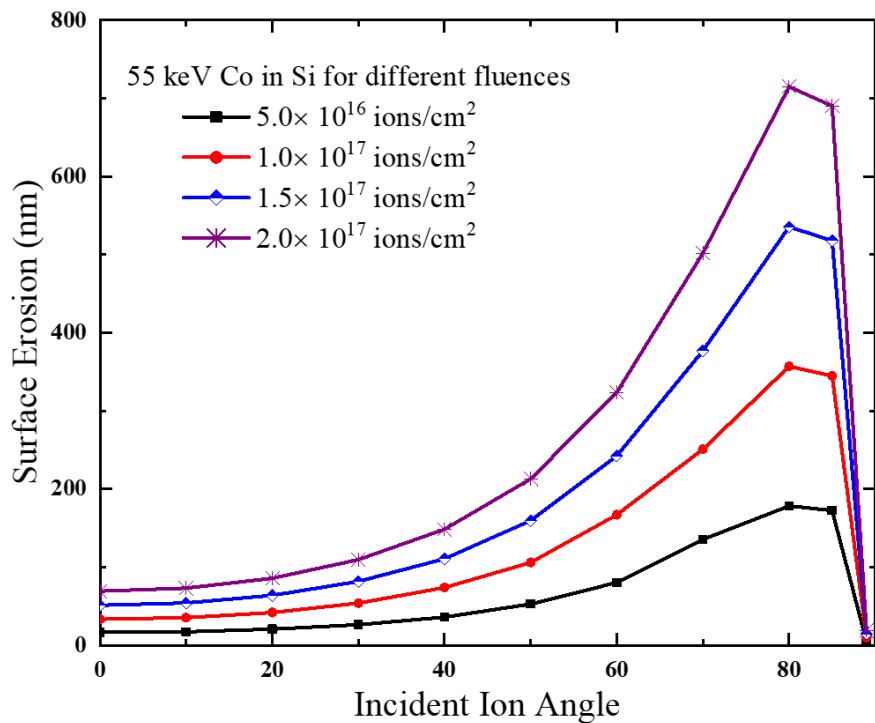
Figure 4.7: Surface erosion vs angle of incident for a 55 keV Co ion implanted into Si simulated for four different fluences using SDTrimSP code.

4.2.3 Simulation Results for a Sequential Implantation

For a sequential implant, SDTrimSP offers the possibility to include the elemental depth profile of the first implantation simulation to be used as an input target for the second simulation. In this case, a simulation of sequential implantation was carried out for 55 keV Fe implanted in the first implanted Co-Si matrix. For such a case it is important to consider the effect of sputtering due to the incoming ions from the first implant as it affects the distribution of ions in the target for the second implant. Another important factor to consider is the presence of implanted ions, more specifically the concentration of ions from the first implant in the target matrix, as the previous simulation suggests that the nuclear energy loss is greatly affected by this (Figure 4.1 (b)) which ultimately affects the sputtering yield and the final distribution of ions in the target. The partial sputtering yield of 55 keV Fe implanted into the Co-Si matrix is shown in Figure 4.8.
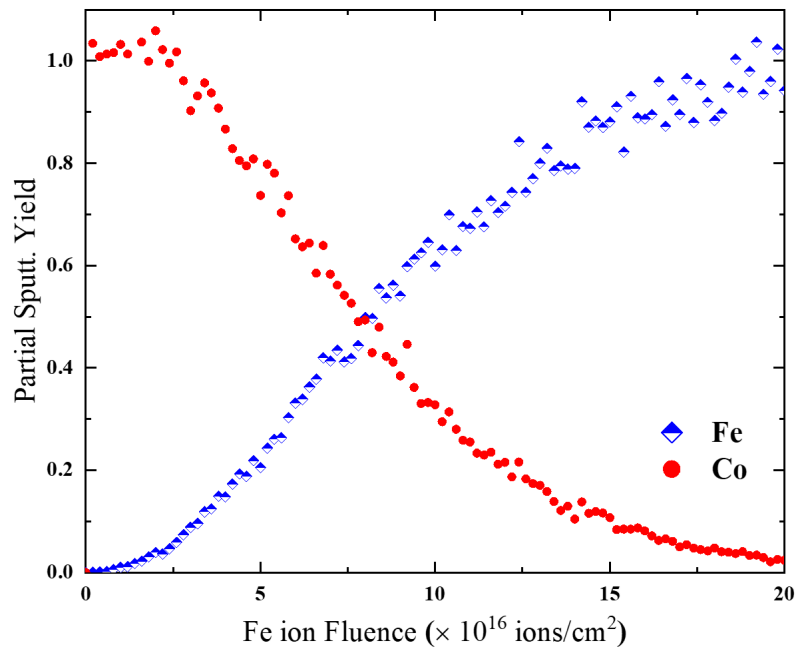
Figure 4.8: Partial sputtering yield of both Fe and Co as a function of ion fluence for 55 keV Fe and Co both implanted sequentially in Si simulated using SDTrimSP. First the simulation of Co implanted into Si was carried out and then the simulation was carried out of Fe implanted in to Co-Si matrix generated from the previous simulation.

For this simulation, both the ions were incident at 0º to the normal of the target surface. The first simulation was carried out for 55 keV Co in Si and then the second simulation for Fe was performed by utilizing the output result of the first simulation. The results show that the partial sputtering yield of Co decreases with an increase in Fe fluence. The partial sputtering yield of Fe increases with the increase in ion fluence. Around a fluence of 7.5×10^{16} ions/cm^2 both Fe and Co have the same sputtering yield. With further increase in the fluence, the Fe sputtering yield dominates over Co. This type of behavior affects the deposited concentration of each ion in Si.
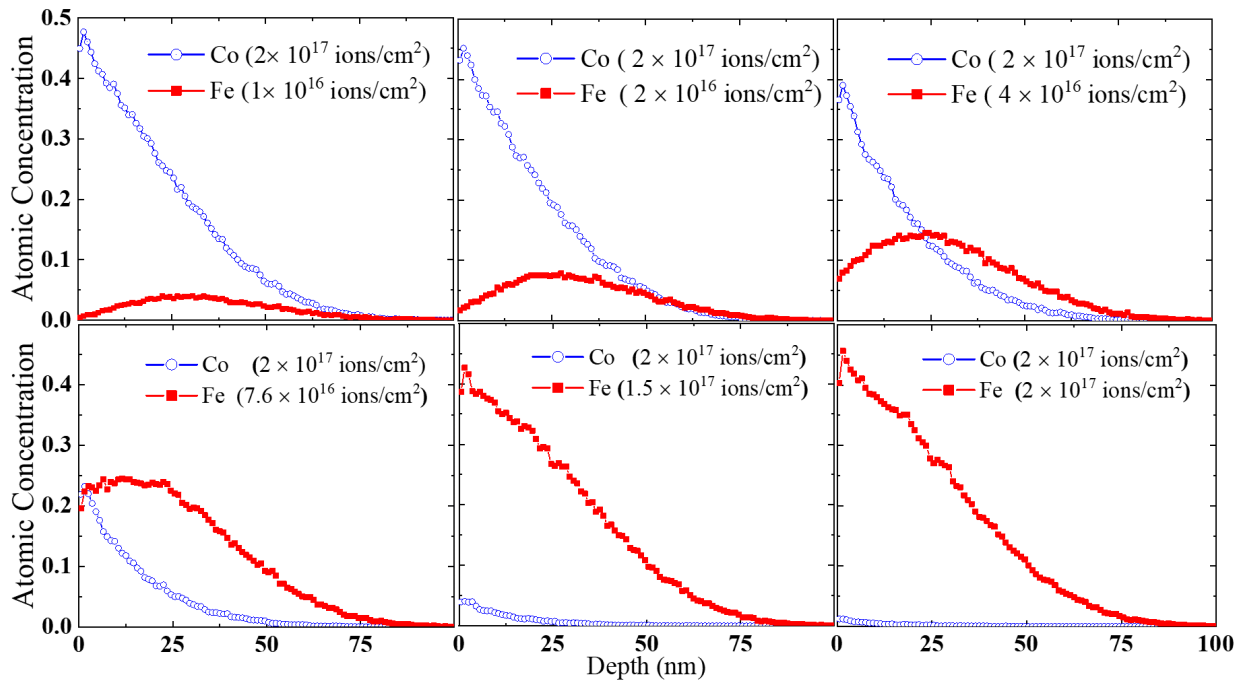
Figure 4.9: Simulated depth profile of 55 keV Fe in Co implanted Si simulated using SDTrimSP code for various ion fluences.

The depth profile of the sequential implantation of both Fe and Co is shown in Figure 4.9. For this simulation, both ions were implanted at 55 keV energy and simulated for a various fluence of Fe up to a fluence of 2×10^{17} ions/cm^2 while keeping the fluence of the first implant of Co as constant (2×10^{17} ions/cm^2). The simulation results showed that initially, Co has the highest concentration in Si. With an increase in Fe ion fluence, Co concentration at the surface starts to

decrease. For a fluence of 7.5×10^{16} ions/cm^2, both Fe and Co have similar concentrations at the surface. This happens because around a fluence 7.5×10^{16} ions/cm^2, both Fe and Co have the same sputtering yield which implies that an equal amount of Fe and Co are sputtered from the surface until both ions have equal concentration.

The concentration of each ion at this fluence was found to be ~23%. With a further increase in Fe ion fluence, the cobalt concentration decreased and reached its minimum concentration for the Fe fluence of 2×10^{17} ions/cm^2. This happens because most of the Co present in Si are sputtered away by the incoming Fe ions since their atomic masses are very close to each other. This implicates that even if more than one ion of similar mass is implanted in Si, it is difficult to implant more ions beyond the saturation fluence and saturation concentration for particular energy of incoming ions. In this case, the simulated saturation fluence for 55 keV Fe and/or Co implanted in Si was found to be 2×10^{17} ions/cm^2. The saturation concentration was estimated to be 48%. The simulated results in Figure 4.9 provide an excellent recipe to synthesize ternary Fe-Co-Si alloys with the desired stoichiometric ratio as a function of depth.

4.3   Conclusion

It is essential to choose the appropriate simulation code for modeling the distribution of ions in solids as the elemental concentration depth profile of the implanted ions differs considerably by considering a static or dynamic simulation code. As ion implantation is a dynamic process, it is difficult to estimate the distribution of ions only using the most popular TRIM code. SDTrimSP code can provide more realistic results which are comparable to the experimental data. Our simulations indicate that for a specific condition (energy and angle of incidence) of implantation, there exists a saturation fluence that provides the maximum concentration of heavy ions that can be implanted into a lighter atom target, beyond which the concentration of implanted

ion does not increase further. We have shown that the sputtering yield increases with an increase in ion incidence angle and ion fluence. But the directions in which the atoms are sputtered to the target surface normal do not seem to change. Most of the atoms were sputtered in the forward direction between 30°- 60° with a peak around 45°. The sputtering and distribution of ions are greatly affected by the surface composition of the target material. For the ion irradiation in the Consideration of a dynamic target is essential when the implantation is performed for a higher fluence using an ion beam because the target composition changes significantly which affects the movement of the ions in the target. This results in a change of the implantation profiles. Thus, these ion-solid interaction simulations can be used to generate implantation parameters input parameters of the desired implant distribution which can save the time and effort of performing multiple experiments.

CHAPTER 5

OBSERVATION OF ROOM TEMPERATURE SUPERPARAMAGNETIC BEHAVIOR OF

Fe_5Si_3 NANOCRYSTALS SYNTHESIZED VIA 50 KEV Fe ION IMPLANTATION IN

SILICON*

5.1   Introduction

In this study, we report the formation of crystalline Fe_5Si_3 structures embedded inside Si

substrate, synthesized via low energy (50 keV) Fe^- ion implantation and subsequent thermal

annealing. Before the experiment, the implantation process (depth, distribution, and sputtering of

the implanted and target atoms) was modeled using both static and dynamic ion solid interaction

codes to achieve the desired implantation parameters. The simulation showed that for a 50 keV Fe

ion beam, a fluence of 2×10^{17} ions/cm^2 gives the optimal concentration of Fe and Si in the

substrate for the desired Fe-rich stoichiometry. X-ray photoelectron spectroscopy (XPS) spectra

show the presence of Fe ions buried under the surface of Si and XRD analysis confirms the

presence of crystalline Fe_5Si_3 in Si. In a vibrating sample magnetometer (VSM) analysis, the

synthesized Fe_5Si_3 nanocrystals show superparamagnetic behavior with very low but nonzero

magnetization at room temperature.

5.2   Experimental Details

The Fe_5Si_3 nanostructured crystals were synthesized using 50 keV Fe^- ion implantation into

n-type Si (100) wafers with a fluence of 2×10^{17} ions/cm^2 using the low energy ion implantation

system available at the IBMAL of the UNT [42]. Before the implantation, the Si wafer was cleaned

in acetone to remove any surface contaminations. To exclude the role of native oxide, another set of samples were implanted with the same implantation conditions, after etching the surface oxide using diluted HF solution for 5 minutes. The SNICS-II ion source was used to produce and accelerate the Fe^- ions from a solid cathode containing a mixture of Fe and Ag powder. The beam was electrostatically raster-scanned over a circular aperture of radius 1 cm to ensure homogeneous implantation on the target material. To avoid ion channeling effects, the normal to the sample stage was oriented at an angle of 7° to the incident ion beam. The raster beam current density was kept at ~ 2 $\mu A/cm^2$ during the implantation while the target substrate was mounted on a stage at room temperature. The implantation chamber was kept under a high vacuum with a pressure of 9×10^{-8} mbar. After the implantation, the samples were annealed at 500 °C for 60 minutes in a vacuum environment. The annealing was carried out by mounting the sample on a molybdenum plate with a resistive heating arrangement attached to a five-axis goniometer. The vacuum inside the annealing chamber was maintained at 1×10^{-7} mbar throughout the thermal annealing process. The XRD and XPS measurements were performed at the Material Research Facility of UNT, while the VSM measurements were performed at UNT's Advanced Materials and Manufacturing Processes Institute (AMMPI). The XRD measurements were performed using Cu K_α 1.541 Å radiation with a Rigaku Ultima III high-resolution XRD. The XRD patterns were obtained using two-theta scans from 20° to 90°. The angle of incidence of X-Rays to the sample surface was fixed at 0.5°. The XPS depth profiling measurements were performed with a PHI 5000 Versaprobe. Al monochromatic X-ray radiation (1486.7 eV) was focused on a spot size of about 200 μm. The sputtering was performed with a 2 keV Ar beam on a 2×2 mm^2 area. The pressure of the target chamber was kept at 9×10^{-9} mbar during the XPS measurement. The magnetic properties of the samples were measured using the VSM option in DynaCool-14 Physical Properties Measurement

System (PPMS) from Quantum Design Inc. The samples were fixed on a quartz holder to minimize any external demagnetization effect. The sample surface was kept parallel to the applied magnetic field.

5.3   Simulation Details

Theoretical ion solid interaction simulations were carried out before the ion implantation process to estimate the optimal ion energy and fluence for which the implanted concentration of Fe maximizes in Si at a certain depth. The initial simulation of the implantation process was carried out using a well-known ion solid interaction code TRIM [79] simulation package. The simulation was carried out for 5×10^5 ions. TRIM simulation gives the output in terms of $(atoms/cm^3)/(atoms/cm^2)$. The output result was then multiplied with the ion fluence of 2×10^{17} ions/cm^2 to get the implanted concentration in terms of atoms/cm^3. Although the TRIM code can predict the distribution of the implanted ions in the substrate, it does not incorporate directly the dynamic modification of the target composition during the irradiation process.

Table 5.1: The simulation parameters for the 50 keV Fe ion implantation in Si.

Fe ion energy	50 keV
Fluence	2×10^{17} ions/cm^2
Angle of implantation	7 °
Interaction potential	Ziegler-Biersack-Littmark (ZBL) [80]
No of particles for simulation	50000
Integration method	MAGIC algorithm from Biersack [81]

5.4   Results from Ion Solid Interaction Simulation

When an energetic ion travels through solids, it loses energy via two nearly independent processes: (i) collision with target nuclei called "nuclear energy loss", and (ii) collision with target electrons called "electronic energy loss". When an ion travels in an energy range with dominant nuclear energy loss, it can result in knocking off the target atoms, particularly sputtering of the

atoms on the surface of the target [79]. This sputtering of the target surface by the irradiated species plays an important role in accurately determining the implant atom depth profile. In general, the sputtering effect is not significant in the case of high-energy (MeV) implantation, but it plays an important role in the case of low-energy (keV) implantation with heavy ions on a target with lighter atoms.

Figure 5.1: Simulation results of 50 keV Fe ion implanted in Si using the static code TRIM and the dynamic code SDTrimSP. (a) Electronic vs Nuclear energy loss of Fe implanted in Si using TRIM at 1 - 600 keV energy, (b) Sputtering depth of Si as a function of various ion fluence simulated using SDTrimSP.

Figure 5.1 (a) shows the simulated energy loss of Fe in Si for various incident ion energy. It is clear that for around 500 keV of Fe, the electronic energy loss starts dominating over electronic energy loss. The peak nuclear energy loss for Fe occurs around 50 keV dominating the electronic energy loss. For the 50 keV Fe ion in Si, the electronic energy loss is about ~15 eV/A° whereas nuclear energy loss is about ~ 91 eV/A°. In this case, the nuclear energy loss is roughly 6 times the electronic energy loss. In the range of 500 keV energy, the electronic energy loss dominates and contributes to the ionization of the target atoms. The dominance of nuclear energy loss over electronic energy loss is responsible for the sputtering of the Si target. At 50 keV implant energy, the depth of the surface erosion increases with fluence linearly, which can be seen in Figure 5.1(b). In this case, ~ 68 nm of Si surface was sputtered by the incoming Fe ions. The partial sputtering

yield of Fe (Figure 5.2(a)) increases with an increase in ion fluence and reaches a saturation value around a fluence of 1.8×10^{17} ions/cm^2.
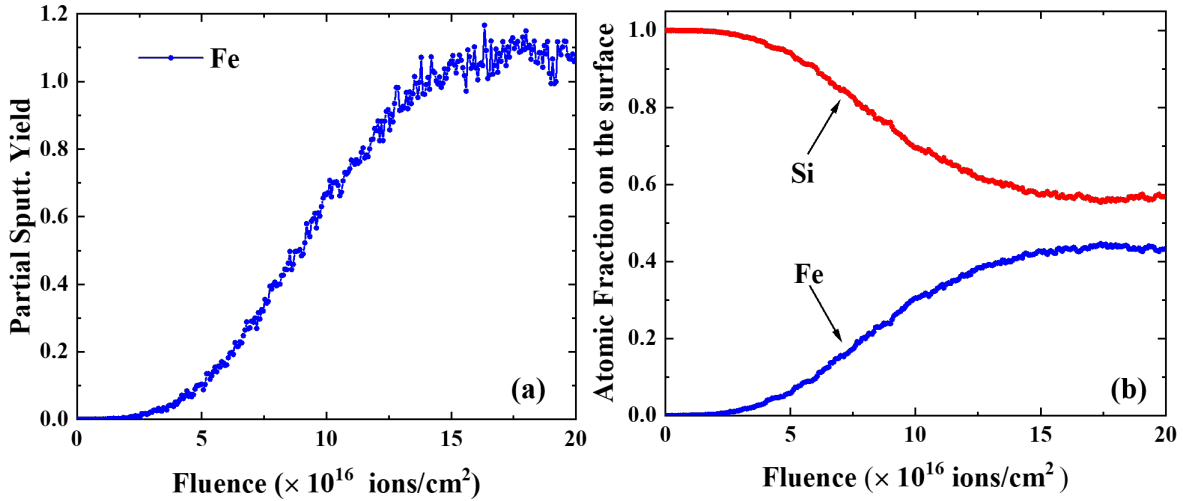
Figure 5.2: Simulation results of 50 keV Fe ion implanted in Si using the dynamic code SDTrimSP. (a) Partial sputtering yield of 50 keV Fe in Si as a function of ion fluence, and (b) Atomic fraction of Fe and Si at the surface as a function of ion fluence.
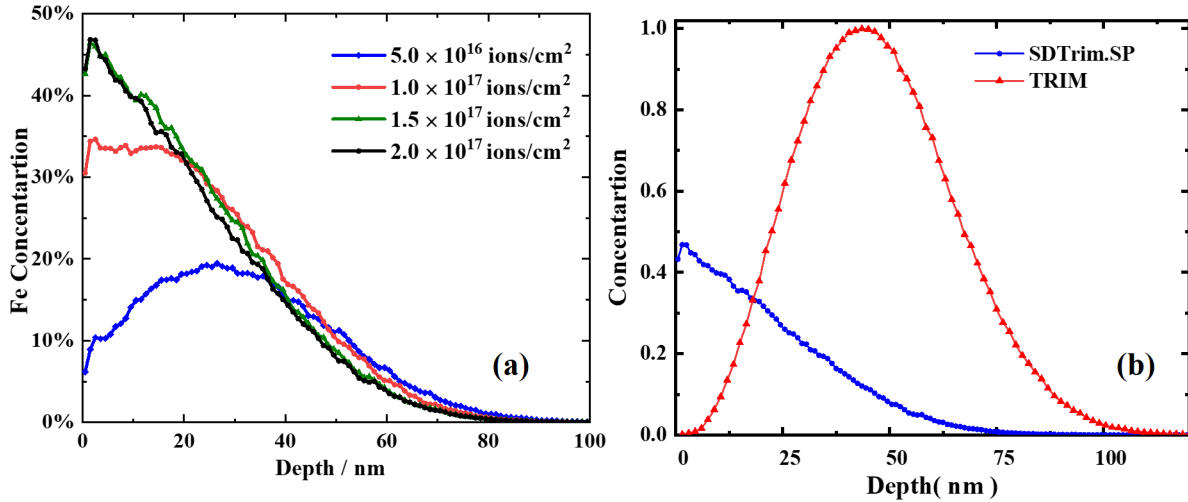
Figure 5.3: (a) Concentration of Fe as a function of depth for various ion fluences simulated using dynamic SDTrimSP code, (b) Depth profile of Fe implanted at 50 keV in Si for a fluence of 2×10^{17} ions/cm^2 simulated using both static code-SRIM and SDTrimSP.

The SDTrimSP simulated depth profile of implanted ions for a 50 keV Fe at various fluences is shown in Figure 5.3(a). The Fe concentration in Si increases to a maximum of ~48% for a fluence of 2×10^{17} ions/cm^2. In the simulation (Figure 5.3(a)), the concentration of Fe is seen to be saturated at a fluence range of $1.5 - 2 \times 10^{17}$ ions/cm^2. A comparison of depth profile

simulated using SDTrimSP and the static code TRIM is also shown in Figure 5.3(b). The TRIM simulation showed that for a 50 keV beam of Fe with a fluence of 2×10^{17} ions/cm^2, the range of the implanted ions is peaked at 45 nm with a full width at half maximum (FWHM) value of 22.5 nm. The distribution of the implanted ions in Si has spread over a depth of ~100 nm. It is important to note that with the change in the fluence, the depth profile of the implanted sample and the surface profile of the target change greatly due to the dynamic process.

5.5   Results from XPS Analysis

The depth profiles of the 50 keV Fe implanted Si samples were experimentally studied using XPS along with Ar ion etching. Figure 5.4 shows the XPS spectra from the surface of the as implanted and un-irradiated samples.
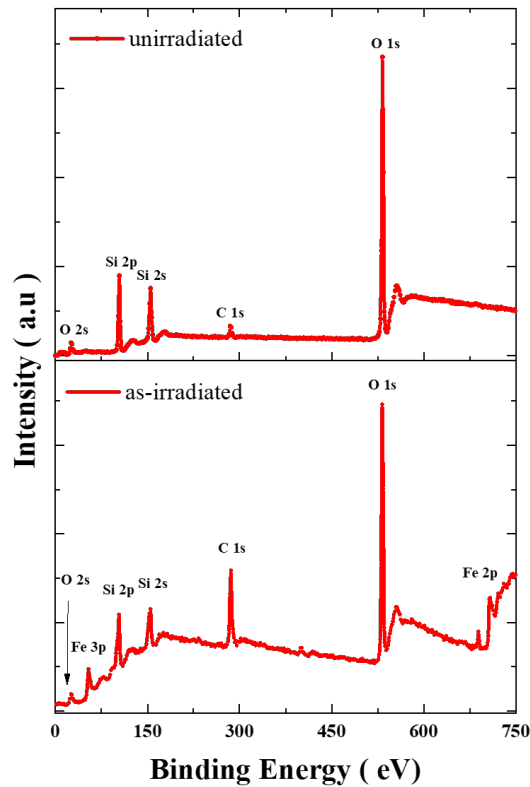
Figure 5.4: XPS Spectra collected at the surface of un-irradiated (virgin) Si and Si sample as-irradiated with 50 keV Fe at a fluence of 2×10^{17} ions/cm^2.
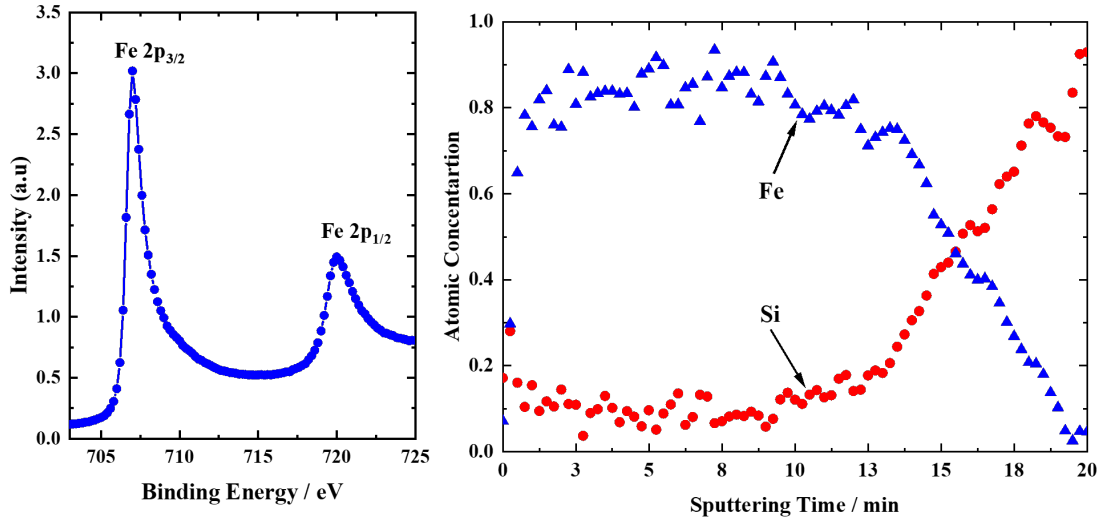
Figure 5.5: XPS depth profile of Fe implanted in Si at 50 keV for a fluence of 2×10^{17} ions/cm^2 as a function of sputtering time (right); XPS measurement of Fe 2p Peak (left).

The spectrum shows the presence of C and O on the surface. The presence of C on the surface of the sample is due to the long implantation process. The target irradiation chamber is evacuated by a Turbopump backed by an oil-free scroll pump. However, the presence of a small amount of carbon on the sample surface is mainly due to the generation of carbon atoms during the interaction of energetic ions with some of the components of beamlines. Recent research by Was et al. and Wang et al. have discussed the various sources of carbon contamination during ion implantation in great detail [82,83]. In future experiments, we plan to install a liquid nitrogen-based cold finger near the target stage to trap the carbon atoms. The O signal is due to the growth of native oxide on the silicon sample surface due to transferring the sample outside the vacuum environment. The sample was placed under vacuum only during the implantation and analytical characterization with XPS only. The native oxide is found to present only on the surface with 1-2 nm thickness. The carbon surface contaminants for high fluence implantation are up to a few nanometers of the surface [84]. To study the depth profile of Fe and Si, ~7 nm of the sample surface was sputtered using a 2 keV Ar$^+$ beam to remove the contaminant film prior to the collection of

depth profile data. The XPS depth profile is shown in Figure 5.5. Figure 5.6 shows the XPS spectra of Fe 2p as a function of sputtering time. The decrease in the intensity of the Fe 2p Signal confirms the decrease in Fe concentration as the sputtering time increases.
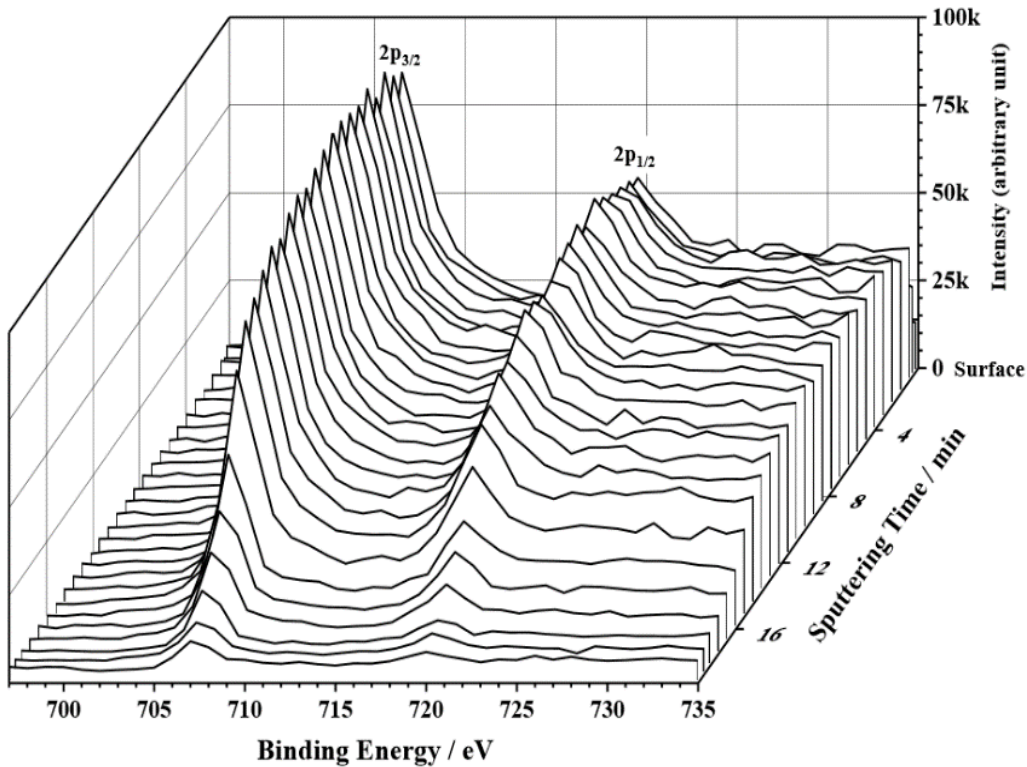
Figure 5.6: XPS Spectra of as implanted sample showing the depth profile of Fe 2p as a function of sputtering time.

5.6   Results from XRD Analysis

The structural properties of ion-irradiated samples were studied using the XRD analysis. Figure 5.7 shows the XRD pattern of the (a) annealed sample along with (b) as-implanted, and (c) un-irradiated virgin sample. In the case of the annealed sample, five distinct peaks are visible. Out of those five peaks, three are dominant and are identified as Fe_5Si_3 crystals. The peaks were identified utilizing Crystallography Open Database - 9015765. In the case of Fe_5Si_3, the highest intensity of the XRD pattern occurs for (111) and (131) crystal planes. Un-annealed, as-irradiated Si shows weak crystalline peaks of both Fe_5Si_3 and Si (400).

61
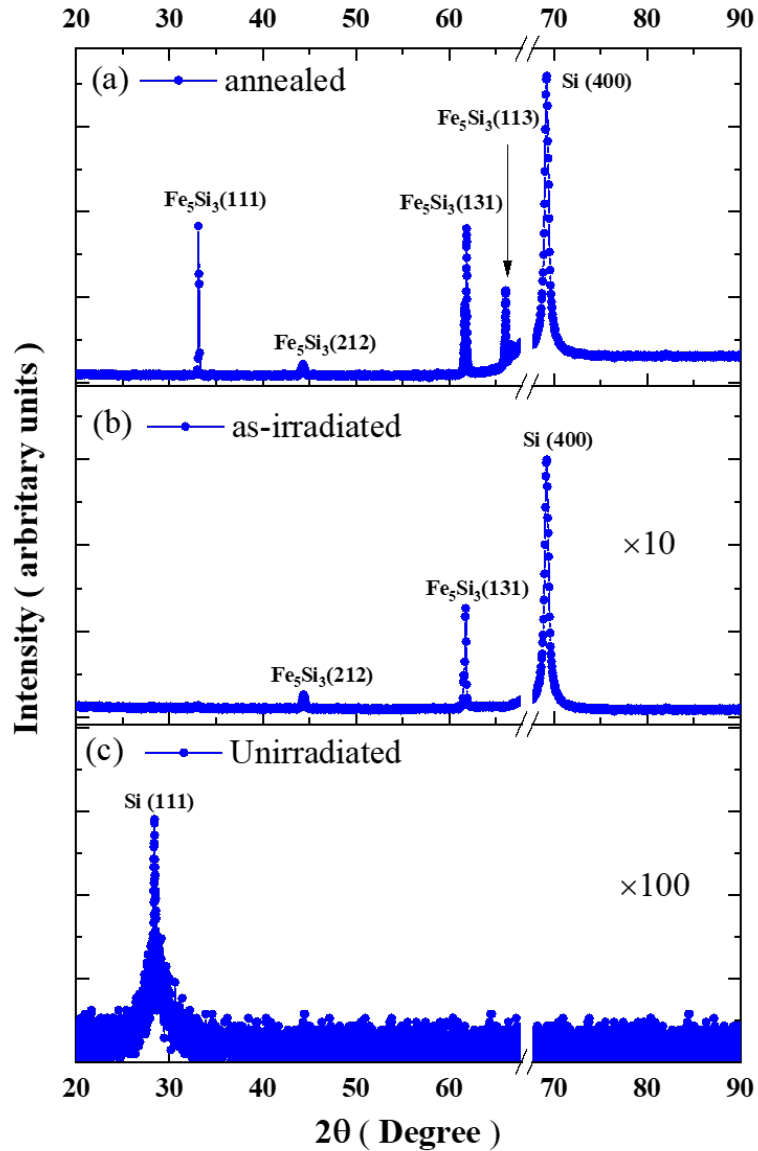
Figure 5.7: XRD Pattern of (a) Si irradiated with 50 keV Fe at a fluence of 2×10^{17} ions/cm^2 and annealed at 500 °C in vacuum for 1-hour (b) as-irradiated Si (c) non-irradiated virgin silicon. The intensity of (b) and (c) are multiplied by 10 and 100 respectively.

The appearance of weak crystalline peaks in the as-irradiated samples is due to the ion-beam mixing as well as the local beam heating effect during the implantation. , the beam flux was kept at a moderate value of 2.2 μA/cm^2. However, it may make a minor contribution to the local heating of the samples. Better crystalline peaks are observed in the 500 °C for 60 minutes annealed sample is due to the growth of Fe$_5$Si$_3$ crystals in Si. When a transition metal is implanted into Si,

it becomes interstitial and diffuses quicker into Si lattice when given enough thermal energy. In this case, a high concentration of Fe is observed near the surface region of the Si substrate. As described in the introduction (Chapter -1), previous research shows that iron-rich phases are preferentially formed when the implanted substrate is annealed at a temperature up to 500 ºC [39]. In the present study, the post-implantation annealing of the sample was performed at a narrow window of 500 ± 5 ºC for 1 hour providing the necessary energy to facilitate the growth of iron-rich polycrystalline Fe_5Si_3 structures in the Si substrate.

The grain size of Fe_5Si_3 crystals has been estimated from the FWHM value of the peaks in the XRD pattern using the Scherrer formula [85]. The Scherrer Formula is given as,

From the Scherrer Formula, the average grain sizes of the synthesized Fe_5Si_3 crystal have been determined in the range of 38 nm to 70 nm.

$$D = \frac{K\lambda}{\beta Cos\theta}$$

where

> D = average grain size
> λ = wavelength of x-ray
> β = FWHM
> θ = diffraction angle corresponding to the FWHM

5.7   Results from Magnetic Measurement

The magnetic properties of the synthesized Fe_5Si_3 crystals were investigated by measuring the response of the samples to an applied magnetic field both at 5 K and 300 K temperatures. Figure 5.8 shows the M-H curve of the synthesized crystals at 5 K whereas Figure 5.9 represents the behavior at 300 K. The hysteresis loop of the annealed sample at 300 K shows that the coercivity of the synthesized structure is ~ 25 Oe which is typical in the case of a

superparamagnetic system. The saturation magnetization of the as-irradiated sample decreased from ~75 emu/g to ~27 emu/g with an increase in the substrate temperature from 5 K to 300 K. With the annealing of the irradiated substrate at 500 °C for 1 hour, better crystalline structures are formed which increased saturation magnetization. Annealed samples show a higher saturation of 185 emu/g compared to as-irradiated ones at 5 K. With an increase in substrate temperature, this saturation magnetization decreases to ~110 emu/g at 300 K for the annealed sample. For both as-irradiated and annealed samples, the saturation magnetization decreased with an increase in substrate temperature from 5 K to 300 K.
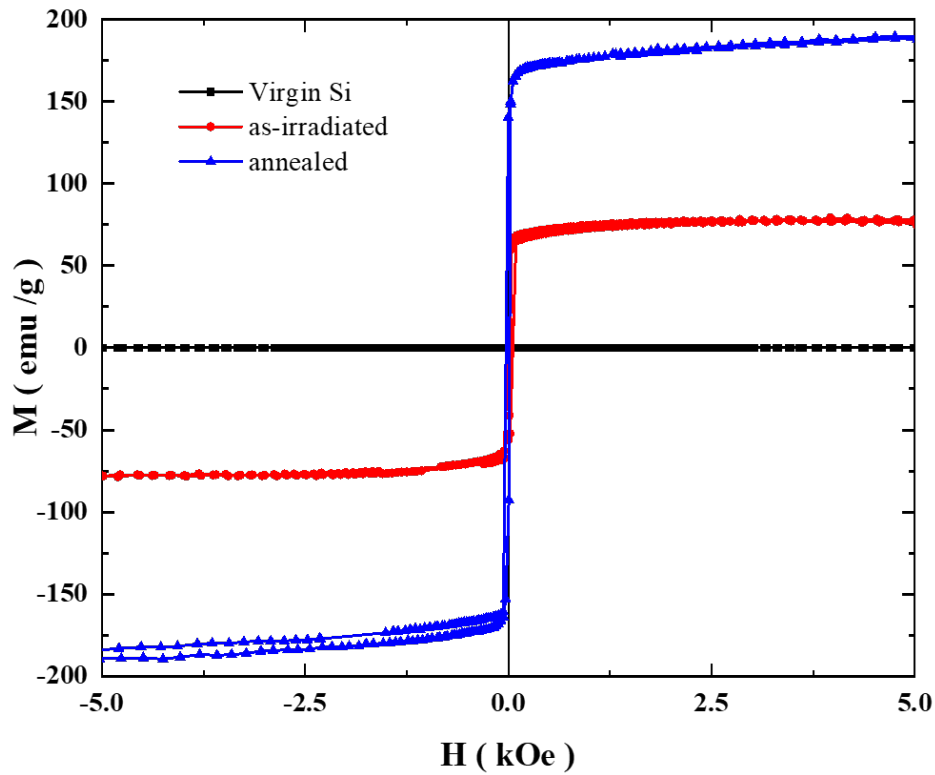
Figure 5.8: Hysteresis loop (M vs H) of virgin Si, as-irradiated and annealed Si sample irradiated with presence of Fe₅Si₃ structures measured at 5 K.
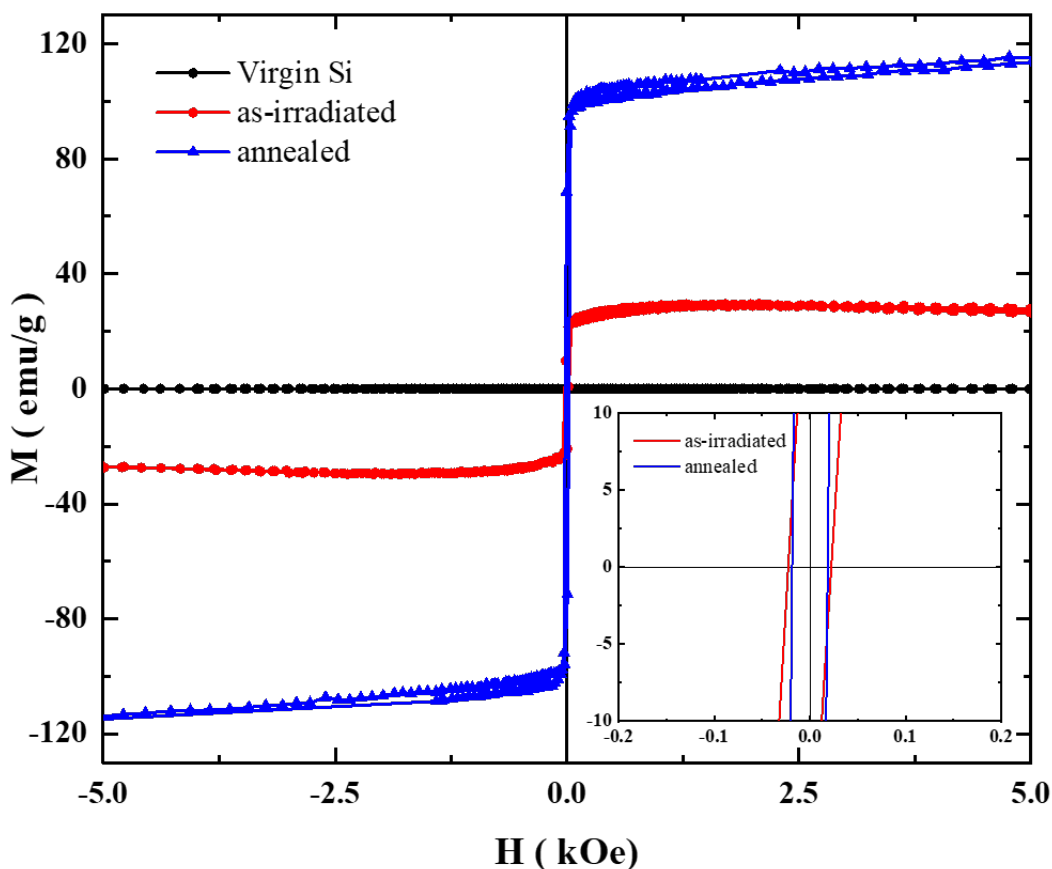
Figure 5.9: Hysteresis loop (M vs H) of Virgin Si, as irradiated and annealed Si with Fe₅Si₃ structures measured at 300 K. The inset shows the M-H loops in a larger scale with same axis and units.

The magnetic behavior of these nanocrystals is expected to be superparamagnetic. The superparamagnetic behavior of nanoparticles was first proposed by Frenkel and Doefman in 1930 [40]. When the dimension of a ferromagnetic nanoparticle is in the range of 10 nm - 100 nm, it shows superparamagnetic behavior [41]. In the present studies, the nanocrystals have sizes ranging from 38 nm to 70 nm with an average size of 68 nm. With a reduction in grain size, these ferromagnetic nanocrystals change from a multi-domain system to a single domain system which results in a superparamagnetic behavior. Such type of magnetic behavior of the synthesized structures is useful for biomedical applications as these superparamagnetic iron-rich silicide nanoparticles can be inserted into polymer particles and can be made biocompatible.

5.8   Conclusion

We have demonstrated the synthesis of Fe_5Si_3 nanocrystals embedded in Si using 50 keV Fe^- implantation at a fluence of 2×10^{17} ions/cm^2 and post-thermal vacuum annealing at 500 ºC for one hour. The structural characterization using the XRD pattern of the sample shows the presence of 38 nm to 70 nm long-grain nanocrystals embedded in Si. The XPS depth profile confirmed the presence of a high concentration of iron near the surface region of the irradiated Si as predicted by the SDTrimSP simulation. The magnetic characterization of the sample shows that the synthesized nanocrystals are expected to be superparamagnetic with a very small coercive field. The superparamagnetic behavior is present even at room temperature.

CHAPTER 6

OBSERVATION OF SUPERPARAMAGNETIC BEHAVIOR AT ROOM TEMPERATURE IN

ION BEAM SYNTHESIZED Co-Si NANO SYSTEM

6.1   Introduction

In this study, we report the observation of superparamagnetic behavior in Co-Si nanostructures embedded inside Si substrate, synthesized via 50 keV Co$^-$ ion implantation. Before the experiment, the implantation process (depth, distribution, and sputtering of the implanted and target atoms) was modeled using both static and dynamic ion solid interaction codes to achieve the desired implantation parameters. The simulation indicated that for a 50 keV Co ion beam, a fluence of 3.2×10^{16} ions/cm^2 would provide the optimal balance between the concentration of Co and sputtering of Si in the substrate for the desired Co-Si stoichiometry. The characterization using RBS indicate the presence of Co ions buried under the surface of Si and XRD analysis confirms the presence of crystalline Co-Si structures in Si. The RBS depth-profile of the Co ions in Si were compared with the dynamical simulated depth profiles.   The VSM analysis indicate, the synthesized Co-Si nanostructures show superparamagnetic behavior with very low magnetization at room temperature and higher blocking temperature.

6.2   Simulation Details

Theoretical ion solid interaction simulations were carried out before the ion implantation process to estimate the optimal ion energy and fluence for the implantation process. The initial simulation of the implantation process was carried out using a well-known ion solid interaction code TRIM [79] simulation package. TRIM simulation gives the output in terms of (atoms/cm^3)/(atoms/cm^2). The output result was then multiplied with the ion fluence of 3.2×10^{16} ions/cm^2 to get the implanted concentration in terms of atoms/cm^3. Although the TRIM code can

predict the distribution of the implanted ions in the substrate, it does not incorporate directly the dynamic modification of the target composition during the irradiation process. To further study the distribution of cobalt ions in silicon, we have used SDTrimSP [86] simulation code which includes the modification of the target surface during the implantation process due to the sputtering effect. The SDTrimSP allows the target surface to change as a function of the implanted fluence. This allows the surface sputtering of the implanted target to be included in all subsequent histories, thus allowing for far greater accuracy in the low energy, high fluence heavy ion implantation process. The elemental depth profile results from both the static and dynamic simulations were normalized to the fluence of 3.2×10^{16} ions/cm^2. For both simulations, the input parameters were kept identical to ensure the consistent output of the simulation results. The details of the simulation parameters used in this study are given below.

Table 6.1: Parameter for the Monte-Carlo simulation.

Co ion energy	50 keV
Fluence	3.2×10^{16} ions/cm^2
Angle of implantation	7 $^\circ$
Interaction potential	Ziegler-Biersack-Littmark (ZBL)[80]
Integration method	MAGIC algorithm from Biersack [81]
The thickness of Sputtered Layer	~ 8 nm

6.3   Experimental Details

The implantation was carried out using 50 keV Co$^-$ ion into n-type Si (100) wafers with a fluence of 3.2×10^{16} ions/cm^2 using the low energy ion implantation system available at the IBMAL of the UNT [42]. Before the implantation, the Si wafer was cleaned in acetone to remove any surface contaminations. The SNICS-II ion source was used to produce and accelerate the Co$^-$ ions from a solid cathode. The cathode was made from aluminum with a small cylindrical cavity in which cobalt powder was tightly packed. The cathode was kept under a constant cooling cycle

during the implantation to ensure the efficient production of Co⁻ ions from the source. The ions produced were then accelerated through a series of potential differences to increase the energy of ions to 50 keV. The ion beam was focused on using the Einzel lens to minimize the loss in beam current during the transmission of ions from the source to the target. The Co ions were filtered from the beam with a momentum per charge selector magnet which was has a resolution of 1 amu. The beam was electrostatically raster-scanned over a circular aperture of radius 1 cm to ensure homogeneous implantation on the target material. To avoid ion channeling effects, the normal to the sample stage was oriented at an angle of 7° to the incident ion beam. The raster beam current density was kept at ~ 2 $\mu A/cm^2$ during the implantation while the target substrate was mounted on a stage at room temperature. The implantation chamber was kept under a high vacuum with a pressure of 7.5×10^{-8} mbar. The VSM measurements were performed at the UNT's AMMPI. The magnetic properties of the samples were measured using the VSM option in DynaCool-14 Physical Properties Measurement System (PPMS) from Quantum Design Inc. The samples were fixed on a quartz holder to minimize any external demagnetization effect. The sample surface was kept parallel to the applied magnetic field. RBS experiments were performed using a 1 MeV He⁺ beam from a single-ended accelerator (NEC, 9SH). The RBS detector was placed at a scattering angle of 150 ° and the angle of beam incidence to the sample surface normal was fixed at 7°. The RBS spectra were analyzed with the SIMNRA computer package . Corresponding depth profiles were extracted from the RBS spectra.

6.4   Results and Discussion

For this research, the energy of the implanted cobalt ion was chosen based on the energy loss of the ion to the target atoms. When an energetic ion travels through solids, it loses energy via two nearly independent processes: (i) collision with target nuclei called "nuclear energy loss", and

(ii) collision with target electrons called "electronic energy loss". When an ion travels in an energy range with dominant nuclear energy loss, it can result in knocking off the target atoms, particularly sputtering of the atoms on the surface of the target [79]. This sputtering of the target surface by the irradiated species plays an important role in accurately determining the implant atom depth profile. In general, the sputtering effect is not significant in the case of high-energy (MeV) implantation, but it plays an important role in the case of low-energy (keV) implantation with heavy ions on a target with lighter atoms. Figure 6.1 shows the simulated energy loss of Co in Si for various incident ion energy. It is clear that for around 620 keV of Co, the electronic energy loss starts dominating over electronic energy loss.
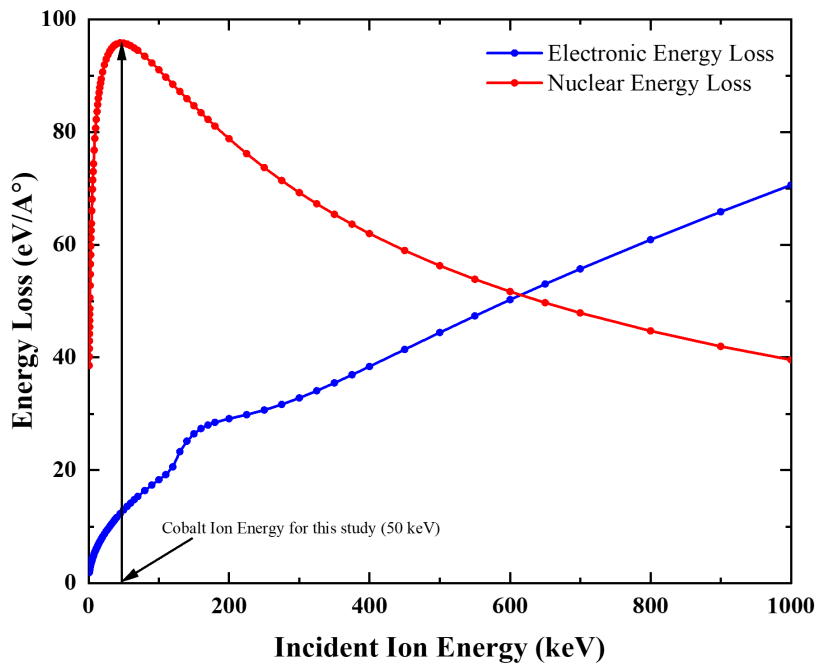
Figure 6.1: Electronic vs nuclear energy loss of cobalt in silicon for various incident ion energy.

For incoming ion energy of less than 620 keV, Nuclear energy loss is most dominant. The peak nuclear energy loss for Co occurs around 50 keV dominating the electronic energy loss. For the 50 keV Co ion in Si, the electronic energy loss is about ~12 eV/A° whereas nuclear energy loss is about ~ 96 eV/A°. In this case, the nuclear energy loss is about 8 times the electronic energy

loss. The dominance of nuclear energy loss over electronic energy loss is responsible for the sputtering of the Si target and this sputtering affects the distribution of implanted ions in the target. This sputtering increases with an increase in ion fluence for fixed incoming ion energy. At 50 keV implant energy and for a fluence of 3.2×10^{16} ions/cm^2 the total sputtering was ~8 nm. This sputtering mainly removes the surface oxide from silicon and does not affect the depth profile of implanted ions. To create metal nanostructures buried in near-surface region implantations at keV energy are performed.

The SRIM and SDTrimSP simulated depth profile of implanted ions for a 50 keV Co at various fluences is shown in Figure 6.2. The Co concentration in Si increases to a maximum of ~12% for a fluence of 3.2×10^{16} ions/cm^2. The TRIM simulation showed that for a 50 keV beam of Co with a fluence of 3.2×10^{16} ions/cm^2, the range of the implanted ions is peaked at 40 nm whereas, in the case of SDTrimSP, it's 35 nm. The simulation showed that the implanted Co ions are distributed over a depth of ~100 nm. It is important to note that with the change in the fluence, the depth profile of the implanted sample and the surface profile of the target change greatly due to the dynamic process.
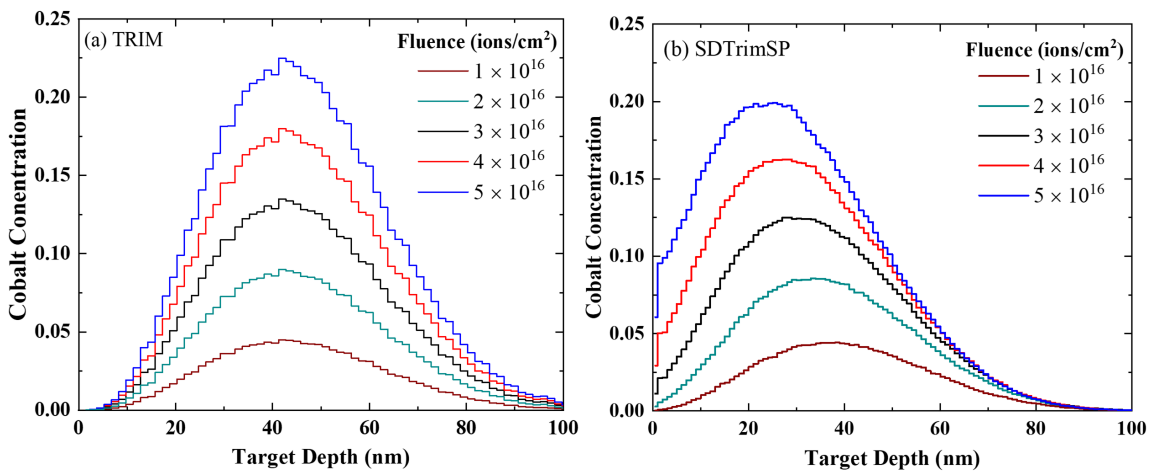
Figure 6.2: The simulated results for a 50 keV Co beam implanted into a Si substrate for various fluence using a) SRIM, and b) SDTrimSP.

The RBS spectrum of the Co irradiated sample is shown in Figure 6.3. The RBS spectrum shows a clear cobalt peak which is spread over a depth of ~100 nm. The spectrum also shows a small oxygen peak which is typical surface oxide in the case of silicon that occurs due to handling of the sample outside the vacuum environment. The corresponding depth profile extracted from the RBS spectra is shown in Figure 6.4. The depth profile was extracted using the SIMNRA simulation package. For the SIMNRA simulation, the Co–Si layer was subdivided into several layers each with a thickness of 5nm. Then each 5 nm layer was configured with a different Co to Si ratio to match the experimental RBS Spectrum. The results from the RBS analysis indicate the formation of a buried Co–Si layer.
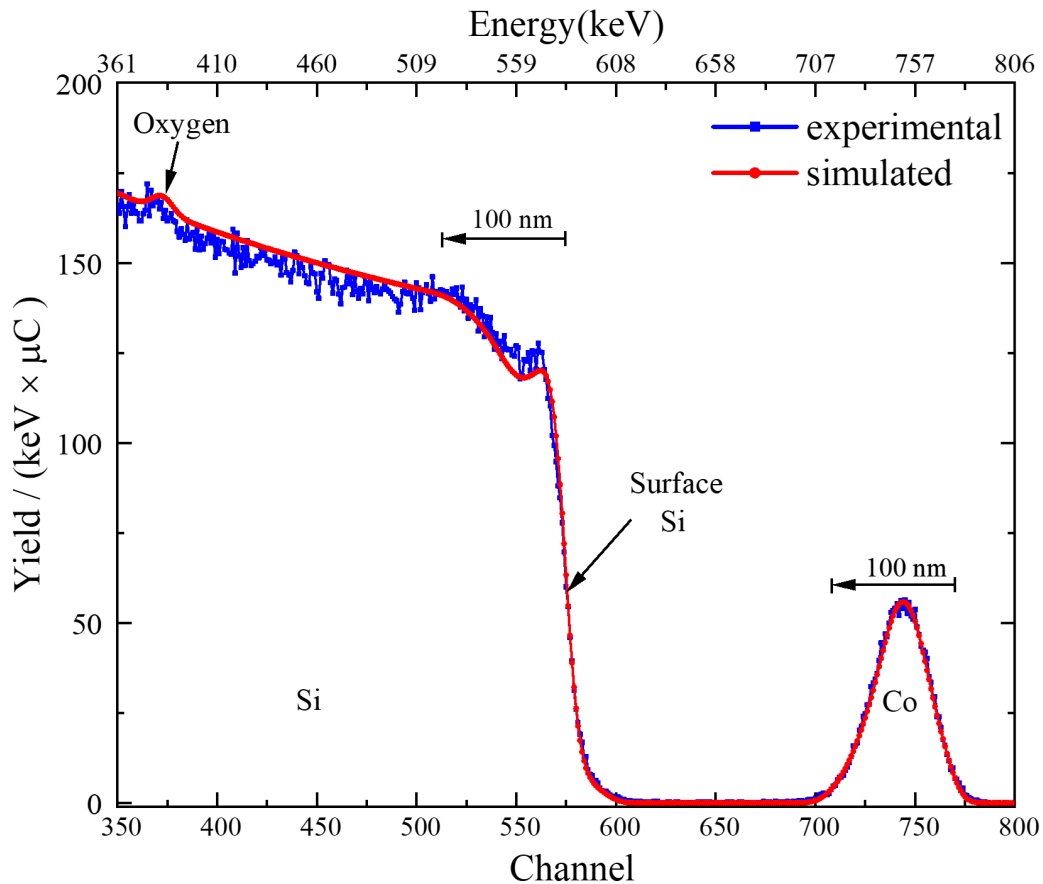
Figure 6.3: SIMNRA fit of a typical RBS spectrum obtained from a 50 keV cobalt implanted into silicon sample.

Figure 6.4 shows the overlap of both experimental and simulated depth profiles for 50 keV Co in Si. Both SRIM and SDTrimSP simulated depth profile matches with the experimental depth profile. However, SDTrimSP matches more closely to the experimental ion distribution. The experimental distribution shows that the peak concentration of implanted ion is around ~14% and it peaks around 40 nm.
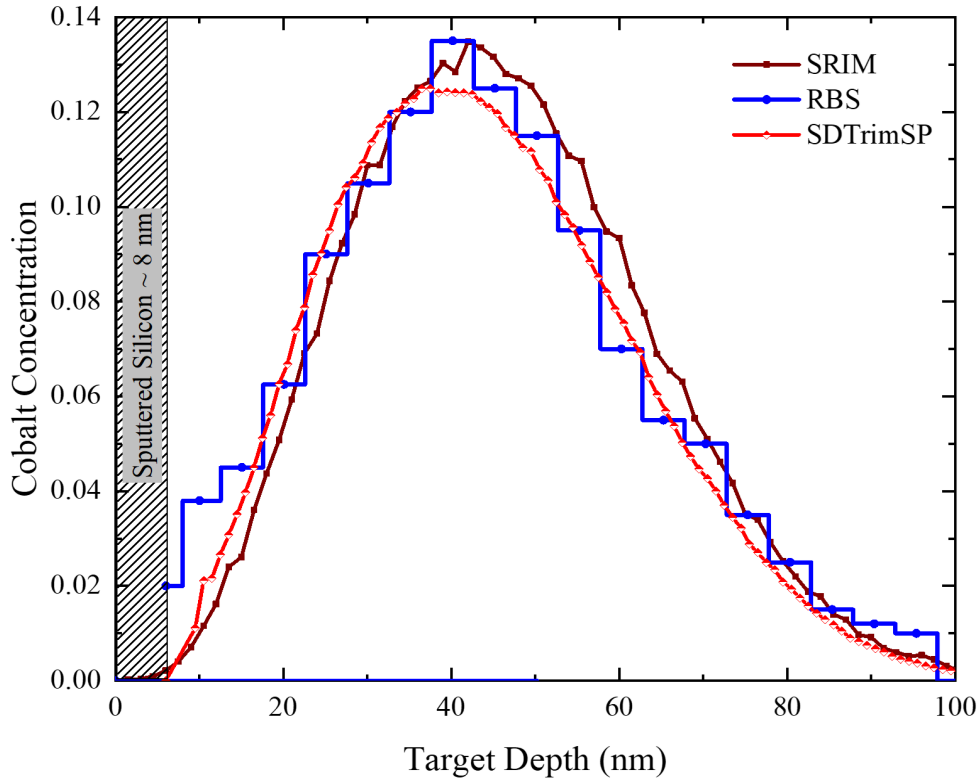
Figure 6.4: Depth profiles of cobalt in Si using RBS analysis and simulated profiles from SRIM and SDTrimSP codes.

The magnetic behavior of the as-irradiated Co-Si was measured by the temperature-dependence magnetization and hysteresis loop. The temperature dependence magnetization of the sample was carried out by varying the temperature between 5 K and 400 K and an external magnetic field of 100 Oe. Typical temperature-dependence magnetization curves are consisting of zero-field cooled and field-cooled (FC) curves as shown in Figure 6.5. For the zero-field-cooled measurement (ZFC), the sample was cooled to 5 K in the absence of an external magnetic field. A

field of 100 Oe was then applied and simultaneously the magnetization was measured with increasing temperature. For the field-cooled measurement, the sample was cooled to 5 K in the presence of a field of 100 Oe, and then the magnetization was measured with increasing temperature in the same field.
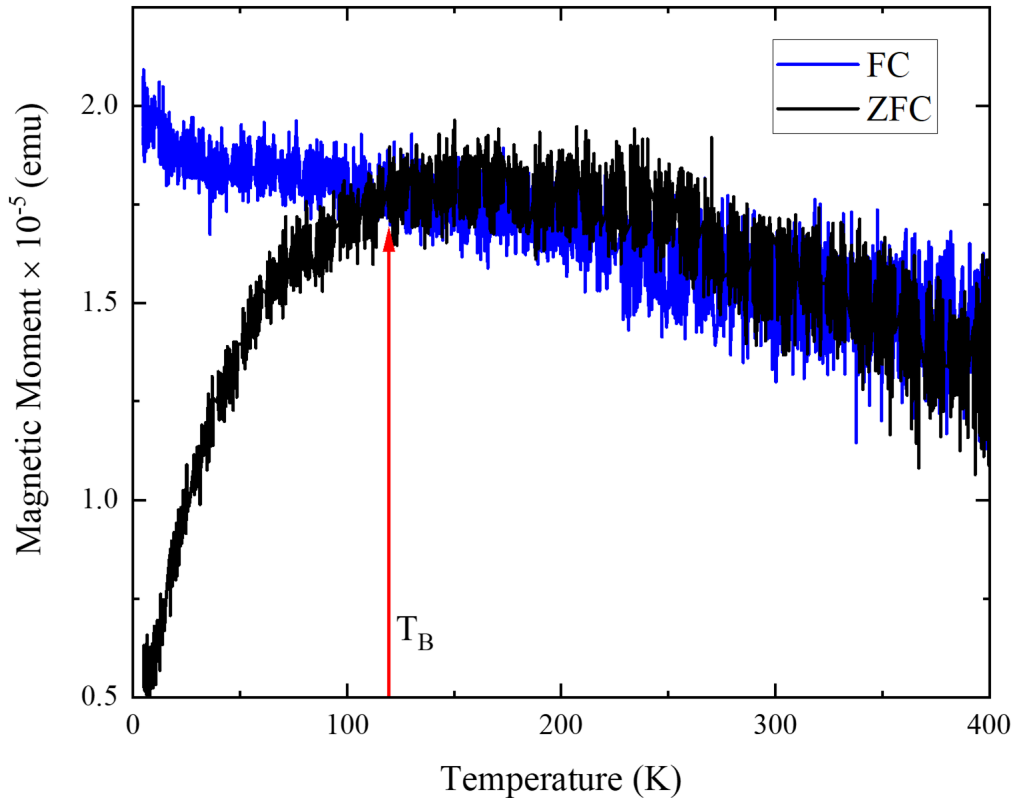
Figure 6.5: M Vs T of a sample with 50 keV Co implanted into Si. The arrow in red point towards the blocking temperature of this system.

When the nanoparticles are cooled to extremely low temperatures in the presence of a magnetic field (Field Cooled process), each particle is magnetized in the direction of the applied field which results in a net increase in the total magnetization. In the case of no applied field also known as zero-field cooling, the net magnetization is relatively smaller compared to the field cooling one. This can be seen in Figure 6.5. Both the FC and ZFC curves bifurcate at a certain temperature which indicates that there exists an equilibrium magnetization below the separation temperature. This temperature is also known as blocking temperature (T_b). Below T_b, the sample

stays in the ferromagnetic state. This is the characteristic feature of superparamagnetic behavior. In this case, the observed blocking temperature was found to be ~120 K. This blocking temperature depends on the concentration of the Co ions in Si and also dependent on the size of the nanoclusters formed in Si.

It has also been shown in various research that nanoparticles can overcome magnetic anisotropy as they can get thermally activated very easily. Beyond the blocking temperature, the nanoparticles lose their hysteresis property. This can be seen in Figure 6.6. The Coercivity at 5K is ~200 Oe which decreased to ~ 0 Oe at 300 K. The remanent magnetization also decreases from 2.5×10^{-5} emu to ~ 0 emu as the substrate temperature increased from 5 K to 300 K. The coercivity and remanence magnetization at 300 K becomes zero (Figure 6.6) whereas the magnetic moments follow the direction of the applied magnetic field which suggests that the sample is in a superparamagnetic state.
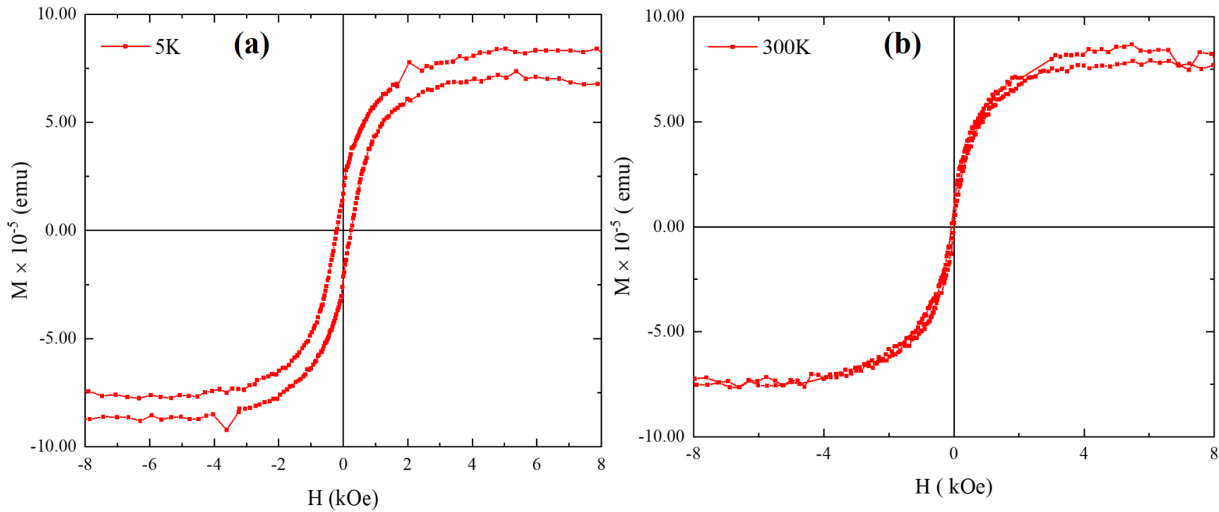
Figure 6.6: Hysteresis loop (M vs H) of 50 keV Co irradiated Si with a fluence of 3.2×10^{16} ions/cm². (a) shows the magnetic behavior at 5 K and (b) the magnetic behavior at 300 K.

6.5   Conclusion

We have demonstrated the synthesis of a cobalt-based superparamagnetic nanostructures in silicon using 50 keV energetic ion implantations. The dynamically simulated cobalt

concentration depth profile for this irradiation process matches closely with the experimental depth-profile. The magnetic measurement showed that the synthesized structure is in a ferromagnetic state at 5 K but becomes superparamagnetic as it approaches room temperature. The synthesized sample has a higher blocking temperature of 120 K.

CHAPTER 7

MODELLING AND EXPERIMENTAL STUDY OF IRRADIATION OF PRE-FABRICATED

SILICON NANO-POST AND ANALYSIS OF ELEMENTAL DISTRIBUTION USING ATOM

PROBE TOMOGRAPHY

7.1   Introduction

As nanostructures have curved surface geometry, it's difficult to simulate the effect of ion

irradiation using conventional ion-solid interaction simulation codes. To accurately determine the

distribution of ions in a nanoscale target, it is better to consider simulation codes in which the

target can be defined as three-dimensional cubical grids, to allow the curved surface geometry of

nanowires or nanoparticles. It will be more accurate to define the target with a curved surface in

the simulation code itself rather than extracting the result from the 1D code where the target is

usually has a flat surface. This way the sputtering, depth profile, damage formation, etc. can be

accurately predicted, which is essential for considering the effect of ion irradiation in

nanostructures. Implanting ions directly into nanowires can modify their functional properties and

annealing the implanted nanowire at different temperatures can facilitate the formation of various

alloys in the nanowire. Recently, several groups have reported studies utilizing codes like Iradina,

which can incorporate targets involving curved surface geometry and shows many realistic results

in the case of ion irradiation in nanostructures (specifically nanowire) in comparison to 1D codes

like TRIM or SDTrimSP. In this chapter, we will discuss the effect of ion irradiation on pre-

fabricated nanostructures and will provide a direct comparison of modeling data with the elemental

distribution from the experimental results.

7.2   Reported Studies Based on Nanowires Using Iradina

Over the last few years, many researchers have used Iradina to estimate the implantation

and defect profile due to ion irradiation in the case of nanowire and have compared the simulation results with the experimental data. Their study shows that results from the Iradina simulation match more closely with the experimental data. Here we have discussed some of those cases where Iradina was used to model the ion solid interaction and showed comparable results.

Segura-Ruiz et al. have reported the study of the properties of the local structure of Co-implanted ZnO nanowires of 180 nm diameter and 7 μm length using a hard x-ray nanoprobe. In this study, the Co ions were implanted at a fluence of 1.57×10^{16} atoms/cm^2 with ion energies ranging from 60 keV to 300 keV to obtain a homogeneous concentration profile. The ion irradiated nanowires were annealed at 750 °C in the air for four hours to recover from the radiation-induced lattice damage. In this study, the simulated concentration of Co in the ZnO nanowires was compared with the elemental maps of Zn and Co ions along the NW obtained from the experiment. The average concentrations of Co and Zn were (0.3 ± 0.1) and (49.7 ± 0.1) atom %, respectively. These values show good agreement with the simulation results obtained from the Iradina code [87]. Borschel et al. have reported the study of permanent bending and alignment of ZnO nanowires using ion irradiation. In this study, they have used ion irradiation to permanently bend and re-align ZnO nanowires after the growth. They have used Iradina to simulate the ion irradiation process which explains the bending of the nanowires initiated by ion beam-induced damage [88]. Borschel et al. have also reported the study of highly Mn-doped GaAs nanowires by ion-implantation under dynamic annealing conditions. In this study, they have used the Iradina code to simulate the Mn concentration in GaAs NWs irradiated with Mn at various fluences. They have compared the simulation results of the SRIM simulation with Iradina for this specific case. The results show that SRIM overestimated the Mn concentration in the nanowires by a factor of 1.7 [89]. Ernst et al. have reported the study of thin crystalline macro-porous silicon solar cells with

the ion-implanted emitter. In this study, they have used Iradina to simulate the fraction of backscattered ions as a function of the angle of incidence of the ion beam [90]. Guerra et al. have studied the modification of structure and morphology of Bi nanowires of two different diameters (80 or 130 nm) irradiated with 400 keV and 1 MeV Au+ beams for the fluences up to ~1 ion/nm^2. In this study, they have used Iradina to simulate the depth profile and sputtering of ion irradiated Bi nanowires [91]. Johannes et al. have studied the sputter yield of ZnO and GaAs nanowires irradiated with energetic Mn ions at room temperature both experimentally and using Iradina simulation. Their research shows that the sputtering in the case of a nanowire is 1.7 times higher compared to the bulk material [92]. Csato et al. have designed an energy filter for doping in the semiconductor in which they have used the Iradina code to simulate the depth profile of 7 MeV boron ions implanted into different substrate materials [93]. Johannes et al. have studied the anomalous plastic deformation and sputtering of Ar irradiated Si nanowires in which Iradina code was used to simulate the ion range and sputtering of the Si nanowires [94]. Holland-Moritz et al. have reported the study of enhanced sputter yields in the case of ion irradiated Au nanoparticles as a function of ion energy and nanoparticle size. In this study, they have used the Iradina code to simulate the depth profile and sputtering yield of gold nanoparticles due to ion irradiation. The results show that sputtering is significant in the case of irradiating the nanostructures. Their studies have shown that the Iradina code provides a good qualitative prediction of the number of sputtered atoms in nanostructures, but especially when irradiating heavy or dense materials, the sputter yield is underestimated [95]. All the mentioned studies above have shown that Iradina simulation results are in good agreement with experimental data.

7.3   Simulation Details

Theoretical ion solid interaction simulations were carried out before the ion implantation

79

process to estimate the distribution of ions inside the nanowire. The initial simulation was carried out using Iradina with few numbers of ions. Then the number of ions was increased gradually till the noise of the simulation was sufficiently small. When the simulation was carried out for 5×10^5 ions, the noise was extremely small. This is consistent with our TRIM and SDTrimSP simulation. As described earlier, Iradina has been successfully used by many researchers to predict the distributions of ions inside a nanowire or nanoparticle. The Iradina can be set up to generate output data in terms of $(atoms/cm^3)/(atoms/cm^2)$. The output result was then multiplied with specific ion fluences to get the implanted concentration in terms of $atoms/cm^3$. A brief description of the simulation details is discussed below.

For this study, the nanowire version of Iradina was used in which the target was considered as a solid cylinder of fixed radius. The incoming direction of the ion beam was chosen to be the +X axis and was perpendicular to the axis of the NW. A small segment of the NW was considered for the simulation and periodic boundary condition was applied along the nanowire axis (+ Z-axis). This leads to a nanowire of infinite length. The simulation volume was defined as a cube of dimensions such a way that the length of the cube is identical to the diameter of the nanowire and was placed around the NW. The simulation volume was then divided into 1 nm × 1 nm × 1 nm cubical cell. The cells inside the NW are filled with the target materials (Si) and the cells outside the NW were set to vacuum. It is essential to choose the outside material as a vacuum so that the ions can be tracked as they exit the silicon nanostructure. The simulations were carried out for Co/Fe ions implanted with single energy onto the Si NWs with various diameters.

7.4   Experimental Details

As a demonstration case, the samples were prepared by implanting ions directly onto pre-fabricated Si nanotips. The nanotips are pre-sharpened (<50 nm tip radius) microtip coupons

suitable for LEAP analysis without specimen preparation. The nanotips were procured from Cameca Istruments, Inc, USA. 50 keV Fe⁻ and/or Co⁻ ions extracted from a solid cathode used in the SNICS-II were irradiated on the silicon nanotip samples. Also another sample was prepared by irradiating a smooth silicon substrate. The beam was electrostatically raster-scanned over a circular aperture of radius 1 cm to ensure homogeneous implantation on the target material. The implantation chamber was kept under a high vacuum with a residual pressure of 9×10^{-8} mbar. A schematic of the ion implantation setup is shown in Figure 7.1.
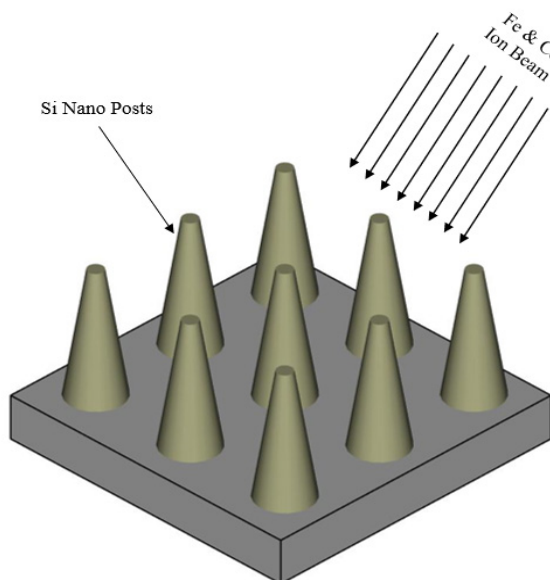
Figure 7.1: Schematics of the ion irradiation experimental setup for Si nano-posts.

After the implantation, the samples were characterized using Atom probe tomography (APT) where the irradiated Si nano-tips were evaporated layer by layer using a pulsed laser to study its structural composition. The samples from the smooth silicon substrates were prepared using a FEI™ Nova 200 dual-beam focused ion beam (FIB). Ga ion beam operating at a voltage of 30 kV was used to mill the prism-shaped lift out from the sample with an approximate dimension 3 μm ×3 μm ×4 μm . The Ga beam current was kept at 3 nA for this process. The sample was then further processed to a conical needle with ~50 nm diameter at a depth of 100 nm from the vertex.

Final polishing of the conical needle was performed with Ga ion operating at 5 kV and 70 pA current. The APT measurement was performed using Cameca LEAP 5000XS 3D Atom Probe Microscope where the APT tip was kept at a temperature of 30 K during the measurement. The leaser used to evaporate the sample had a pulse rate of 200 kHz, and a detection rate of 0.005-0.03 ion/pulse. The laser pulse energy was set to 50 nJ. AP Suite 6 software was used to analyze the APT data.

7.5   Simulation Results

Several ion beam simulations were carried out using Iradina simulation code by varying the ion energy and nanowire diameter. The ion beam was chosen to be either Fe or Co and the target material was silicon. The Co and/or Fe beam was incident from +X direction. The cross-sectional view of the nanowires is shown in Figure 7.2. In this simulation, 50 keV cobalt beam was incident on the nanowire where the diameter of the wire was changed in each case keeping other simulation parameters constant. As shown in the Figure 7.2, with the increase in the diameter of the nanowire, a greater number of ions reside within the nanowire. For 20 nm diameter, the concentration of ions is below 0.05% as most of the ions pass through the material. With the increase in diameter, the ions lose more energy to the target atoms and follow multiple scattering.

As the result shows, the high concentration region of the implanted ions in the target shifts towards the left implying that a greater number of ions are interacting with either target electrons or target atoms and losing their energy. For 50 nm diameter, the highest concentration of irradiation is towards the edge of the nanowire whereas for 80 and 100 nm diameter it is more towards the center. The simulation for a higher diameter nanowire is shown in Figure 7.3. A curved depth profile is observed in this case where the implanted ions are near the surface of the nanowire. The range of ions is more along the edge compared to the central region because the ions travel a

different path for a different region of the nanowire. Another reason for this kind of behavior is that the ions enter the target at different angles for different regions and previous simulations showed that the depth and concentration of the implanted ions are affected by the incident ion angle.
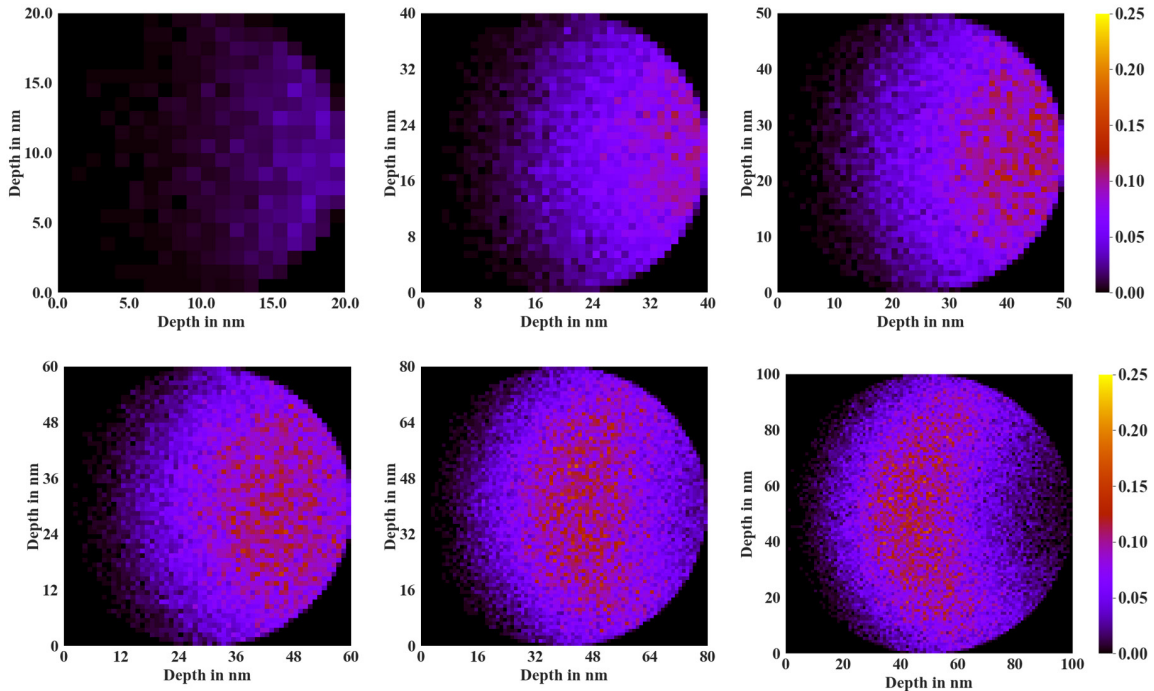
Figure 7.2: Simulated depth profile of Co in Si where the cobalt ion beam energy was 50 keV and the results were simulated by changing the nanowire diameter as shown in the figure.
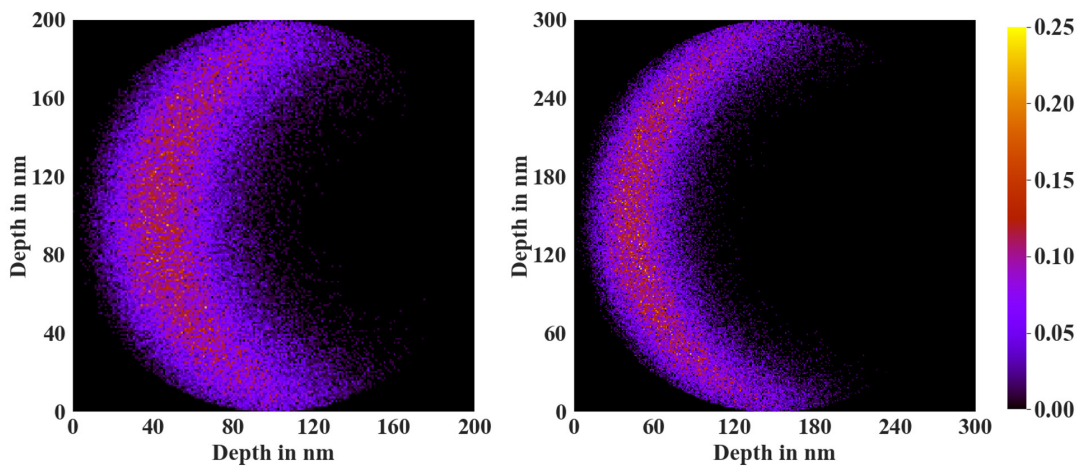
Figure 7.3: Simulated depth profile of 50 keV Co in Si where the diameter of the Si nanowire is 200 nm and 300 nm.

As discussed in Chapter 4, changing the incidence angle hugely affects the ion distribution and a similar effect can be observed here. Similar modeling was carried out using Fe as the incoming ion beam and identical results were observed as the mass difference between Fe and Co is very small. The simulated results are shown in Figures 7.4 and 7.5.
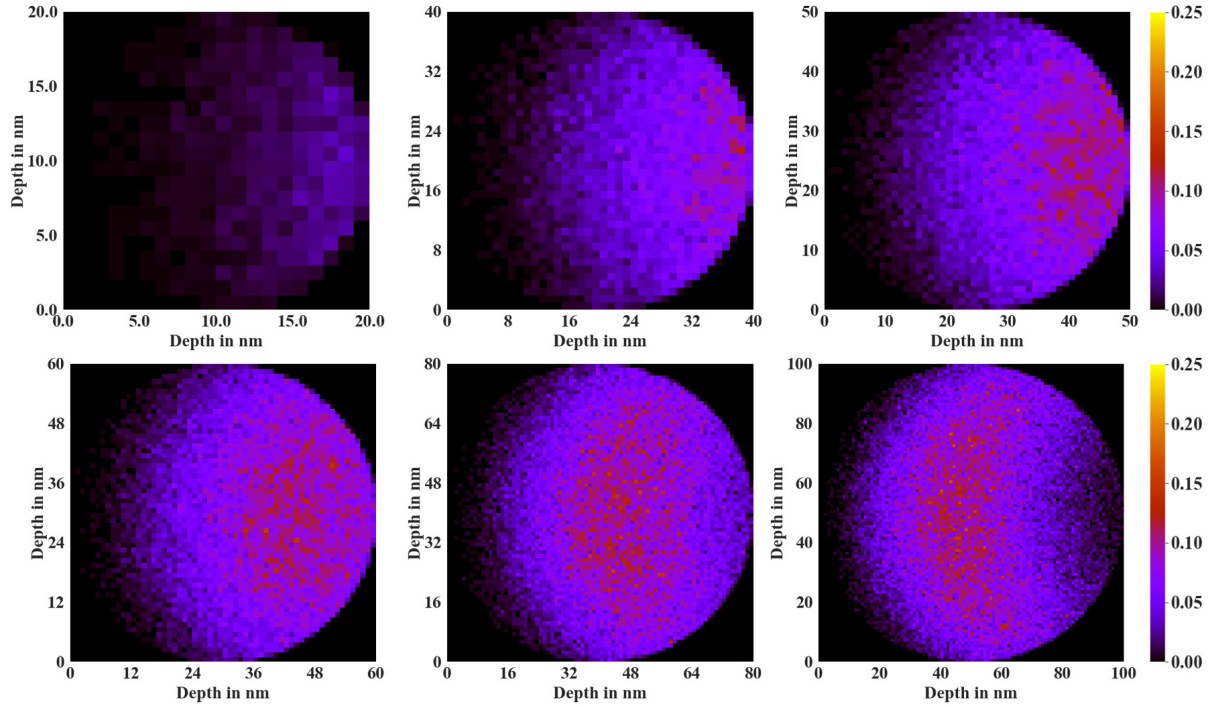
Figure 7.4: Simulated depth profile of Fe in Si where the ion beam energy was 50 keV and the results were simulated by changing the nanowire diameter as shown in the figure.
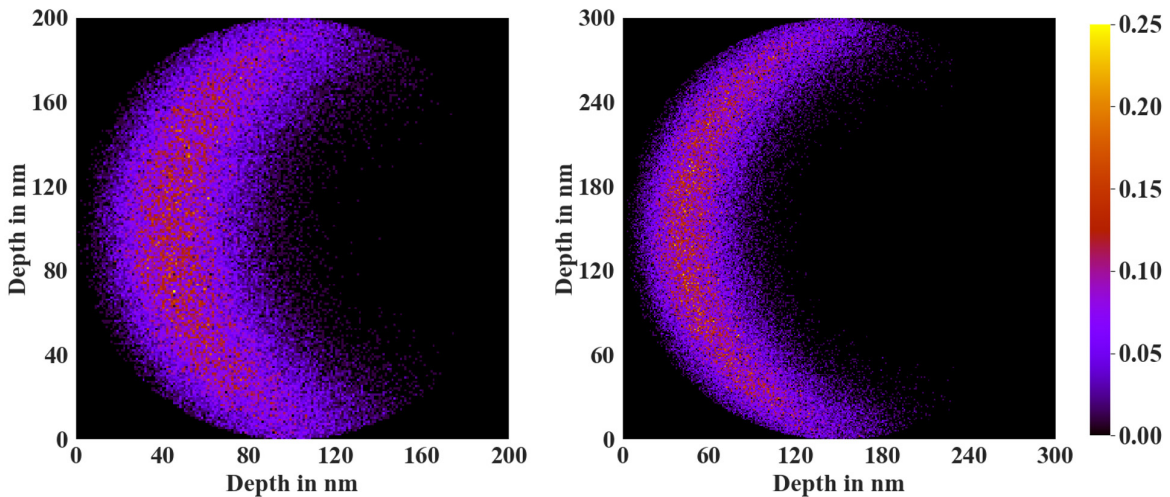
Figure 7.5: Simulated depth profile of 50 keV Fe in Si where the diameter of the Si nanowire is 200 nm and 300 nm.

Another set of simulations were carried out by varying the incoming ion energy and keeping the diameter of the nanowire constant. The simulations were only carried out for Co ions as previous simulations showed no significant difference between Fe and Co profiles. The energy of the ions was varied from 10 keV to 40 keV (as the 50 keV case is already discussed earlier). The diameter of the nanowire was chosen to be 50 nm. The simulated results are shown in Figure 7.6.
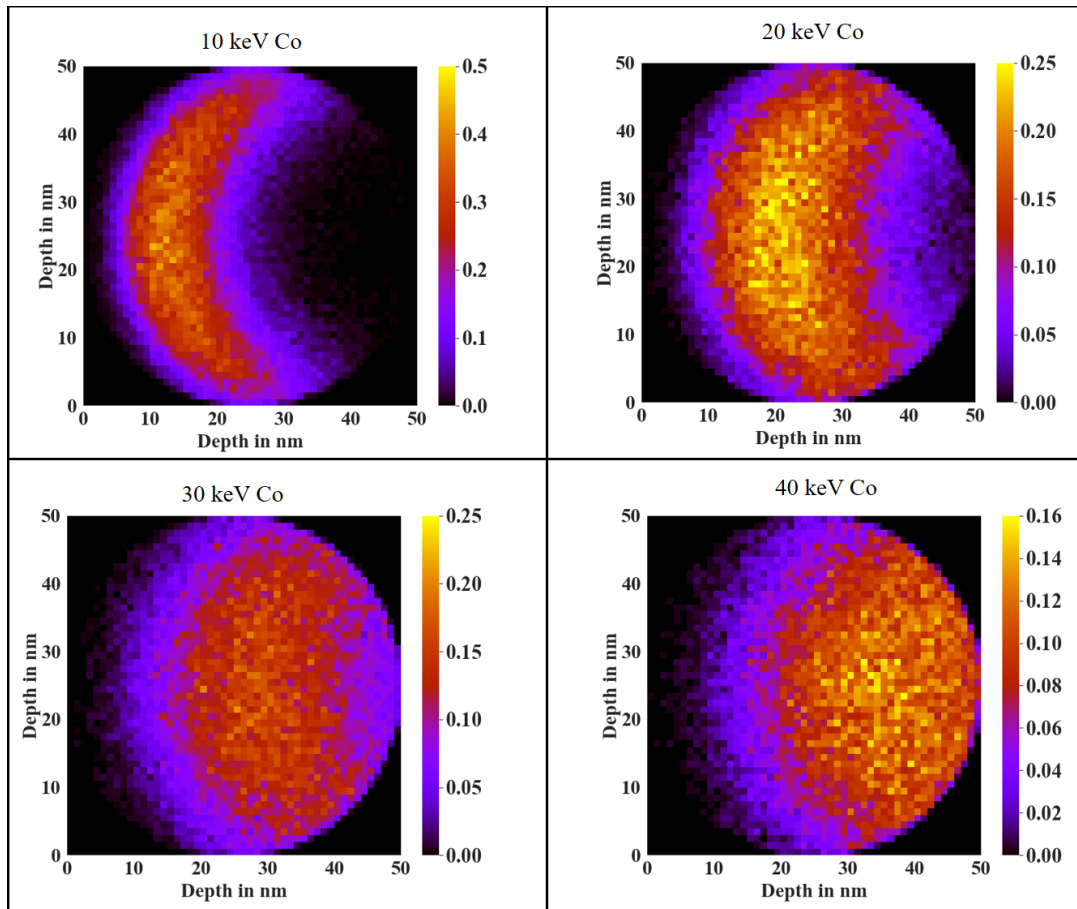
Figure 7.6: Simulated results of 10 - 40 keV Co ion irradiated on to a 50 nm diameter of Si nanowire using Iradina code. The results show the cross-sectional view of the simulation structure where the variation of depth profile can be observed. The implanted ions are represented in the unit of cobalt percentage in with respect to silicon.

The results showed that with the increase in ion energy, there is a sharp decrease in the implanted concentration. This is because more energetic ions have a higher probability of leaving the target rather than contributing to the implantation concentration. The peak concentration of the

implanted ions decreased sharply from 45% to 15% as the energy is increased by 20 keV. Around 40 – 50 keV, the range of the implanted ions is comparable to the diameter of the nanowire. Hence, most ions directly pass through the nanowire creating target damages.

7.6   Experimental Results

Several experiments were carried out to study the distribution of ions in the nanostructures. In each case, the silicon nanotip was irradiated with a different condition. Figure 7.7 shows the SEM image of all the cases where APT was used to study the distribution of ions inside the silicon Matrix. In each image (a, b, and c) the tip appears to be sharp however in the case of Co irradiated with a fluence of 5×10^{16} ions/cm^2.
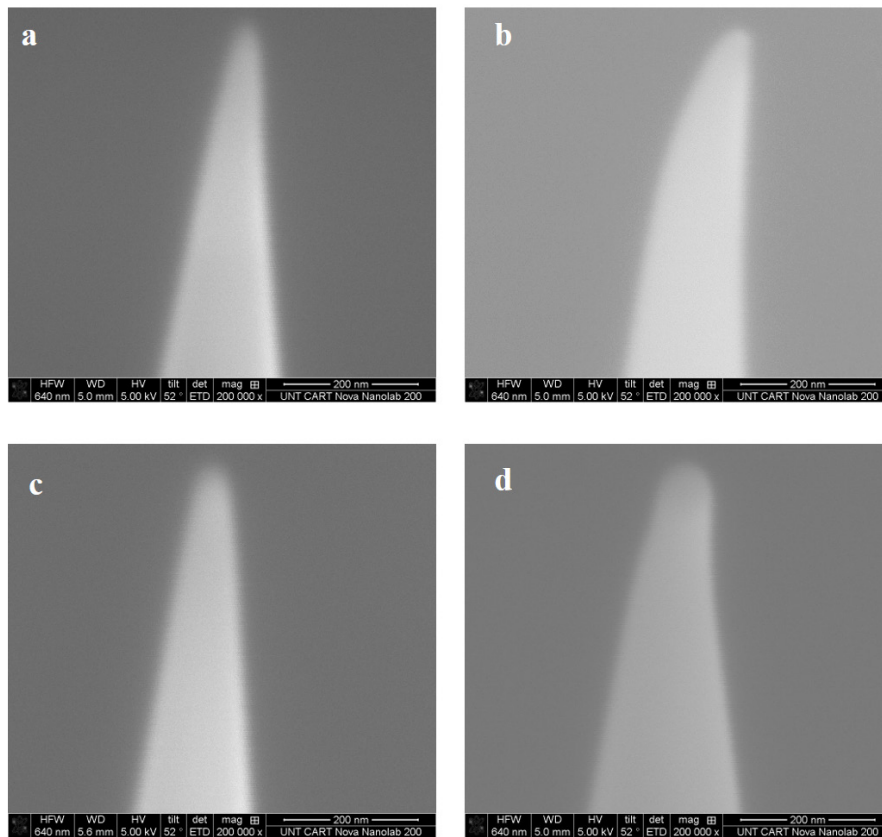
Figure 7.7: SEM image of (a) pre synthesized Si nano-tip irradiated with fluence of 2.5 × 10^{16} ions/cm^2 (b) tips prepared by FIB technique from Si substrate irradiated with fluence of 2.5 × 10^{16} ions/cm^2 (c) pre-synthesized Si nano-tip irradiated with equal amount of Fe and Co to a total of 2.5 × 10^{16} ions/cm^2 fluence and (d) pre-synthesized Si tip irradiated with a fluence 5 × 10^{16} ions/cm^2. In each case the cobalt, the irradiation energy was 50 keV.

This is due to the sputtering of the Si due to high fluence irradiation as discussed in Chapter 4. For case "d", the APT was not performed as the experiment requires a sharp tip and due to sputtering in the case of 5×10^{16} ions/cm^2 irradiation, it was not suitable for the experiment. In this section, we will discuss the results of the APT for cases a, b and, c.

7.6.1   Results from Irradiation of Si Nano-Post

For the first study, the pre-synthesized Si nano-posts were irradiated with 50 keV Co to a fluence of 2.5×10^{16} ions/cm^2. The beam current was kept relatively low (< 50 nA/cm^2). After the irradiation, layer by layer of the sample surface was sputtered to study the composition of the ion irradiated nano posts. A cross-section of 60 nm × 60 nm was chosen at the center of the sample and implanted ion maps were collected for various depths. The top of the sample surface (top of the nano-post) was considered to be Z = 0 nm and into the sample was considered as +Z direction. The ions maps for various depths are shown in Figure 7.8.
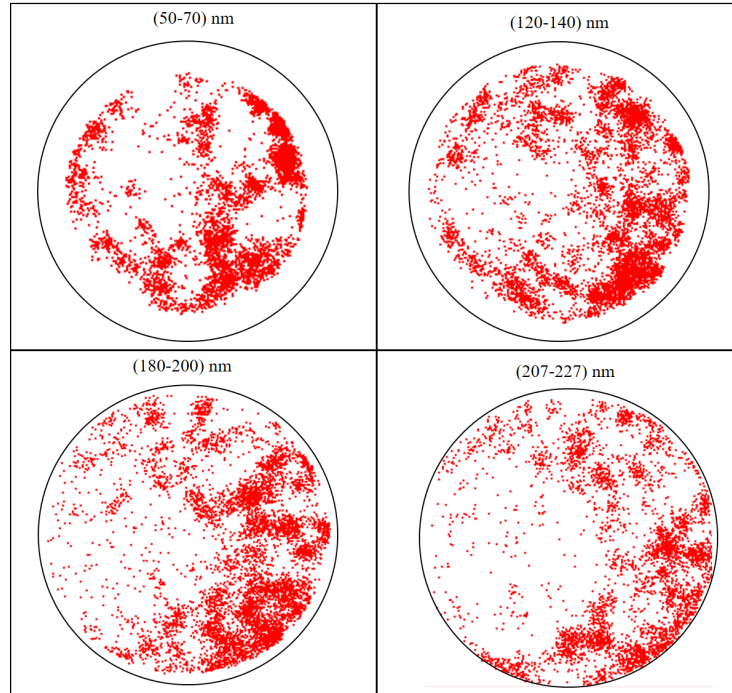
Figure 7.8: Cross-sectional (60 nm × 60 nm) view of the ion irradiated nano-post where each point represents the location of Co ions inside the nano-post. The depth in Z direction is shown above each figure.

The profile of the irradiated ion is similar to our modeling. Near the top of the tip, most of the ions are clustered throughout the cross-section. As Z increases the ions start to accumulate and a curved profile can be seen in the image. For Z between 120 nm -140 nm, the curved profile of ions can be seen and for Z around 200 nm, the curved profile is visible. This is similar to our predicted results from Iradina which showed that even constant energy is applied to the ions, different ions travel differently depending on the entry point on the target surface.

The concentration of the implanted ions in the Si nano-posts is shown in the form of a heat map. Figure 7.9 shows the concentration profile of the ions for various Z depths. As we go into the substrate deeper, the cobalt concentration changes. However, the concentration is still below 10 % and not higher as predicted by the Iradina code.
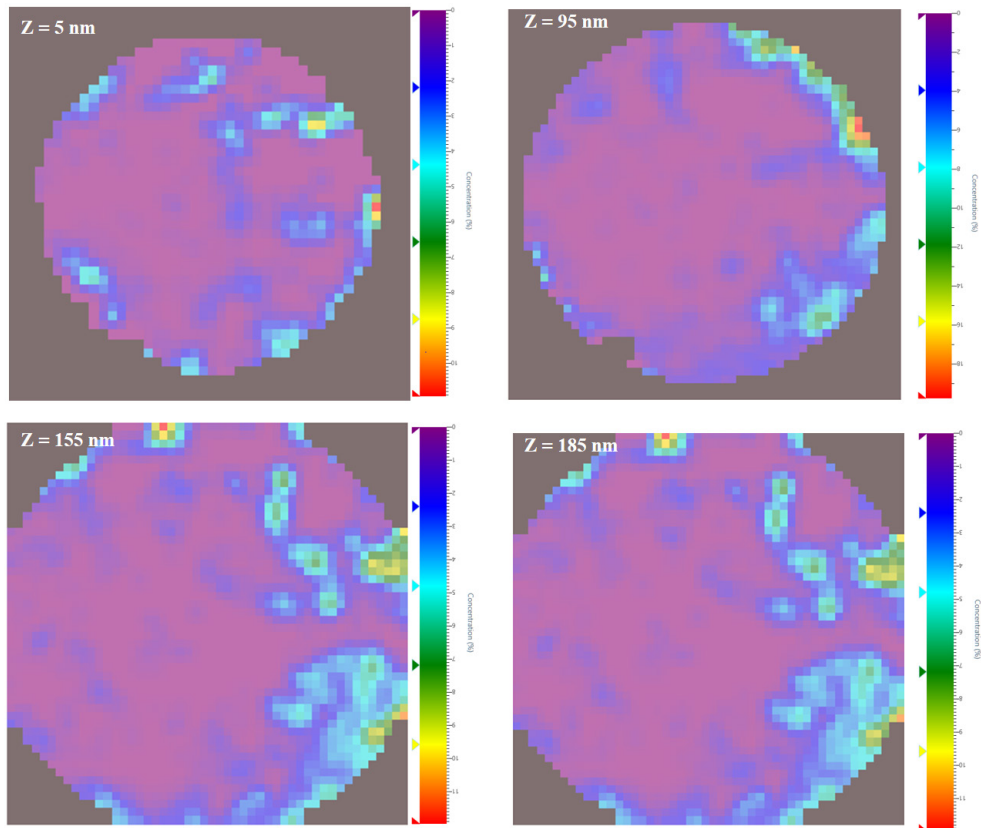
Figure 7.9: Heat map of the ion irradiated nano post where the concentration of Co ions inside the nano-post are shown in color. The depth in Z direction is shown above each figure.

This can be explained as follows. Iradina code is static which means that it does not update the target composition during the irradiation process. As discussed in Chapter 4, the static code overestimates the concentration whereas dynamic code can accurately predict the distribution. In this case the experimental and simulated concentration vary slightly but the profile of the implanted ions is curved in nature as predicted by Iradina. Figure 7.10 shows the total reconstruction of the tip. As the image shows, most of the cobalt ions are concentrated at the top and the concentration gradually decreases as the depth is increased.

Figure 7.10: Full reconstruction of both Co and Si atoms distribution where Si nano-post was irradiated with 50 keV Co at a fluence of 2.5×10^{16} ions /cm^2.

7.6.2   Results from FIB Extracted Sample from Si Substrate

A second study was done to compare the distribution of ions from pre-fabricated Si nano-post with the sample extracted using FIB from the silicon substrate. In this case, the first Co was irradiated at 50 keV on to Si wafer. The ion fluence and beam current were identical as compared

to Si nano posts. Then using Focused Ion beam lithography, APT tips were created. The image of the tip is shown in Figure 7.7 (b). Then the surface of the tip was sputtered layer by layer to collect the atomic concentration data. Figure 7.11 shows the profile of the implanted Co ions for various depths.

Figure 7.11: Cross-sectional (60 nm × 60 nm) view of the ion irradiated Si wafer where each point represents the location of Co ions inside the substrate. The depth in Z direction is shown above each figure.

In Figure 7.11, it is clear that with increased in-depth, the concentration of the Co ions is also decreased. This is slightly different compared to the nano post. For the silicon substrate, the ions are distributed only on the top 100 nm and the density of the implanted ions decreases sharply as the depth increases. This is because in the case of a substrate that has a flat surface, each ion travels a similar distance within the target and the projected range of 50 keV Co in Si is around 100 nm. In the case of nano posts, the ions can travel to different depths because of the curvature

surface. Figure 7.12 shows the full reconstruction of the prepared tip and the length of the

reconstruction is 200 nm. Figure 7.13 shows the concentration of irradiated Co ions in the silicon

substrate. As discussed above, most ions are at the top part of the sample and the concentration

decreases as we go to higher depths.
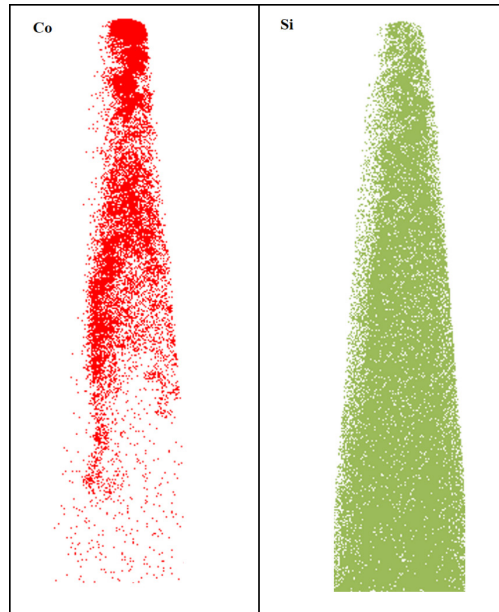
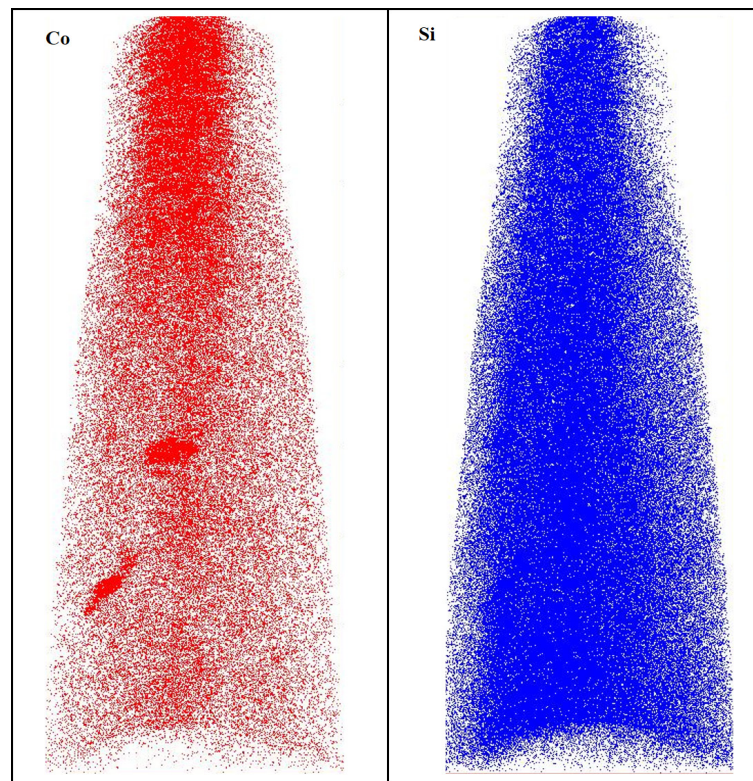**Figure 7.12: Full reconstruction of both Co and Si where Si nano post was irradiated with 50 keV Co at a fluence of 2.5 × 1016 ions /cm2. The total length of the reconstruction image is 200 nm.**
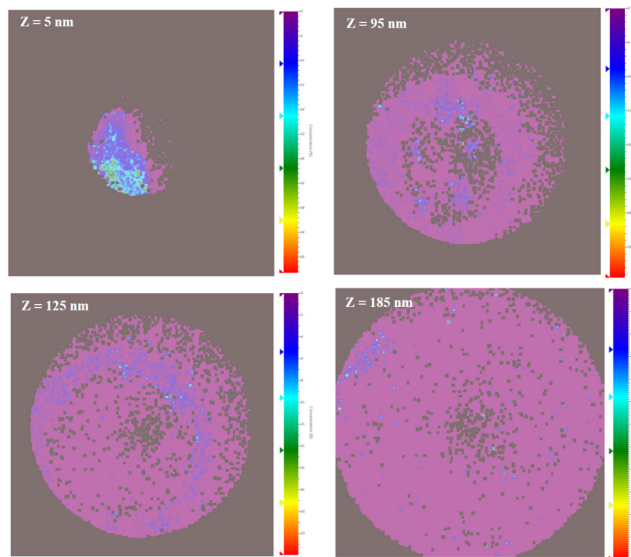
Figure 7.13: Heat map of the ion irradiated Si substrate where the concentration of Co ions inside the substrate are shown in color. The depth in Z direction is shown above each figure.

7.6.3 Results from Fe and Co Sequentially Implanted in Si Nano-Posts with a Fluence of 1.2×10^{16}

The third study was done where the Si nano post was irradiated with an equal amount of Fe and Co at 50 keV to a total fluence of 2.5×10^{16} ions/cm². Fe was irradiated first and then Co was irradiated. The experimental conditions were kept identical to the first and second cases. The cross-sectional profile of Fe and Co for various depths is shown in Figure 7.14. Co has a higher concentration compared to Fe. Since Co was irradiated after Fe, some of the Co ions can sputter the Fe ions from the target and take their position in the Si matrix.

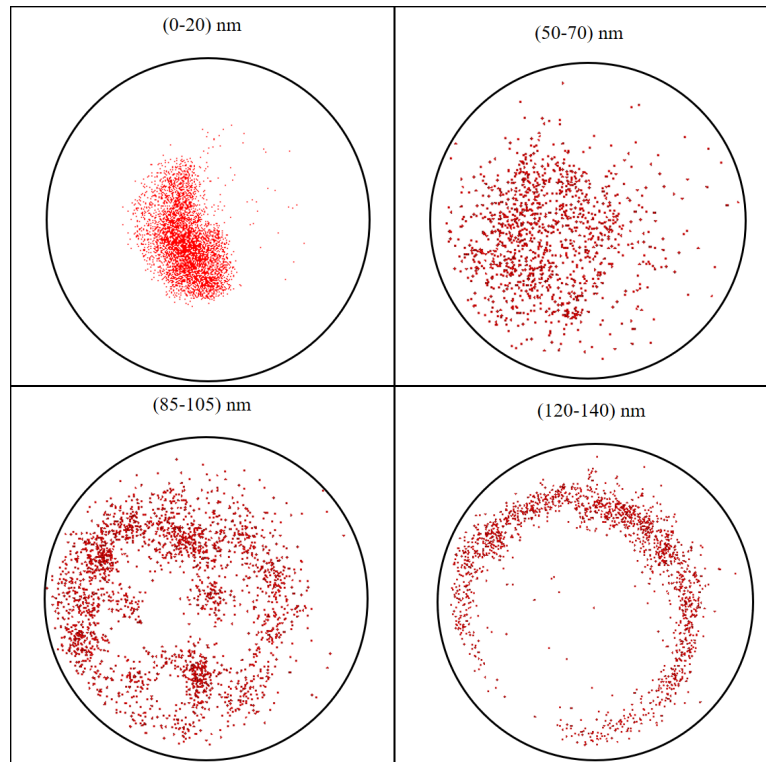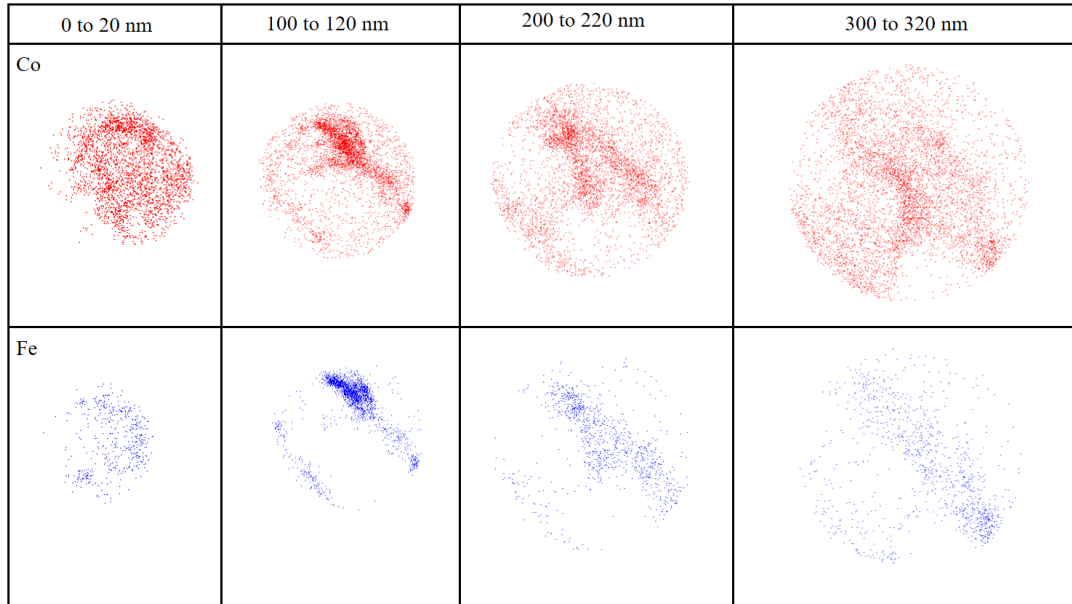**Figure 7.14: Cross-sectional view of the ion irradiated nano post where each point represents the location of Co and Fe ions inside the substrate. The Co ions are represented on the top and Fe ions are represented at the bottom for a certain location inside the sample. The depth in Z direction is shown above each figure.**

Figure 7.15 shows the Full reconstruction of the Si nano-post where individual ions are shown. The total length of the reconstruction is 480 nm. It is clear from the image that the Co concentration is relatively higher compared to Fe. Figures 7.16 and 7.17 represent the quantitative data for this case. It is also clear for these Figures that at each Z value, the Co has a higher concentration than Fe.
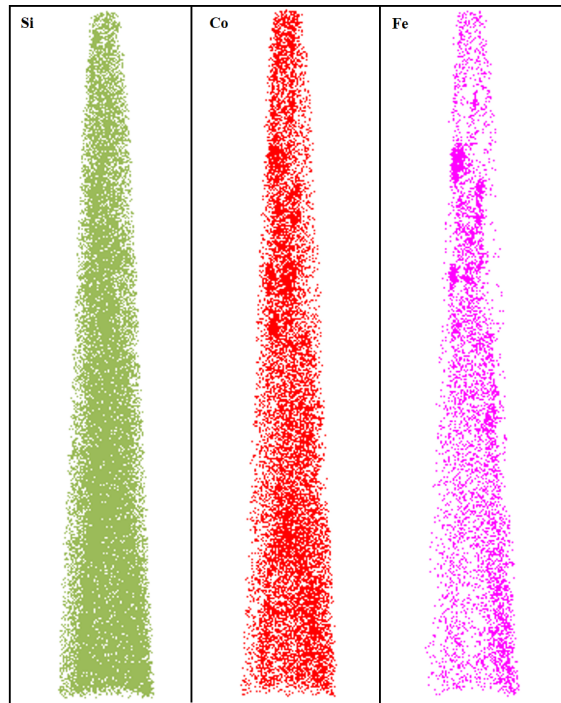
Figure 7.15: Full reconstruction of both Co and Fe in Si where Si nano-post was irradiated with 50 keV Co and Fe to a total fluence of 2.5 × 1016 ions /cm2. The total length of the reconstruction image is 480 nm.
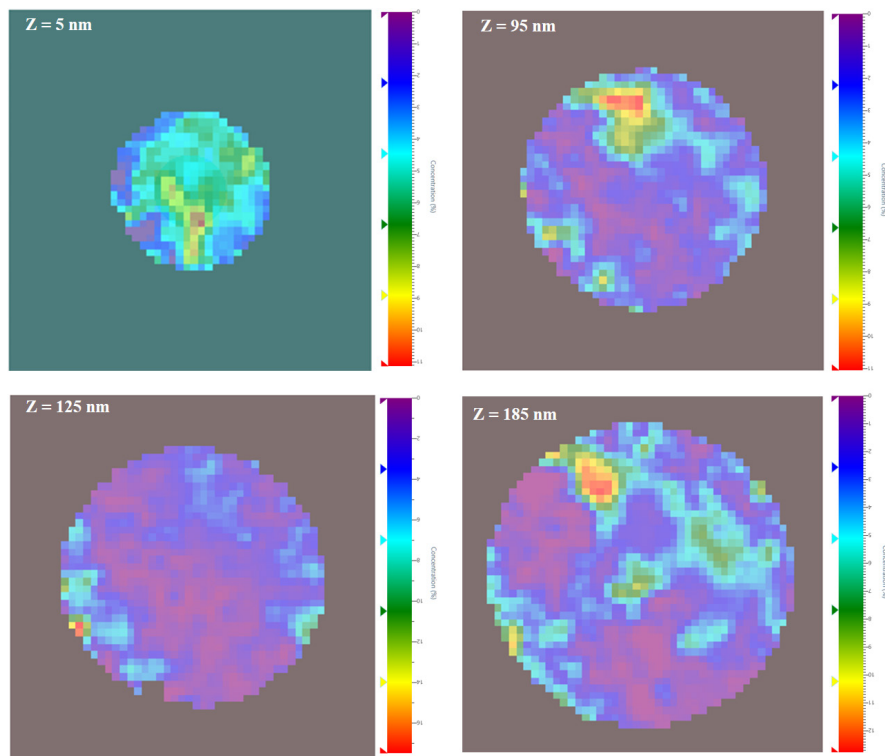
Figure 7.16: Heat map of the Si nano-post irradiated with 50 keV Fe and Co sequentially to a total fluence of 2.5×10^{16} ions /cm^2. The concentration of Co is shown in this map. The depth in Z direction is shown above each figure.

93
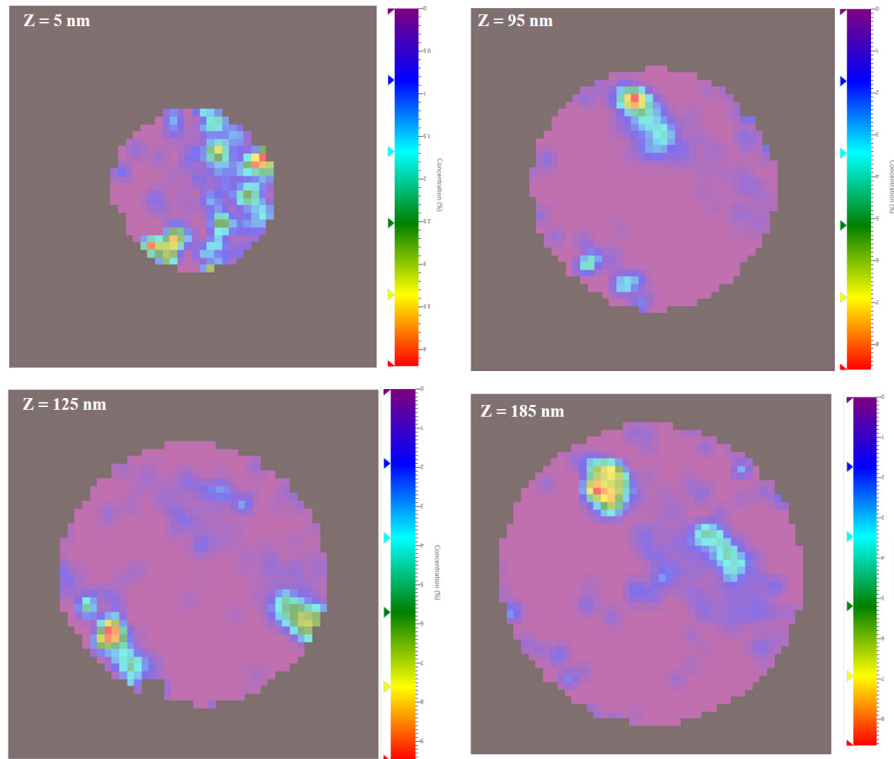
Figure 7.17: Heat map of the Si nano post irradiated with 50 keV Fe and Co sequentially to a total fluence of 2.5 × 10^{16} ions /cm^2 .The concentration of Fe is shown in this map. The depth in Z direction is shown above each figure.

7.7   Conclusion

The experimental results from atom probe tomography analysis show that the irradiated ions have a curved depth profile in the Si nano-posts. The results are similar to the simulated profiles predicted by the Iradina code. The distribution of the implanted ions in the nano-posts is not uniform and the profile changes with change in diameter. The distribution also follows the curvature of the nano wires. The concentration of the implanted ions in the Si substrate is slightly lower compared to the nano posts for a given fluence. In our experiment for the case of sequential irradiation, the ion irradiated first (Fe) has a lower concentration compared to the second one (Co). In this case, the incoming Co ions replaced some of the Fe ions in the Si as both Fe and Co have atomic mass very close to each other.

CHAPTER 8

SUMMARY

Among many processing methods, ion implantation followed by post-implantation thermal annealing is one of the most efficient methods for synthesizing nanostructures in various semiconductors. The implanted ions gradually amorphized the Si substrates as the ion fluence increases while getting distributed at a shallow depth near the substrate surface. At higher fluences, the substrate surface gets sputtered and the implanted species move to the near-surface region. Ion implantation provides control over the ion species, depth, and concentration of the implanted ions in the target. The control over the ion depth and concentration can be simulated using various simulation methods as described in this study. We have shown that one of the key factors when simulating the ion irradiation process is to choose the appropriate simulation code. The distribution of the implanted ions in a certain target differs considerably by choosing a static or dynamic and 1D or 3D simulation code. If the target surface is not flat and has curvatures, it is difficult to estimate the distribution of ions only using the most popular TRIM code. The Iradina code showed much more realistic results in the case of the target with curved surfaces in 3D such as nanowires. Our simulations also showed that for a specific condition (energy and angle of incidence) of implantation, there exists a saturation fluence that provides the maximum concentration of heavy ions that can be implanted into a lighter atom target, beyond which the concentration of implanted ion does not increase further. Thus, these ion-solid interaction simulations can be used to generate implantation parameters input parameters of the desired implant distribution which can save the time and effort of performing multiple experiments.

As described in the introduction, the interest in synthesizing iron and cobalt-based nanostructures is due to potential application in biomedical fields. In ion implantation, the

implanted ions can be redistributed inside the target. One of the mechanisms responsible for the redistribution of atoms is localized thermal annealing. In our study, we have developed a new fabrication process for the formation of iron-rich Silicon nanostructures using bombardment of low energetic Fe ion beams on silicon at high beam current. This allows dynamic annealing of the sample at the nanoscale which facilitates the formation of iron-rich nanostructures. We have discussed the successful synthesis of Fe_5Si_3 nanocrystals embedded in Si using 50 keV Fe^- implantation at a fluence of 2×10^{17} ions/cm^2 and post-thermal vacuum annealing at 500 ^oC for one hour. The synthesized structures are formed with 38 nm to 70 nm long-grain nanocrystals embedded in Si. The experimental depth distribution confirmed the presence of a high concentration of iron near the surface region of the irradiated Si as predicted by the SDTrimSP simulation. These synthesized nanostructures are superparamagnetic with a very small coercive field and this superparamagnetic behavior is present even at room temperature.

Our study involving low energy Co ion irradiation in silicon showed interesting magnetic properties. Our simulated depth profile before the irradiation process matches closely with the experimental depth profile. The magnetic measurement of the synthesized structure showed that it is in a superparamagnetic state at room temperature. The synthesized structure also has a higher blocking temperature of 120 K.

Our final study in this research involving Si nano posts showed promising results. As predicted by the Iradina code, the distribution of the implanted ions in the nano posts is not uniform and has a curved depth profile. This further confirms our previous discussion regarding optimizing the experiment using simulation rather than performing physical experiments.

We have shown that superparamagnetic nanostructures can be synthesized using low energy ion irradiation. Further research can be done to develop a dynamic 3D simulation code that

can predict the distribution of ions in nanowires or nanoparticles quantitatively. Several simulations can be performed to predict the optimal experimental conditions such as ion energy, fluence, and angle of incidence for a specific ion that can be implanted on a nanoparticle. Once irradiated, the magnetic properties of these nanoparticles can be studied to investigate the nature of their magnetism. Further experiments can be carried out by changing the implantation parameter to synthesize superparamagnetic nanoparticles of various diameters. Once synthesized, these nanoparticles can be encapsulated in biocompatible polymers and be used in various biomedical applications.

REFERENCES

[1]   X. Fang, L. Wu, Handbook of Innovative Nanomaterials: From Syntheses to Applications, Jenny Stanford Publishing, 2012.

[2]   H. Watanabe, H. Yamamoto, K. Ito, Neutron Diffraction Study of the Intermetallic Compound FeSi, J. Phys. Soc. Jpn. 18 (1963) 995–999. https://doi.org/10.1143/JPSJ.18.995.

[3]   A.R. Weill, Structure of the Eta Phase of the Iron-Silicon System, Nature. 152 (1943) 413. https://doi.org/10.1038/152413a0.

[4]   Y. Chen, J. Qian, Y. Cao, H. Yang, X. Ai, Green Synthesis and Stable Li-Storage Performance of FeSi2/Si@C Nanocomposite for Lithium-Ion Batteries, ACS Appl. Mater. Interfaces. 4 (2012) 3753–3758. https://doi.org/10.1021/am300952b.

[5]   D. Leong, M. Harry, K.J. Reeson, K.P. Homewood, A silicon/iron-disilicide light-emitting diode operating at a wavelength of 1.5 μm, Nature. 387 (1997) 686.

[6]   K. Takakura, H. Ohyama, K. Takarabe, T. Suemasu, F. Hasegawa, Hole mobility of p-type β-FeSi2 thin films grown from Si⁄Fe multilayers, J. Appl. Phys. 97 (2005) 093716. https://doi.org/10.1063/1.1891279.

[7]   M. Miu, I. Kleps, T. Ignat, M. Simion, A. Bragaru, Study of nanocomposite iron/porous silicon material, J. Alloys Compd. 496 (2010) 265–268. https://doi.org/10.1016/j.jallcom.2010.01.058.

[8]   W.A. Jensen, N. Liu, E. Rosker, B.F. Donovan, B. Foley, P.E. Hopkins, J.A. Floro, Eutectoid transformations in Fe-Si Alloys for thermoelectric applications, J. Alloys Compd. 721 (2017) 705–711. https://doi.org/10.1016/j.jallcom.2017.06.023.

[9]   X. Dai, L. Zhang, J. Li, Z. Wang, H. Li, Electronic transport properties of heterojunction devices constructed by single-wall Fe2Si and carbon nanotubes, J. Mater. Chem. C. 6 (2018) 5794–5802. https://doi.org/10.1039/C8TC01708E.

[10]   Y. Sun, Z. Zhuo, X. Wu, J. Yang, Room-Temperature Ferromagnetism in Two-Dimensional Fe2Si Nanosheet with Enhanced Spin-Polarization Ratio, Nano Lett. 17 (2017) 2771–2777. https://doi.org/10.1021/acs.nanolett.6b04884.

[11]   R. Nakane, M. Tanaka, S. Sugahara, Preparation and characterization of ferromagnetic DO3-phase Fe3Si thin films on silicon-on-insulator substrates for Si-based spin-electronic device applications, Appl. Phys. Lett. 89 (2006) 192503. https://doi.org/10.1063/1.2378487.

[12]   A.V. Alekseev, G.G. Gumarov, D.A. Konovalov, V.Yu. Petukhov, V.I. Nuzhdin, Uniaxial magnetic anisotropy of iron-silicide thin films ion synthesized in an external magnetic field, J. Surf. Investig. X-Ray Synchrotron Neutron Tech. 8 (2014) 1124–1127. https://doi.org/10.1134/S1027451014050036.

[13]   N. Balakirev, V. Zhikharev, G. Gumarov, The formation of magnetic silicide Fe3Si clusters during ion implantation, 17th Int. Conf. Radiat. Eff. Insul. REI. 326 (2014) 61–64. https://doi.org/10.1016/j.nimb.2013.09.032.

[14]   L. Wang, Q. Qi, H. Wu, H. Zhang, J. Yin, Y. Yang, J. Huang, X. Yang, X. Liu, Z. Huang, Stress distribution around Fe5Si3 and its effect on interface status and mechanical properties of Si3N4 ceramics, J. Am. Ceram. Soc. 101 (2018) 856–864. https://doi.org/10.1111/jace.15240.

[15]   S.A. Lyashchenko, Z.I. Popov, S.N. Varnakov, E.A. Popov, M.S. Molokeev, I.A. Yakovlev, A.A. Kuzubov, S.G. Ovchinnikov, T.S. Shamirzaev, A.V. Latyshev, A.A. Saranin, Analysis of optical and magnetooptical spectra of Fe5Si3 and Fe3Si magnetic silicides using spectral magnetoellipsometry, J. Exp. Theor. Phys. 120 (2015) 886–893. https://doi.org/10.1134/S1063776115050155.

[16]   M.K. Kolel-Veetil, S.B. Qadri, M. Osofsky, R. Goswami, T.M. Keller, Carbon Nanocapsule-Mediated Formation of Ferromagnetic Fe5Si3 Nanoparticles, J. Phys. Chem. C. 113 (2009) 14663–14671. https://doi.org/10.1021/jp904188f.

[17]   J.K. Tripathi, P.C. Srivastava, Ion irradiation induced nano granular magnetic Fe5Si3 silicide phase formation in Fe/Si structures, Appl. Surf. Sci. 255 (2008) 2767–2772. https://doi.org/10.1016/j.apsusc.2008.08.035.

[18]   I.T. Yoon, Y.H. Kwon, Y. Shon, Ferromagnetic Properties of Fe-Implanted Si Followed by Thermal Annealing, J. Supercond. Nov. Magn. 28 (2015) 3623–3627. https://doi.org/10.1007/s10948-015-3207-2.

[19]   D. Errandonea, D. Santamaría-Perez, A. Vegas, J. Nuss, M. Jansen, P. Rodríguez-Hernandez, A. Muñoz, Structural stability of Fe5Si3 and Ni2Si studied by high-pressure x-ray diffraction and ab initio total-energy calculations, Phys. Rev. B. 77 (2008) 094113. https://doi.org/10.1103/PhysRevB.77.094113.

[20]   R. Skomski, P. Kumar, B. Balamurugan, B. Das, P. Manchanda, P. Raghani, A. Kashyap, D.J. Sellmyer, Exchange and magnetic order in bulk and nanostructured Fe5Si3, J. Magn. Magn. Mater. 460 (2018) 438–447. https://doi.org/10.1016/j.jmmm.2018.02.015.

[21]   K. Seo, S. Lee, Y. Jo, M.-H. Jung, J. Kim, D.G. Churchill, B. Kim, Room Temperature Ferromagnetism in Single-Crystalline Fe5Si3 Nanowires, J. Phys. Chem. C. 113 (2009) 6902–6905. https://doi.org/10.1021/jp902010j.

[22]   P.M. Enriquez-Navas, M.L. Garcia-Martin, Chapter 9 - Application of Inorganic Nanoparticles for Diagnosis Based on MRI, in: J.M. de la Fuente, V. Grazu (Eds.), Front. Nanosci., Elsevier, 2012: pp. 233–245. https://doi.org/10.1016/B978-0-12-415769-9.00009-1.

[23]   J. Dobson, Gene therapy progress and prospects: magnetic nanoparticle-based gene delivery, Gene Ther. 13 (2006) 283–287. https://doi.org/10.1038/sj.gt.3302720.

[24] R. Jurgons, C. Seliger, A. Hilpert, L. Trahms, S. Odenbach, C. Alexiou, Drug loaded magnetic nanoparticles for cancer therapy, J. Phys. Condens. Matter. 18 (2006) S2893–S2902. https://doi.org/10.1088/0953-8984/18/38/s24.

[25] S. Senthilarasu, R. Sathyamoorthy, S. Lalitha, Synthesis and characterization of β-FeSi2 grown by thermal annealing of Fe/Si bilayers for photovoltaic applications, CANCUN 2003. 82 (2004) 299–305. https://doi.org/10.1016/j.solmat.2004.01.027.

[26] B. Tatar, K. Kutlu, M. Ürgen, Synthesis of β-FeSi2/Si heterojunctions for photovoltaic applications by unbalanced magnetron sputtering, Thin Solid Films. 516 (2007) 13–16. https://doi.org/10.1016/j.tsf.2007.04.044.

[27] K. Shimura, K. Yamaguchi, H. Yamamoto, M. Sasase, S. Shamoto, K. Hojou, Photoluminescence of β-FeSi2 thin film prepared by ion beam sputter deposition method, Ion Beam Modif. Mater. 242 (2006) 673–675. https://doi.org/10.1016/j.nimb.2005.08.175.

[28] D. Santamaría-Pérez, J. Nuss, J. Haines, M. Jansen, A. Vegas, Iron silicides and their corresponding oxides: a high-pressure study of Fe5Si3, Solid State Sci. 6 (2004) 673–678. https://doi.org/10.1016/j.solidstatesciences.2004.03.027.

[29] Y. Maeda, K. Umezawa, Y. Hayashi, K. Miyake, K. Ohashi, Photovoltaic properties of ion-beam synthesized β-FeSi2/n-Si heterojunctions, Thin Solid Films. 381 (2001) 256–261. https://doi.org/10.1016/S0040-6090(00)01753-3.

[30] L. Antwis, L. Wong, A. Smith, K. Homewood, C. Jeynes, R. Gwilliam, Optimization and Characterisation of Amorphous Iron Disilicide formed by Ion Beam Mixing of Fe/Si Multilayer Structures for Photovoltaic Applications, AIP Conf. Proc. 1321 (2011) 278–281. https://doi.org/10.1063/1.3548379.

[31] H. Katsumata, Y. Makita, N. Kobayashi, H. Shibata, M. Hasegawa, I. Aksenov, S. Kimura, A. Obara, S. Uekusa, Optical absorption and photoluminescence studies of β-FeSi2 prepared by heavy implantation of Fe+ ions into Si, J. Appl. Phys. 80 (1996) 5955–5962. https://doi.org/10.1063/1.363591.

[32] M. NAITO, M. ISHIMARU, Formation process of β-FeSi2 from amorphous Fe-Si synthesized by ion implantation: Fe concentration dependence, J. Microsc. 236 (2009) 123–127. https://doi.org/10.1111/j.1365-2818.2009.03270.x.

[33] H.T. Lu, L.J. Chen, Y.L. Chueh, L.J. Chou, Formation of light-emitting FeSi2 in Fe thin films on ion-implanted (111)Si, J. Appl. Phys. 93 (2003) 1468–1471. https://doi.org/10.1063/1.1534379.

[34] Y.T. Chong, Q. Li, C.F. Chow, N. Ke, W.Y. Cheung, S.P. Wong, K.P. Homewood, The effect of ion implantation energy and dosage on the microstructure of the ion beam synthesized FeSi2 in Si, EMRS 2005 Symp. D. 124–125 (2005) 444–448. https://doi.org/10.1016/j.mseb.2005.08.042.

[35] W.J. Lakshantha, V.C. Kummari, T. Reinert, F.D. McDaniel, B. Rout, Depth profile investigation of β-FeSi2 formed in Si(100) by high fluence implantation of 50keV Fe ion and post-thermal vacuum annealing, 21st Int. Conf. Ion Beam Anal. 332 (2014) 33–36. https://doi.org/10.1016/j.nimb.2014.02.024.

[36] G.G. Gumarov, D.A. Konovalov, A.V. Alekseev, V.Yu. Petukhov, V.A. Zhikharev, V.I. Nuzhdin, V.A. Shustov, Scanning MOKE investigation of ion-beam-synesized silicide films, Ion Beam Synth. Modif. Nanostructured Mater. Surf. 282 (2012) 92–95. https://doi.org/10.1016/j.nimb.2011.08.056.

[37] K. Omae, I.-T. Bae, M. Naito, M. Ishimaru, Y. Hirotsu, J.A. Valdez, K.E. Sickafus, Structural evolution in Fe ion implanted Si upon thermal annealing, Radiat. Eff. Insul. 250 (2006) 300–302. https://doi.org/10.1016/j.nimb.2006.04.127.

[38] M. Naito, M. Ishimaru, Y. Hirotsu, J.A. Valdez, K.E. Sickafus, Transmission electron microscopy study on ion-beam-synthesized amorphous Fe–Si thin layers, Appl. Phys. Lett. 87 (2005) 241905. https://doi.org/10.1063/1.2142101.

[39] T.H. Yang, Y.L. Chueh, H.C. Chen, L.J. Chen, L.J. Chou, Auto-correlation function analysis of phase formation in iron ion-implanted amorphous silicon layers, Proc. Symp. Semicond. Silicides Sci. Future Technol. 8th IUMRS Int. Conf. Adv. Mater. 461 (2004) 126–130. https://doi.org/10.1016/j.tsf.2004.02.085.

[40] J. Frenkel, J. Doefman, Spontaneous and Induced Magnetisation in Ferromagnetic Bodies, Nature. 126 (1930) 274–275. https://doi.org/10.1038/126274a0.

[41] A. Akbarzadeh, M. Samiei, S. Davaran, Magnetic nanoparticles: preparation, physical properties, and applications in biomedicine, Nanoscale Res. Lett. 7 (2012) 144. https://doi.org/10.1186/1556-276X-7-144.

[42] B. Rout, M.S. Dhoubhadel, P.R. Poudel, V.C. Kummari, B. Pandey, N.T. Deoli, W.J. Lakshantha, S.J. Mulware, J. Baxley, J.E. Manuel, J.L. Pacheco, S. Szilasi, D.L. Weathers, T. Reinert, G.A. Glass, J.L. Duggan, F.D. McDaniel, An overview of the facilities, activities, and developments at the University of North Texas Ion Beam Modification and Analysis Laboratory (IBMAL), AIP Conf. Proc. 1544 (2013) 11–18. https://doi.org/10.1063/1.4813454.

[43] J. Perrière, Rutherford backscattering spectrometry, Vacuum. 37 (1987) 429–432. https://doi.org/10.1016/0042-207X(87)90327-7.

[44] J.F. Ziegler, M.D. Ziegler, J.P. Biersack, SRIM – The stopping and range of ions in matter (2010), Nucl. Instrum. Methods Phys. Res. Sect. B Beam Interact. Mater. At. 268 (2010) 1818–1823. https://doi.org/10.1016/j.nimb.2010.02.091.

[45] A. Mutzke, R. Schneider, W. Eckstein, R. Dohmen, SDTrimSP Version 5.00, 2018.

[46] L. Liu, Z. Xu, R. Li, R. Zhu, J. Xu, J. Zhao, C. Wang, K. Nordlund, X. Fu, F. Fang, Molecular dynamics simulation of helium ion implantation into silicon and its migration,

Nucl. Instrum. Methods Phys. Res. Sect. B Beam Interact. Mater. At. 456 (2019) 53–59. https://doi.org/10.1016/j.nimb.2019.06.034.

[47] H.Y. Chan, M.P. Srinivasan, N.J. Montgomery, C.P.A. Mulcahy, S. Biswas, H.-J.L. Gossmann, M. Harris, K. Nordlund, F. Benistant, C.M. Ng, D. Gui, L. Chan, Application of molecular dynamics for low-energy ion implantation in crystalline silicon, J. Vac. Sci. Technol. B Microelectron. Nanometer Struct. Process. Meas. Phenom. 24 (2006) 462–467. https://doi.org/10.1116/1.2137333.

[48] K. Nordlund, Molecular dynamics for ion beam analysis, Ion Beam Anal. 266 (2008) 1886–1891. https://doi.org/10.1016/j.nimb.2007.11.056.

[49] W. Möller, W. Eckstein, Tridyn — A TRIM simulation code including dynamic composition changes, Nucl. Instrum. Methods Phys. Res. Sect. B Beam Interact. Mater. At. 2 (1984) 814–818. https://doi.org/10.1016/0168-583X(84)90321-5.

[50] W. Möller, TRI3DYN – Collisional computer simulation of the dynamic evolution of 3-dimensional nanostructures under ion irradiation, Nucl. Instrum. Methods Phys. Res. Sect. B Beam Interact. Mater. At. 322 (2014) 23–33. https://doi.org/10.1016/j.nimb.2013.12.027.

[51] A. Mutzke, R. Schneider, W. Eckstein, R. Dohmen, A. Mutzke, R. Schneider, W. Eckstein, R. Dohmen, SDTrimSP: Version 5.00, IPP Rep. (2011).

[52] C. Borschel, C. Ronning, Ion beam irradiation of nanostructures – A 3D Monte Carlo simulation code, Nucl. Instrum. Methods Phys. Res. Sect. B Beam Interact. Mater. At. 269 (2011) 2133–2138. https://doi.org/10.1016/j.nimb.2011.07.004.

[53] Corteo20160816.pdf, (n.d.). http://www.lps.umontreal.ca/~schiette/uploads/Recherche/Corteo20160816.pdf (accessed August 8, 2018).

[54] F. Schiettekatte, Fast Monte Carlo for ion beam analysis simulations, Nucl. Instrum. Methods Phys. Res. Sect. B Beam Interact. Mater. At. 266 (2008) 1880–1885. https://doi.org/10.1016/j.nimb.2007.11.075.

[55] F. Schiettekatte, Fast Monte Carlo for ion beam analysis simulations, Ion Beam Anal. 266 (2008) 1880–1885. https://doi.org/10.1016/j.nimb.2007.11.075.

[56] L. Liao, H.B. Lu, J.C. Li, C. Liu, D.J. Fu, Y.L. Liu, The sensitivity of gas sensor based on single ZnO nanowire modulated by helium ion radiation, Appl. Phys. Lett. 91 (2007) 173110. https://doi.org/10.1063/1.2800812.

[57] J.H. He, C.S. Lao, L.J. Chen, D. Davidovic, Z.L. Wang, Large-Scale Ni-Doped ZnO Nanowire Arrays and Electrical and Optical Properties, J. Am. Chem. Soc. 127 (2005) 16376–16377. https://doi.org/10.1021/ja0559193.

[58] S. Hoffmann, J. Bauer, C. Ronning, Th. Stelzner, J. Michler, C. Ballif, V. Sivakov, S.H. Christiansen, Axial p-n Junctions Realized in Silicon Nanowires by Ion Implantation, Nano Lett. 9 (2009) 1341–1344. https://doi.org/10.1021/nl802977m.

[59] J.F. Ziegler, M.D. Ziegler, J.P. Biersack, SRIM – The stopping and range of ions in matter (2010), 19th Int. Conf. Ion Beam Anal. 268 (2010) 1818–1823. https://doi.org/10.1016/j.nimb.2010.02.091.

[60] W. Möller, W. Eckstein, J.P. Biersack, Tridyn-binary collision simulation of atomic collisions and dynamic composition changes in solids, Comput. Phys. Commun. 51 (1988) 355–368. https://doi.org/10.1016/0010-4655(88)90148-8.

[61] W. Möller, TRI3DYN – Collisional computer simulation of the dynamic evolution of 3-dimensional nanostructures under ion irradiation, Nucl. Instrum. Methods Phys. Res. Sect. B Beam Interact. Mater. At. 322 (2014) 23–33. https://doi.org/10.1016/j.nimb.2013.12.027.

[62] C. Borschel, C. Ronning, Ion beam irradiation of nanostructures – A 3D Monte Carlo simulation code, Nucl. Instrum. Methods Phys. Res. Sect. B Beam Interact. Mater. At. 269 (2011) 2133–2138. https://doi.org/10.1016/j.nimb.2011.07.004.

[63] Y.G. Li, Y. Yang, M.P. Short, Z.J. Ding, Z. Zeng, J. Li, IM3D: A parallel Monte Carlo code for efficient simulations of primary radiation displacements and damage in 3D geometry, Sci. Rep. 5 (2015) 18130.

[64] S. R. Messenger, E. A. Burke, G. P. Summers, M. A. Xapsos, R. J. Walters, E. M. Jackson, B. D. Weaver, Nonionizing energy loss (NIEL) for heavy ions, IEEE Trans. Nucl. Sci. 46 (1999) 1595–1602. https://doi.org/10.1109/23.819126.

[65] R.E. Stoller, M.B. Toloczko, G.S. Was, A.G. Certain, S. Dwaraknath, F.A. Garner, On the use of SRIM for computing radiation damage exposure, Nucl. Instrum. Methods Phys. Res. Sect. B Beam Interact. Mater. At. 310 (2013) 75–80. https://doi.org/10.1016/j.nimb.2013.05.008.

[66] D. Kalanov, A. Anders, C. Bundesmann, Ion beam sputtering of silicon: Energy distributions of sputtered and scattered ions, J. Vac. Sci. Technol. A. 37 (2019) 051507. https://doi.org/10.1116/1.5114973.

[67] C. Bundesmann, T. Amelal, Secondary particle properties for the ion beam sputtering of TiO2 in a reactive oxygen atmosphere, Appl. Surf. Sci. 485 (2019) 391–401. https://doi.org/10.1016/j.apsusc.2019.04.078.

[68] R. Arredondo, M. Oberkofler, T. Schwarz-Selinger, U. von Toussaint, V.V. Burwitz, A. Mutzke, E. Vassallo, M. Pedroni, Angle-dependent sputter yield measurements of keV D ions on W and Fe and comparison with SDTrimSP and SDTrimSP-3D, Nucl. Mater. Energy. 18 (2019) 72–76. https://doi.org/10.1016/j.nme.2018.12.007.

[69] R. Stadlmayr, P.S. Szabo, B.M. Berger, C. Cupak, R. Chiba, D. Blöch, D. Mayer, B. Stechauner, M. Sauer, A. Foelske-Schmitz, M. Oberkofler, T. Schwarz-Selinger, A. Mutzke, F. Aumayr, Fluence dependent changes of surface morphology and sputtering yield of iron: Comparison of experiments with SDTrimSP-2D, Nucl. Instrum. Methods Phys. Res. Sect. B Beam Interact. Mater. At. 430 (2018) 42–46. https://doi.org/10.1016/j.nimb.2018.06.004.

[70] S. Eswara, Jean-Nicolas Audinot, Brahime El Adib, Maël Guennou, Tom Wirtz, Patrick Philipp, Defect formation in multiwalled carbon nanotubes under low-energy He and Ne ion irradiation, J. Nanotechnol. 9 (2018) 1951–1963. https://doi.org/10.3762/bjnano.9.186.

[71] A. De Backer, A. Sand, C.J. Ortiz, C. Domain, P. Olsson, E. Berthod, C.S. Becquart, Primary damage in tungsten using the binary collision approximation, molecular dynamic simulations and the density functional theory, Phys. Scr. T167 (2016) 014018. https://doi.org/10.1088/0031-8949/t167/1/014018.

[72] A. Lasa, C. Björkas, K. Vörtler, K. Nordlund, MD simulations of low energy deuterium irradiation on W, WC and W2C surfaces, J. Nucl. Mater. 429 (2012) 284–292. https://doi.org/10.1016/j.jnucmat.2012.06.012.

[73] U. Plank, G. Meisl, U. von Toussaint, T. Höschen, W. Jacob, Study of the temperature-dependent nitrogen retention in tungsten surfaces using X-ray photoelectron spectroscopy, Nucl. Mater. Energy. 17 (2018) 48–55. https://doi.org/10.1016/j.nme.2018.08.006.

[74] A. Mutzke, W. Eckstein, Ion fluence dependence of the Si sputtering yield by noble gas ion bombardment, Nucl. Instrum. Methods Phys. Res. Sect. B Beam Interact. Mater. At. 266 (2008) 872–876. https://doi.org/10.1016/j.nimb.2008.01.053.

[75] H. Hofsäss, K. Zhang, A. Mutzke, Simulation of ion beam sputtering with SDTrimSP, TRIDYN and SRIM, Sel. Manuscr. Aris. 18th Int. Conf. Surf. Modif. Mater. Ion Beams SMMIB-2013. 310 (2014) 134–141. https://doi.org/10.1016/j.apsusc.2014.03.152.

[76] W. Eckstein, R. Dohmen, Isotope sputtering of molybdenum, Nucl. Instrum. Methods Phys. Res. Sect. B Beam Interact. Mater. At. 129 (1997) 327–340. https://doi.org/10.1016/S0168-583X(97)00289-9.

[77] W. Eckstein, Oscillations of sputtering yield, Nucl. Instrum. Methods Phys. Res. Sect. B Beam Interact. Mater. At. 171 (2000) 435–442. https://doi.org/10.1016/S0168-583X(00)00321-9.

[78] R. Behrisch, W. Eckstein, Sputtering by Particle Bombardment, 1st ed., Springer-Verlag Berlin Heidelberg, 2007. 10.1007/978-3-540-44502-9.

[79] J.F. Ziegler, M.D. Ziegler, J.P. Biersack, SRIM – The stopping and range of ions in matter (2010), Nucl. Instrum. Methods Phys. Res. Sect. B Beam Interact. Mater. At. 268 (2010) 1818–1823. https://doi.org/10.1016/j.nimb.2010.02.091.

[80] J.F. Ziegler, THE STOPPING AND RANGE OF IONS IN SOLIDS, in: J.F. Ziegler (Ed.), Ion Implant. Sci. Technol. Second Ed., Academic Press, 1988: pp. 3–61. https://doi.org/10.1016/B978-0-12-780621-1.50005-8.

[81] J.P. Biersack, L.G. Haggmark, A Monte Carlo computer program for the transport of energetic ions in amorphous targets, Nucl. Instrum. Methods. 174 (1980) 257–269. https://doi.org/10.1016/0029-554X(80)90440-1.

[82] G.S. Was, S. Taller, Z. Jiao, A.M. Monterrosa, D. Woodley, D. Jennings, T. Kubley, F. Naab, O. Toader, E. Uberseder, Resolution of the carbon contamination problem in ion irradiation experiments, Nucl. Instrum. Methods Phys. Res. Sect. B Beam Interact. Mater. At. 412 (2017) 58–65. https://doi.org/10.1016/j.nimb.2017.08.039.

[83] J. Wang, M.B. Toloczko, K. Kruska, D.K. Schreiber, D.J. Edwards, Z. Zhu, J. Zhang, Carbon Contamination During Ion Irradiation - Accurate Detection and Characterization of its Effect on Microstructure of Ferritic/Martensitic Steels, Sci. Rep. 7 (2017) 15813. https://doi.org/10.1038/s41598-017-15669-y.

[84] W.J. Lakshantha, F.D. McDaniel, B. Rout, Formation and characterization of embedded Fe3Si binary structures in Si, J. Appl. Phys. 125 (2019) 195301. https://doi.org/10.1063/1.5091541.

[85] A.L. Patterson, The Scherrer Formula for X-Ray Particle Size Determination, Am. Phys. Soc. 56 (1939) 978–982. https://doi.org/10.1103/PhysRev.56.978.

[86] A. Mutzke, R. Schneider, W. Eckstein, R. Dohmen, SDTrimSP Version 5.00, (2018).

[87] J. Segura-Ruiz, G. Martínez-Criado, M.H. Chu, S. Geburt, C. Ronning, Nano-X-ray Absorption Spectroscopy of Single Co-Implanted ZnO Nanowires, Nano Lett. 11 (2011) 5322–5326. https://doi.org/10.1021/nl202799e.

[88] C. Borschel, S. Spindler, D. Lerose, A. Bochmann, S.H. Christiansen, S. Nietzsche, M. Oertel, C. Ronning, Permanent bending and alignment of ZnO nanowires, Nanotechnology. 22 (2011) 185307. https://doi.org/10.1088/0957-4484/22/18/185307.

[89] C. Borschel, M.E. Messing, M.T. Borgström, W. Paschoal, J. Wallentin, S. Kumar, K. Mergenthaler, K. Deppert, C.M. Canali, H. Pettersson, L. Samuelson, C. Ronning, A New Route toward Semiconductor Nanospintronics: Highly Mn-Doped GaAs Nanowires Realized by Ion-Implantation under Dynamic Annealing Conditions, Nano Lett. 11 (2011) 3935–3940. https://doi.org/10.1021/nl2021653.

[90] M. Ernst, H. Schulte-Huxel, R. Niepelt, S. Kajari-Schröder, R. Brendel, Thin Crystalline Macroporous Silicon Solar Cells with Ion Implanted Emitter, Proc. 3rd Int. Conf. Cryst. Silicon Photovolt. SiliconPV 2013. 38 (2013) 910–918. https://doi.org/10.1016/j.egypro.2013.07.364.

[91] D.B. Guerra, S. Müller, M.P. Oliveira, P.F.P. Fichtner, R.M. Papaléo, Bi nanowires modified by 400 keV and 1 MeV Au ions, AIP Adv. 8 (2018) 125103. https://doi.org/10.1063/1.5063463.

[92] A Johannes and S Noack and W Paschoal Jr and S Kumar and D Jacobsson and H Pettersson and L Samuelson and K A Dick and G Martinez-Criado and M Burghammer and C Ronning, Enhanced sputtering and incorporation of Mn in implanted GaAs and ZnO nanowires, J. Phys. Appl. Phys. 47 (2014) 394003.

[93] C. Csato, F. Krippendorf, S. Akhmadaliev, J. von Borany, W. Han, T. Siefke, A. Zowalla, M. Rüb, Energy filter for tailoring depth profiles in semiconductor doping application, Proc. 19th Int. Conf. Ion Beam Modif. Mater. IBMM 2014. 365 (2015) 182–186. https://doi.org/10.1016/j.nimb.2015.07.102.

[94] A. Johannes, S. Noack, W. Wesch, M. Glaser, A. Lugstein, C. Ronning, Anomalous Plastic Deformation and Sputtering of Ion Irradiated Silicon Nanowires, Nano Lett. 15 (2015) 3800–3807. https://doi.org/10.1021/acs.nanolett.5b00431.

[95] H. Holland-Moritz, S. Scheeler, C. Stanglmair, C. Pacholski, C. Ronning, Enhanced sputter yields of ion irradiated Au nano particles: energy and size dependence, Nanotechnology. 26 (2015) 325301. https://doi.org/10.1088/0957-4484/26/32/325301.